Università degli Studi di Napoli "Federico II"

Graduate School of Industrial Engineering

International PhD program on "Novel Technologies for Materials, Sensors and Imaging"
in agreement with
"Chalmers University of Technology", Göteborg

$YBa_2Cu_3O_{7-\delta}$ nanowires for ultrasensitive magnetic flux detectors and optical applications

Doctoral dissertation by
Riccardo Arpaia

Tutors:
Prof. Floriana Lombardi
Prof. Francesco Tafuri
Prof. Thilo Bauch

Coordinator:
Prof. Luciano Lanotte
Co-tutor:
Prof. Antonello Andreone

XXV cycle 2010-2014

Contents

List of symbols and abbreviations

Definitions of symbols

$\vec{A}$	Magnetic vector potential
A_{eff}	Effective area
A_g	Geometrical area
A_w	Nanowire cross section, $w \cdot t$
β_L	Screening inductance factor, $I_C^{max} L_{loop}/\Phi_0$
B_C^0	Thermodynamical critical field
δ	Doping parameter, $0 \leq 7 - n \leq 1$
δ^m	Film/substrate lattice mismatch
Δ	Superconducting gap
ΔI_C	Critical current modulation depth
ΔR	Amplitude of resistance oscillations
e	Electronic elementary charge
F	Free energy
F_n	Free energy of the normal phase
F/S	Ferromagnetic/Superconducting
h	Plank constant
H_c	Magnetic critical field
I_b	Bias current
I_C	Critical current
I_C^{max}	Maximum critical current
J_C	Critical current density, I_C/A_w
$\bar{J}_C$	Average critical current density
J_d	Depairing critical current density
J_s	Superconducting current density
J_v	Vortex entry critical current density
k_B	Boltzmann constant
λ_L	London penetration depth
λ_0	Zero temperature London penetration depth
λ_P	Pearl length, $\lambda_L^2/2t$

l	Nanowire length
ℓ	Electronic mean free path
L_g	Geometrical inductance
L_k	Kinetic inductance
L_{loop}	Total loop inductance
μ_B	Bohr magneton
n_s	Superfluid density
n	Oxygen content
ξ	Coherence length
ξ_0	Zero temperature coherence length
p	Hole doping
p_{ann}	Oxygen post-annealing pressure
R_L	Load resistance
R_{Little}	Wire resistance due to phase slips (Little model)
R_N	Normal resistance
R_{sh}	Shunt resistance
R_v	Wire resistance due to vortex entry
S_v	Voltage noise density
S_Φ	Flux noise density, S_v/V_Φ
t	Film/nanowire thickness
T_C	Critical Temperature
T_{Curie}	Curie Temperature
T_{dep}	Deposition Temperature
T_N	Néel Temperature
T^{onset}	Temperature onset of the superconducting transition
v_s	Superfluid velocity
V_Φ	Voltage-to-flux transfer function
w	Nanowire width
Φ	Magnetic Flux
Φ_0	Magnetic Flux Quantum, $h/2e$
ϕ	Phase
$\Psi(\vec{r})$	Order Parameter, $\lvert\Psi(\vec{r})\rvert e^{i\phi(\vec{r})}$
Ψ_∞	Equilibrium Order Parameter

List of abbreviations

AF	Antiferromagnetic
AFM	Atomic Force Microscopy
CPR	Current Phase Relation
dc	Direct Current
FFT	Fast Fourier Transform
FWHM	Full width at half maximum
GL	Ginzburg-Landau
HTS	High Critical Temperature Superconductors
IVC	Current-Voltage Characteristic

LAO	$LaAlO_3$
LSMO	$La_{0.7}Sr_{0.3}MnO_3$
HTS	Low Critical Temperature Superconductors
PLD	Pulsed Laser Deposition
$R(B)$	Resistance vs Magnetic field
$R(T)$	Resistance vs Temperature
SEM	Scanning Electron Microscopy
SNSPD	Superconducting Nanowire Single Photon Detector
SQUID	Superconducting QUantum Interference Device
STO	$SrTiO_3$
TAPS	Thermally activated phase slip
TEM	Transmission Electron Microscopy
XRD	X-Ray Diffraction
YBCO	$YBa_2Cu_3O_7$

1 Introduction

This thesis focuses on the realization and study of superconducting nanostructures, that in recent years have attracted great attention for both a fundamental physics point of view and for applications [1, 2, 3, 4, 5, 6]. The choice to work with High Critical Temperature Superconductors (HTSs), in our case $YBa_2Cu_3O_{7-\delta}$ (YBCO), does not follow the international research trend. Indeed the number of papers about YBCO published per year on the main physics and condensed matter physics journals (see Fig. 1.1) has had a negative trend in the last ten years.

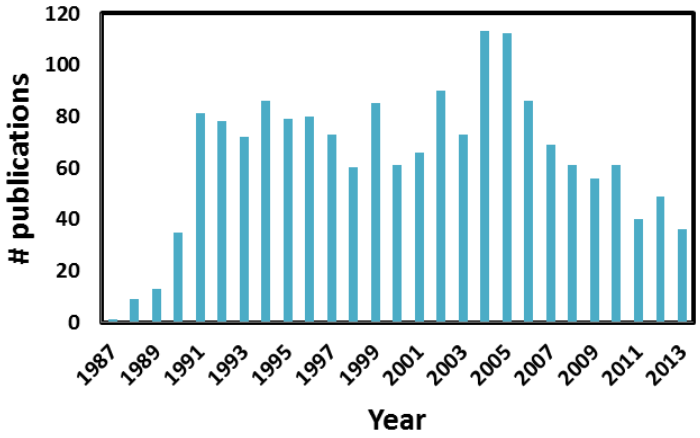

Figure 1.1: Number of publications on YBCO per year, from its discovery in 1987 until the end of 2013 (bibliometric statistics obtained from Scopus, considering Science, Nature, Phys. Rev. Lett., Phys. Rev. B., Appl. Phys. Lett., Supercond. Sci. Technol.)

The nanotechnologies applied to HTS compounds have instead made huge step forward making it possible experiments which could be crucial in identifying the mechanism leading to superconductivity. Even though less people, compared to years ago, appear to be committed to study HTS, the experimental scenario is finally mature to make real discoveries.

- *Why HTS at the nanoscale?*

The microscopic origin of the complex properties of HTS still remains a grand challenge in solid state physics. Is the superconducting phenomenon a purely electronic mechanism or the phonon interaction play a role? By now most researchers agree that a doped Mott insulator is the correct starting point for a microscopic theory and that some kind of quantum spin dynamics plays a key role in the formation of Cooper pairs. Quite recently, the stripes model to explain high T_C superconductivity has gained great interest [7]: stripes are lattice-constant wide lines, separated by antiferromagnetic insulating regions, on which all the charge carriers reside. Their length has been suggested to be somewhere between 4 and 400 nm. Considering that the coherence length and the London penetration depth are also in the order of nanometers in HTS materials, it becomes evident that most of the fundamental lengths in high-T_C superconductivity are on such a scale. Therefore, experimental investigation of structures on the nanoscale can be vital to the understanding of the microscopic mechanisms.

Superconductivity in structures with reduced dimensionality is very intriguing and still unsettled, even for Low Critical Temperature Superconductors (LTSs), touching interesting topics as the suppression of superconductivity via phase-slips due to quantum or thermal fluctuations [1, 4, 6], and the enhancement of the superconducting properties in nanowires and nanodots [8, 9, 10, 11]. Moreover, unique effects have been proposed during the years in HTSs, that have no counterpart in conventional superconductivity. We refer in particular to spin-charge separation [12], detection of electron fractionalization via novel vortex-like excitations [13], preformed Cooper pairs [14] and Bose-condensation [15] in the normal state of the underdoped regime. Nanoscale cuprate devices offer a novel approach to the study of these theoretical proposals.

From an application point of view, HTS nanostructures can be potentially employed in single photon detectors and in nanoSQUIDs, where they have been predicted to behave as weak links [16, 17].

The investigation of HTS at the nanoscale requires the realization of homogeneous nanostructures preserving "pristine" superconducting properties: the structure, the morphology and the stoichiometry need to be as close as possible to the bulk ones. In this way novel phenomena can be directly attributed to intrinsic properties of the superconductor, rather than to inhomogeneities and defects possibly introduced by the nanopatterning procedure.

While the reliable fabrication of nanostructures is nowadays feasible for conventional superconductors, it still represents an extremely challenging task for cuprate HTS, because of their chemical instability, mostly related to oxygen out-diffusion, and their extreme sensitivity to defects and disorder due to very short coherence length (of the order of 1 nm). The result is that - while for LTS the nanoscale is readily achievable - the properties of HTS nanostructures available in literature up to now present such a spread of values, that it is difficult to draw a clear picture of the physics in play [18, 19, 20, 21, 22].

The realization of HTS nanostructures requires:

- *the ability to deposit homogeneous and epitaxial thin films.* The growth of HTS is problematic in itself, because of the strong dependence of the superconducting properties on the ratios of different elements (in particular the oxygen doping).

  We have succeeded in getting high quality thin films with very smooth surfaces, of crucial relevance for the patterning of nanostructures, and relatively high critical temperature close to the optimal doping.

- *the ability to master nanoscale structures.* Since the deposition of HTS materials takes place at high temperature (T $\approx$ 800°C), traditional lift-off procedures cannot be used. To realize HTS nanostructures the most common top-down approach is based on electron beam lithography in combination with an amorphous hard mask and ion etching. The challenge is therefore to minimize/eliminate the damage to the nanostructures (oxygen losses, disorder) due to the resist baking and - even more - to the ion milling etching.

  By using a soft etching procedure and preserving a Au capping layer on top of the nanostructures, we succeeded in the fabrication of YBCO nanowires with cross sections down to 40×50 nm^2 and lengths from 200 nm to several microns. These nanostructures exhibit critical temperatures T_C similar to those of the electrodes/unpatterned film and carry critical current densities J_C close to the theoretical depairing limit. This last result, difficult to achieve even for conventional superconductors, gives a measure of the highly uniform superconductive properties of our nanowires, representing model systems to study HTS at the nanoscale.

The outline of the thesis is the following:

In Chapter 2 we will give an overview of the basic properties of superconductivity and of cuprates, which are of relevance for the discussion of the experiments, with reference to the current literature on the subject.

In the first part of the thesis we will discuss about the optimization of the thin film growth of YBCO (Chapter 3), the fabrication of YBCO nanowires (Chapter 4) and their transport characterization (Chapter 5), used as a benchmark to test the quality of these structures.

In the second part of the thesis, we will show instead the employment of YBCO nanowires in devices for fundamental studies and for ultrasensitive sensors.

The shortest nanowires have been used for the realizations of YBCO nanoSQUIDs with loops on the nanometer scale (Chapter 6). The development of such sensors with LTS nanowires has recently gained a lot of attention for the possibility to achieve the necessary flux sensitivity to detect magnetic moment of nanoscaled systems, with the ultimate goal of observing a single spin [23, 24, 25, 26]. In the case of YBCO, several attempts have been made in the mid-'90s, but a proper SQUID behavior has never been observed [27, 28]. On the contrary our devices work in the full temperature range up to T_C, exhibiting critical current modulations as a function of the external magnetic

field, never seen before for similar HTS devices. Moreover, they show record values for the white flux noise, below 1 $\mu\Phi_0/\sqrt{\text{Hz}}$ making them very attractive for many applications, ranging from nanomagnetism to spintronics and spin-based quantum information processing.

In Chapter 7 we will present our results on YBCO nanorings. These structures, instrumental in studying the fluxoid quantization and other coherent quantum phenomena, have attracted a lot of interest in recent years: the analysis of the magnetoresistance $R(B)$ oscillations at temperatures close to the critical temperature allows the identification of the responsible charge carriers in superconductors, shedding light on different issues on HTS pairing mechanisms. $R(B)$ measurements on our devices show large magnetoresistance oscillations with period $h/2e$, confirming the $2e$ value for the elemental superfluid charge in optimally doped YBCO. Moreover, differently to what previously reported in literature [29], as a consequence of the high degree of homogeneity of our nanostructures, we have a clear evidence of a uniform vorticity of the order parameter inside the rings, which therefore represent ideal sensors to probe the fluxoid quantization. These results represent solid grounds for future experiments on underdoped YBCO nanorings, where a crossover from $h/2e$ to h/e or $h/4e$ flux periodicities has been predicted [30, 31, 32, 33].

The longest nanowires have been employed in devices, described in Chapter 8, aimed at the detection of single photons. YBCO nanowires are indeed potentially very interesting for this application because of their fast thermalization dynamics. Superconducting nanowire single photon detectors up to now have been made only with LTS materials [34]. To reach this goal, many requirements have to be fulfilled, implying additional technological issues. We have realized very large structures, employing nanowires with length up to 10 μm and covered by a ferromagnetic $La_{0.7}Sr_{0.3}MnO_3$ capping layer, without undergoing a severe deterioration of the superconducting properties. We measured the response of the devices to optical laser pulses as a function of the current bias, of the temperature and of the power, finding that a major contribution to the photoresponse signals has a bolometric nature.

Finally, Chapter 9 gives a summary of the main results, with an outlook for possible future work.

2

Introduction to superconductivity and cuprates

2.1 Brief historical review of superconductivity

In what follows we will give a brief chronological account of the superconductivity phenomenon from its discovery to the understanding of the microscopic mechanism for conventional materials:

- 1911. By measuring the mercury resistance as a function of the temperature, Onnes discovers the first hallmark characterizing the superconductivity: the perfect conductivity. Below a critical temperature T_C, the metal resistance rapidly vanishes [35].

- 1933. Meissner and Ochsenfeld discover the second hallmark of the superconductors: the perfect diamagnetism. A magnetic field less than a critical value, B_C, is excluded from the bulk of a superconductor when the latter is cooled down below T_C (the so-called Meissner effect) [36].

- 1935. Fritz and Heinz London develop two equations, which relate the current to the electromagnetic fields in a superconductor, so describing the two previously observed hallmarks of superconductivity [37]:

$$\partial_t \vec{J}_s = \frac{n_s e^{*2}}{m^*} \vec{E} \tag{2.1}$$

$$\vec{\nabla} \times \vec{J}_s = -\frac{n_s e^{*2}}{m^*} \vec{B} \,, \tag{2.2}$$

  where $\vec{J}_s$ is the superconducting current density, $\vec{E}$ and $\vec{B}$ are respectively the electric and the magnetic fields within the superconductor, n_s is the density of superconducting electrons which flow without dissipation (superfluid density), m^* and e^* are respectively the effective mass and effective electric charge of superconducting electrons (which typically are assumed to take the double value of the mass and the elementary charge in the normal state, i.e. $m^* = 2m$ and $e^* = 2e$, with $e \approx -1.6 \times 10^{-19}$ C). The equation (2.1) describes the perfect

conductivity: the electric field accelerates the super-electrons, while it simply sustains the velocity of the electrons in normal metals, described by the Ohm's law. The equation (2.2), combined with the curl of Ampere's law, explains instead the Meissner effect:

$$\nabla^2 \vec{B} = \frac{1}{\lambda_L^2} \vec{B} \, , \qquad \lambda_L \equiv \sqrt{\frac{m^*}{\mu_0 n_s e^{*2}}} \, , \tag{2.3}$$

with μ_0 the vacuum permeability. The magnetic field is screened completely in the bulk of the material due to screening currents flowing in a thin region at the surface of the superconductor. Both the magnetic field and the corresponding screening currents decay exponentially into a superconductor from its surface with a characteristic length scale given by λ_L, known as the *London penetration depth*.

- 1950. Ginzburg and Landau postulate a phenomenological model [38], based on Landau's previously established theory of second-order phase transitions, which extends the London theory, considering the superfluid density $n_s(\vec{r})$ as function of spatial variables, and introduces the order parameter, a complex wavefunction related to the superfluid density, defined as

$$\Psi(\vec{r}) = |\Psi(\vec{r})| e^{i\phi(\vec{r})} \, , \tag{2.4}$$

where $|\Psi(\vec{r})| = \sqrt{n_s(\vec{r})}$ is the amplitude and $\phi(\vec{r})$ is the phase as a function of position.

Their theory is developed at temperature close to the superconducting transition, where the order parameter $\Psi(\vec{r})$ is postulated to be small and slowly varying in the space. As a consequence, the free energy $F = F(\Psi, T)$ of the superconducting system, immersed in a magnetic field B, can be expanded in series of Ψ and $\vec{\nabla}\Psi$, taking the form [39]

$$F = F_n + \alpha |\Psi|^2 + \frac{\beta}{2} |\Psi|^4 + \frac{1}{2m^*} \left| (-i\hbar \vec{\nabla} - e^* \vec{A}) \Psi \right|^2 + \frac{\vec{B}^2}{2\mu_0} \, , \tag{2.5}$$

where F_n is the free energy of the normal phase, $\alpha = \partial F / \partial n_s$ and $\beta = \partial^2 F / \partial n_s^2$ are temperature dependent parameters, and $\vec{A}$ is the magnetic vector potential.

The equilibrium wave function can be found minimizing the free energy written in eq. (2.5), integrated on the system volume, with respect to variations both in the order parameter and in the vector potential. The results are the two Ginzburg-Landau (GL) equations:

$$\alpha |\Psi| + \beta |\Psi|^2 \Psi + \frac{1}{2m^*} (-i\hbar \vec{\nabla} - e^* \vec{A})^2 \Psi = 0 \tag{2.6}$$

$$\vec{J_s} = \frac{\hbar e^*}{2im^*} (\Psi^* \vec{\nabla} \Psi - \Psi \vec{\nabla} \Psi^*) - \frac{e^{*2}}{m^*} \vec{A} |\Psi|^2 \, , \tag{2.7}$$

with the boundary condition $(-i\hbar\nabla - e^*\vec{A})\Psi|_n = 0$, assuring that no current passes through the surface n. Beside the London penetration depth, contained in eq. (2.7), a second characteristic length scale can be extracted, from the first GL equation, representing the distance at which the order parameter can vary without the system undergoing an energy increase. Considering a negligible external magnetic field and a very small but finite value of Ψ at some point in a superconductor just above its transition temperature, eq. (2.6) becomes

$$\nabla^2\Psi = \frac{\Psi}{\xi^2}\,, \qquad \xi \equiv \sqrt{\frac{\hbar^2}{2m^*|\alpha|}}\,. \tag{2.8}$$

This equation describes an exponential decay of Ψ on a characteristic length scale given by the *coherence length* ξ.

- 1950. Maxwell observes the Isotope effect for Hg, which suggested that the electron-phonon coupling is related to the superconductive phenomenon [40].

- 1957. Bardeen, Cooper and Schrieffer (BCS) propose the first microscopic theory of superconductivity [41]. According to their model, electrons of opposite spin and momentum close to the Fermi surface may overcome the Coulomb repulsion at temperatures below the critical one, due to a weak attractive force mediated by the electron-phonon interactions. As a consequence, they pair up into spin singlet pairs, named Cooper pairs, and form a condensate. This superconducting condensate is described by the order parameter $\Psi(\vec{r})$ and $|\Psi(\vec{r})|^2 = n_s(\vec{r})$ is the density of Cooper pairs. The coherence length ξ represents the length scale of the pair interaction. The energy required to break a Cooper pair is 2Δ, where Δ is the gap, predicted by the BCS theory, in the excitation spectrum of the superconductor. However, the BCS theory predicts a theoretical maximum critical temperature of about 25-30 K [42].

2.2 High-T_C superconductors and $YBa_2Cu_3O_{7-\delta}$

The discovery in 1986, by Bednorz and Müller, of a new class of compounds with a $T_C \approx 35$ K [43] was embraced by the scientific community with great enthusiasm. The existence of superconductors overcoming the T_C limit predicted by the BCS theory opened new perspectives in the quest toward room temperature superconductivity. The new compound was $Ba_xLa_{5-x}Cu_5O_{5(3-y)}$ (LBCO), in which the substitution of some La^{3+} ions with Ba^{2+} ions created hole-carriers, giving rise to the superconductivity. Few months later another cuprate, $YBa_2Cu_3O_{7-\delta}$ (YBCO), was discovered [44] with a $T_C = 92$ K. Since then many other HTS materials have been discovered, including both electron- and hole- doped superconductors, with T_C up to 135 K under ambient pressure in mercury compounds [45]. However, YBCO is still one of the most important HTS materials for both fundamental studies and applications, together with $La_{2-x}Sr_xCuO_4$ (LSCO) and $Bi_2Sr_2Ca_2Cu_3O_{10}$ (BSCCO).

2.2.1 Crystal structure

All HTS cuprates have a quasi-two-dimensional (2D) layered structure in common, where one or more copper oxide (CuO_2) planes are contained. Their structure is based on an alternate stacking of CuO_2 planes separated by other oxide layers or layers containing a single element. These intermediate layers normally act as charge reservoirs [46], which maintain both charge neutrality as well as cohesion of the structure. The interaction between CuO_2 planes and charge reservoirs plays an important role for the control and the change of the carrier concentration. Indeed, substitution or insertion of oxygen in the layers separating the CuO_2 planes dopes the material by either electrons or holes [47] (see Fig. 2.1a).

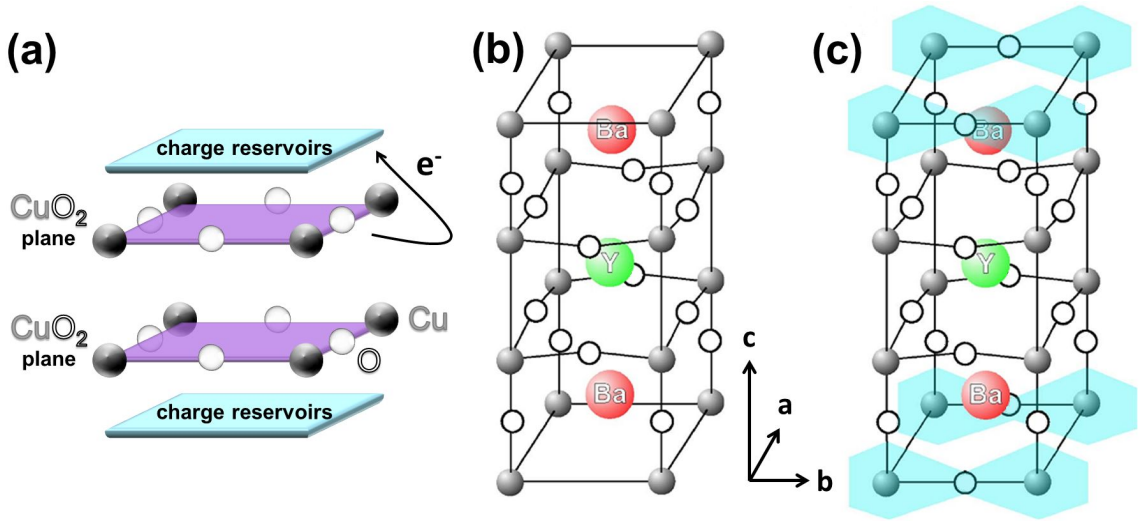

Figure 2.1: (a) The alternate stacking of CuO_2 planes separated by charge reservoir layers. Hole doping is represented by the transfer of electrons from the CuO_2 planes to the charge reservoirs. (b) and (c) represent respectively the $YBaCu_3O_6$ and the $YBaCu_3O_7$ unit cell. Light blue regions highlight the presence of the CuO chains. (Adapted from [48])

The $YBaCu_3O_7$ unit cell consists of three perovskite cells on top of each other (see Fig. 2.1b). Each perovskite unit cell contains a Y or Ba atom at the center: Ba in the bottom and in the top unit cells, Y in the middle one. Cu atoms occupy all the corner sites, while oxygens are placed in the middle edge positions. The CuO_2 planes are located right above and below the Y ion. Oxygen atoms at the top and bottom planes of the $YBaCu_3O_7$ cell are instead missing in the [100] direction, giving rise to CuO chains in the [010] direction. These chains act as charge reservoirs, and are extremely sensitive to oxygen doping.

Oxygen vacancies, introduced in the CuO chains, play indeed an important role, varying the oxygen content (indicated as $n = 7-\delta$) from 6 to 7 per formula [49]. When $\delta = 1$, YBCO is an insulator with a tetragonal crystal structure. By adding oxygen into the charge reservoirs, i.e. decreasing δ, one dimensional CuO chains along the b axis are formed, changing the crystal structure to orthorhombic: the CuO_2 planes are hole-doped and the compound becomes superconducting, with a variable T_C depending on the oxygen stoichiometry. At the optimal doping ($\delta \approx 0$), the lattice parameters of

the unit cell are $a = 3.82$ Å, $b = 3.89$ Å and $c = 11.69$ Å [50].

Such a complex chemistry, together with the large diffusion length of oxygen even at moderate temperatures [51], may affect the YBCO properties at the nanoscale. Oxygen out-diffusion, induced by sample overheating and small dimensions, can indeed dramatically change the structural and superconducting properties.

2.2.2 Phase diagram

YBCO can be doped by introducing oxygen in the CuO chains, resulting in a change of the carrier concentration (hole doping) of the CuO_2 planes [52]. The resulting phase diagram, shown in Fig. 2.2 as a function of both the hole doping p and the oxygen content n per unit cell, is very rich and complex, and still under discussion.

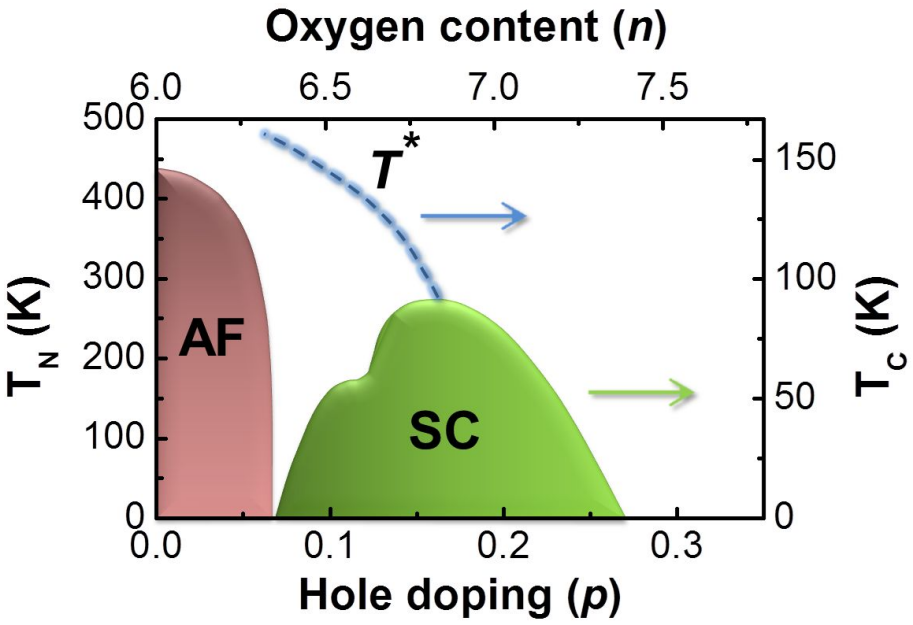

Figure 2.2: Phase diagram of $YBa_2Cu_3O_{7-\delta}$, as a function of both hole doping p and oxygen content n. T_N and T_C are respectively the Néel and the critical temperature. (Adapted from [53])

At zero doping ($p = 0$, $n = 6.0$) YBCO is a Mott-Hubbard insulator with antiferromagnetic (AF) long range order [54]. The AF ordering is easily destroyed by only a small amount of hole doping ($p = 0.05$, $n = 6.4$), giving rise to a metallic compound, characterized by superconductivity (SC) with low critical temperatures. By further doping, the superconducting transition temperature increases, reaching its maximum ($T_C = 94$ K for bulk crystals) for an optimal value $p = 0.16$ ($n \approx 7.0$). Upon additional doping, T_C decreases and the superconductivity disappears at $p = 0.27$ ($n = 7.4$).

This phase diagram can be divided into three regions, namely the underdoped, optimally doped and overdoped regime:

- the *overdoped* region ($p > 0.16$) is explained in terms of the Fermi liquid theory, which associates the electronic excitations at the Fermi level to an non-interacting gas of renormalized quasiparticles [55]. However, recent studies have proven small deviations from this model [56].

- the *optimally doped* region ($p \approx 0.16$) is commonly described as a "strange metal phase". The normal state properties are indeed still not univocally understood. However, the linear temperature dependence of the electrical resistance, observed over the entire accessible temperature range up to 1000 K, can be phenomenologically explained assuming a strangely modified excitation spectrum ("Marginal Fermi Liquid") [57].

- the *underdoped* region ($p < 0.16$) is probably the most intriguing part of the phase diagram. The main characteristic of this phase is that a gapped state, with the same symmetry as the superconducting gap, persists up to a temperature T^*, which is well above T_C. This region of the phase diagram has been intensively studied by various experimental techniques [58], which all conclude on the existence of a pseudogap region in the normal state phase of the underdoped regime that disappears moving in the optimally doped region of the phase diagram [59]. The connection between the pseudogap and the superconducting phase is still debated: are they competing orders [60, 61] (pseudogap state is suppressed below T_C) or do they cooperate [62, 63] (the pseudogap phase is a precursor of the superconducting state)? The answer to these questions may have a central role in the comprehension of the microscopic mechanisms of HTS.

The section of the phase diagram which encloses the superconductive phase as a function of doping is commonly known as the superconducting dome. Two plateaux at $T = 90$ K and $T \approx 60$ K are clearly visible. The first one is related to the occurrence of the optimal doping, while the origin of the second one, in the underdoped region, is still unclear [64, 48]. Two main explanations have been proposed. The first one suggests an ordering of the oxygen atoms in the basal planes (the planes where the CuO chains are located) [65, 66]. The second one suggests a purely electronic reason: the superconductivity is weakened at the hole doping of $p = 0.125$ ("1/8 anomaly"), as a consequence of a charge density wave instability (e.g. the formation of charge stripes) [67, 68, 69]. An enhancement of the T_C reduction at that value of doping leads to the plateau formation.

2.2.3 Superconducting properties

The poor coupling between CuO_2 planes, which are perpendicular to the c-axis, results in a weak superconductivity along this direction and in a high anisotropy of the superconducting properties (see Table 2.1).

As a consequence of the orthorhombicity of the YBCO unit cell, anisotropy in the a and b direction of the CuO_2 planes is also present in untwinned single crystals and films. For instance, far-infrared spectroscopy [70] and neutron scattering on flux-line lattices [71] have shown an anisotropy between 20% and 60% in the London penetration depth, and different values of resistivity, critical current and superconducting gap have been measured along the a and the b axes [72, 73, 74].

Compared to LTS, the carrier density of YBCO is lower, which results in an increased λ_L. Because of the very short coherence length ξ, thermal fluctuations become important and defects like impurities and grain boundaries have a large impact on the

Material	T_C (K)	Δ (meV)	λ_L^a; λ_L^b; λ_L^c (nm)	ξ_{ab}; ξ_c (nm)	H_{c2}^{ab}; H_{c2}^{c} (T)
YBCO	92	20-25	150-300; $\lambda_L^a/1.2$; $\approx$1000	1-3; $\approx$0.24	250; 120
Al	1.18	0.2	50	1600	0.01 (*)
Nb	9.25	1.5	44	40	$\approx$3
NbN	16.1	1.5	$\approx$200	$\approx$5	$\approx$20

Table 2.1: Summary of the anisotropic superconducting parameters of optimally doped YBCO in form of single crystal and thin films. For comparison, the same parameters are listed also for some common LTS materials [71, 75, 76]. (*) This value is the H_c of Al.

current transport. YBCO is a superconductor of type II (for more details, see section 2.3.1) and the value of its upper magnetic critical field H_{c2} is much higher than typical values of H_{c2} in type II LTS.

The superconducting order parameter in YBCO is predominantly of the $d_{x^2-y^2}$ type, in contrast to LTS, characterized by an s-wave type order parameter. The energy gap varies in k-space according $\Delta(\vec{k}) = \Delta_0(cos(k_x a) - cos(k_y a))$ [77], which has four lobes in orthogonal directions, corresponding to the a and b directions of the CuO_2 planes, and nodal lines at 45° angle with respect to the lobes (see Fig. 2.3). Recent studies showed deviations from a pure $d_{x^2-y^2}$ symmetry, with the appearance of a subdominant complex component is (or id_{xy} at low temperature), resulting in a fully gapped quasiparticle density of states [78].

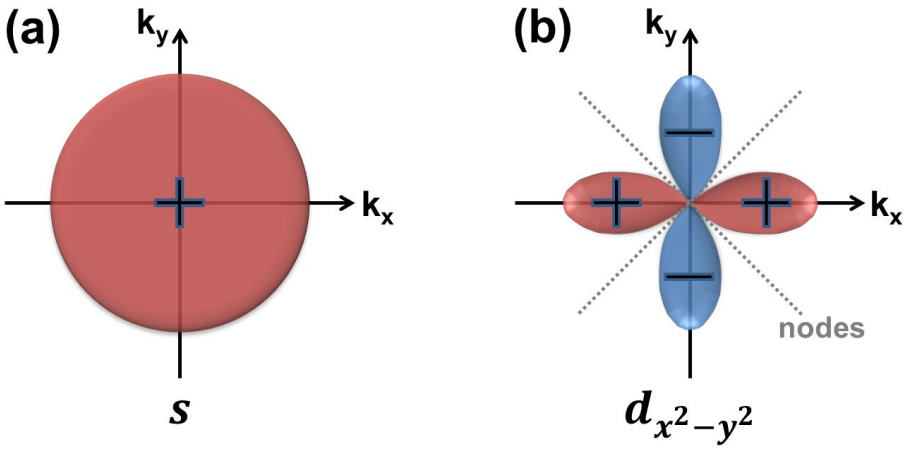

Figure 2.3: Sketch of a pure s-wave (a) and a pure d-wave (b) order parameter.

2.2.4 Nanostructures to probe different models for HTS

A remarkable number of models and theories have been proposed in the last two decades to explain the microscopic mechanism of HTS [79, 80]. Experimental anomalies have been discovered recently with neutron scattering [81], scanning tunnel microscope [82], high energy X-ray diffraction [68] and angle resolved photoemission spectroscopy [83]

measurements, which show unidirectional spin and charge order (known as *stripe order*), significantly strong at a doping $p = 1/8$, when T_C is depressed. Such evidence has been connected to the observation of the pseudogap in the excitation spectrum of high-T_C cuprates (although such hypothesis is still under debate [82, 84]), leading to the creation of the stripe models [42]. Stripes are lattice-constant wide lines on which all the charge carriers reside. The stripes only form in directions parallel to the crystal axes and they are separated by antiferromagnetic insulating regions (see Fig. 2.4). In such models the

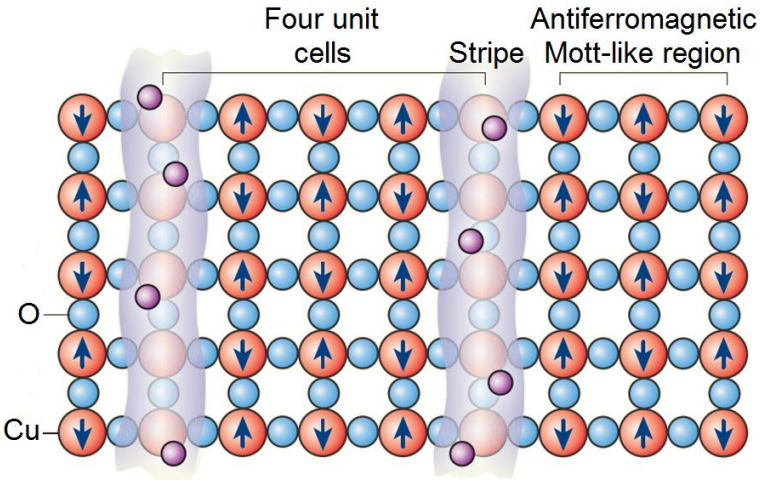

Figure 2.4: Sketch of the electronic order in cuprates, according to the stripe model. The copper oxide planes have ribbons of antiferromagnetic Mott-like order, where the spin of each electron (blue arrow) is in the opposite direction to those of its neighbors, separated by narrow stripes, where all the mobile charges (purple sphere) reside. (Adapted from [85])

pseudogap is explained by the formation of charge stripes at a temperature T_1. At a lower temperature T_2, each stripe becomes superconducting, but there is no long range phase coherence. The superconductivity phenomenon on each stripe can be explained by the confinement of charge carriers to one dimension. Then spin-charge separation occurs and superconductivity is established on each stripe due to a condensation of holons (spinless charge e bosons). The stripes couple via the Josephson effect when $T = T_C$ and long range phase coherence is established.

The exact length of a stripe is unknown, but it is believed to be somewhere between 4 and 400 nm. By fabricating structures with mesoscopic dimensions, HTS materials can be explored on the same scale of their characteristic lengths (ξ, λ_L, stripe length) and interesting and potentially important results could be produced.

Moreover, unusual phases have been associated to the stripe order, of which the most exotic is a charge-$4e$ superconducting state [33], with a corresponding fractional flux number $h/4e$. By measuring flux quantization in a variety of geometries, as in SQUID and ring loops, using 4-e striped superconductors, the existence of these novel superconducting states could be confirmed.

2.3 Key properties of superconducting nanostructures

2.3.1 Fluxoid quantization

The most important phenomenon which shows evidence of the macroscopic quantum behavior of superconductivity is the fluxoid quantization, deriving from the uniqueness of the wave function.

Inserting the expression for order parameter (eq. 2.4) into eq. (2.7), and considering the London limit in which the modulus of the wave function is not function of the spatial variables, the second Ginzburg-Landau equation writes as:

$$\vec{A} + \mu_0 \lambda_L^2 \vec{J}_s = \frac{\hbar}{e^*} \vec{\nabla} \phi \ . \tag{2.9}$$

The integration of eq. (2.9) on a closed line path around a hole in the superconductor, as depicted in Fig. 2.5a, yields to

$$\Phi + \mu_0 \oint \lambda_L^2 \vec{J}_s \, d\vec{r} = \frac{\hbar}{e^*} \oint \vec{\nabla} \phi \, d\vec{r} \, , \tag{2.10}$$

where Φ is the magnetic flux enclosed in the area surrounded by the closed path, while the sum of the two terms on the left side is called the fluxoid. To keep the order

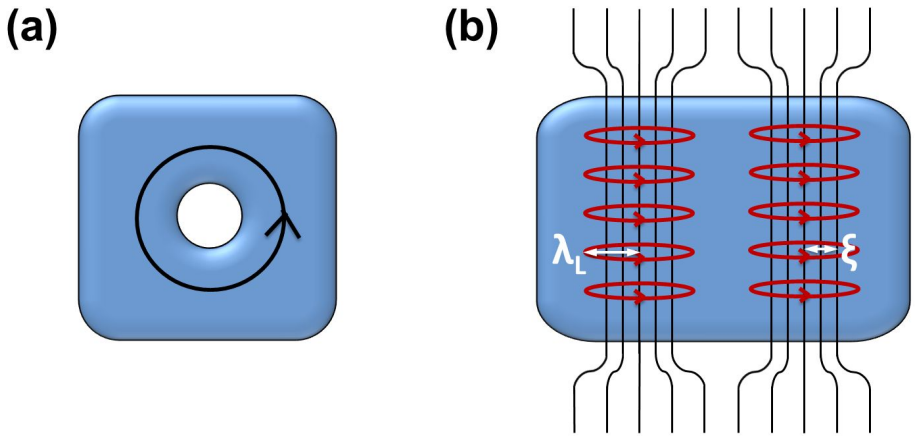

Figure 2.5: (a) Sketch of a superconducting loop. The black line shows a closed line path. (b) Sketch of Abrikosov vortices in a type II superconductor.

parameter single valued, the integral on the right side of eq. (2.10) over the full path must be an integer multiple of 2π:

$$\oint \vec{\nabla} \phi \, d\vec{r} = 2\pi n \ , \qquad n = 0, \pm 1, \pm 2, \dots \ . \tag{2.11}$$

As a consequence, eq. (2.10) writes as

$$\Phi + \mu_0 \oint \lambda_L^2 \vec{J}_s \, d\vec{r} = n \Phi_0 \ , \tag{2.12}$$

where $\Phi_0 = h/e^*$ is the flux quantum. The equation (2.12) describes the fluxoid quantization. In particular, considering an integration path where the screening currents are negligible, the second term on the left side of eq. (2.12) can be dropped ($\vec{J}_s = 0$); the total magnetic flux through a superconducting loop is quantized in units of Φ_0.

The first experiments on flux quantization [86, 87] showed a value of the superconducting flux quantum of $\approx 2 \cdot 10^{-15}$ Tm^2, that is compatible with $e^* = 2e$. Thence, the fluxoid quantization confirmed one of the main assumption of the BCS theory, namely that the superconducting fluid is composed by couples of electrons and not by single electrons.

The ratio between the London penetration depth and the coherence length $k = \lambda_L/\xi$, known as the GL parameter, identify univocally if a superconductor is of type I or of type II. In particular, Abrikosov showed that the breakpoint is at $k = 1/\sqrt{2}$, based on considerations of the energy at the interface between a superconductor and a normal conductor [88]. If $k > 1/\sqrt{2}$, a superconductor is of type II, allowing the entering of magnetic field through Abrikosov vortices. An Abrikosov vortex, also called a fluxon, consists of a normal core with radius approximately given by ξ, around which a supercurrent circulates on a length scale given by λ_L. Each vortex carries a flux quantum Φ_0 (see Fig.2.5b). On the contrary, if $k < 1/\sqrt{2}$, a superconductor is of type I, where Abrikosov vortices cannot exist.

2.3.2 Little-Parks effect

It can be shown that the fluxoid quantization implies that the free energy $F(\Psi, T)$ of the superconductor is a periodic function of the external magnetic field [89]. As a consequence, according to eq. (2.5), the critical temperature T_C, defined as the temperature at which $F(T_C) = F_n$ must also be a periodic function of the external magnetic field, since the free energy of the normal phase is independent on the order parameter. This effect has been observed for the first time by Little and Parks, that determined the $T_C(\Phi)$ oscillations through the measurement of magnetoresistance at temperature close to the critical one [90]. Their experiment, performed on a thin-walled cylinder with thickness t smaller than the London penetration depth λ_L, was to probe the fluxoid rather than the flux quantization: since $t \ll \lambda_L$, in eq. (2.12) one cannot find a closed path when the supercurrent vanishes.

In order to find an analytic expression of $T_C(\Phi)$, we may approximate the free energy in eq. (2.5) with that of a one dimensional conductor with thickness t and width w ($w, t \ll \xi$ and $wt \ll \lambda^2$). In this particular case, the condition $w, t \ll \xi$ ensures that $\Psi(\vec{r}) = |\Psi| e^{i\phi(\vec{r})}$ is constant across the cross section of the superconductor; the limit $wt \ll \lambda^2$ ensures both a uniform current density and that the kinetic energy of the superconducting charge flow dominates over the magnetic energy produced by the same current by roughly a factor λ^2/wt, so allowing to neglect the magnetic self-field terms in eq. (2.5). The result is the following [39]:

$$F = F_n + \alpha|\Psi|^2 + \frac{\beta}{2}|\Psi|^4 + |\Psi|^2 \frac{1}{2} m^* v_s^2 \,. \tag{2.13}$$

Here v_s is the superfluid velocity, defined from the relation $\vec{J}_s = e^*|\Psi|^2 \vec{v_s}$. Then, for a

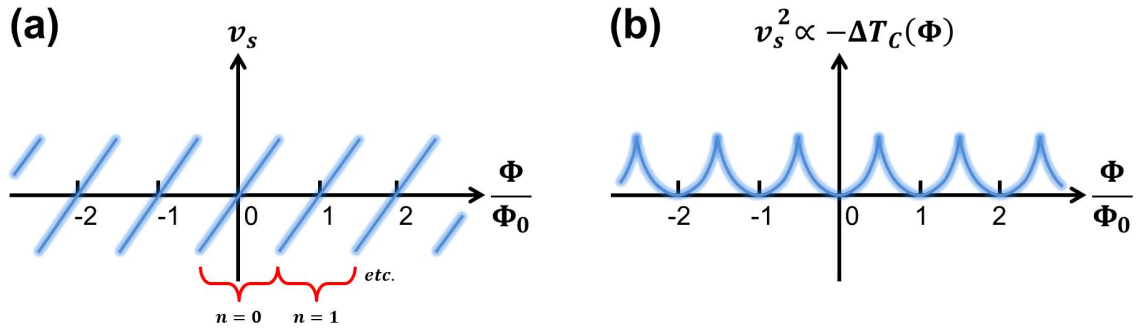

Figure 2.6: Variation of v_s (a) and v_s^2 (b) as a function of the magnetic field through the superconducting loop. The temperature oscillations according to the Little-Parks experiment are proportional to v_s^2. (Adapted from [39])

given v_s, the eq. (2.13) can be minimized to find the optimum value of $|\Psi|^2$:

$$|\Psi|^2 = \Psi_\infty^2 \left[1 - \left(\frac{\xi m^* v_s}{\hbar}\right)^2\right] , \tag{2.14}$$

with Ψ_∞ being the equilibrium order parameter deep inside the superconductor in the absence of the external field and transport current. In particular, the normal-superconductor transition occurs when $|\Psi|^2 = 0$, i.e. when

$$\frac{1}{\xi^2} = \left(\frac{m^* v_s}{\hbar}\right)^2 . \tag{2.15}$$

The superfluid velocity v_s can be also achieved from eq. (2.12), considering that the magnetic flux associated to a magnetic field H applied to a thin-wall cylinder with radius r is given by $\Phi = H\pi r^2$ at temperature close to the critical one (see Fig. 2.6a):

$$v_s = \frac{\hbar}{m^* r}\left(n - \frac{\Phi}{\Phi_0}\right) . \tag{2.16}$$

Thence, merging equations (2.15) and (2.16) we find the relation between ξ and Φ:

$$\frac{1}{\xi^2} = \frac{1}{r^2}\left(n - \frac{\Phi}{\Phi_0}\right)^2 . \tag{2.17}$$

Finally, by using in the latter equation the Ginzburg-Landau expression of the coherence length near T_C

$$\xi(T) = k_{cd}\frac{\xi_0}{\sqrt{1 - \frac{T}{T_C}}} , \tag{2.18}$$

we achieve the expression for the dependence of T_C on the magnetic field at the transition:

$$\frac{\Delta T_C(H)}{T_C} = k_{cd}\frac{\xi_0^2}{r^2}\left(n - \frac{\Phi}{\Phi_0}\right)^2 , \tag{2.19}$$

with ξ_0 the zero temperature coherence length and k_{cd} a constant, whose value differs for dirty ($\ell < \xi$) and clean ($\ell > \xi$) superconductors (ℓ being the electronic mean free path). Therefore the maximum depression in T_C, ΔT_C^{max}, is expected when $n - \Phi/\Phi_0 = 1/2$ (see Fig. 2.6b). Moreover, the ratio ξ_0^2/r^2 in eq. (2.19) shows the crucial role that the size of the superconductor plays: the loop radius can't be too large to detect variations of T_C. For instance, in case of YBCO k_{cd} is 0.55, and typical values for T_C and ξ_0 are respectively 80 K and 2 nm; in such a case, to be able to obtain measurable oscillations $T_C^{max} \approx 1$ mK, a loop radius not larger than 200 nm is required, corresponding to a field periodicity $\Phi_0/\pi r^2$ of 16 mT.

In the actual experiments the resistance oscillations as a function of H are measured rather than ΔT_C, taking advantage of the finite width of the resistive transition. The resistance modulations ΔR can be converted to ΔT_C via the following expression:

$$\Delta T_C = \Delta R \frac{dT}{dR} \, . \tag{2.20}$$

This relation is not entirely correct, since the slope of the transition dT/dR depends on the magnetic field H, causing the inferred $\Delta T_C(H)$ to depend on the resistance choice within the transition. However, it still gives the best approximation for the determination of ΔT_C from magnetoresistance oscillations [39].

2.3.3 Josephson effect

In 1962 Josephson published a theoretical paper [91] predicting the existence of two remarkably effects. The basic idea of the DC-Josephson effect is that S-I-S junctions, made by two superconducting electrodes separated by a thin insulating barrier, may sustain a non-dissipative (zero-voltage) superconducting current I_S:

$$I_S = I_C \sin\phi \, . \tag{2.21}$$

Here, $\phi = \phi_2 - \phi_1$ is the phase difference between the wavefunctions describing the order parameter in the two electrodes and I_C is the critical current, which is the maximum supercurrent the junction can sustain without dissipation. The AC-Josephson equation tells instead that the phase varies linearly with time, if a fixed voltage V is applied across the junction:

$$\frac{d\phi}{dt} = \frac{2e}{\hbar} V \, . \tag{2.22}$$

Both effects have been verified by experiments shortly after Josephson prediction [92]. Moreover, it soon became clear that the Josephson effects exist not only in S-I-S junctions, but also in other kinds of the so-called weak links, that is, short sections of superconducting circuits where the critical current is substantially suppressed (see Fig. 2.7).

Among the different types of weak links, we will focus on superconducting narrow bridges with thickness t, width w and length l connecting two bulk electrodes of the same material (see Fig. 2.7c).

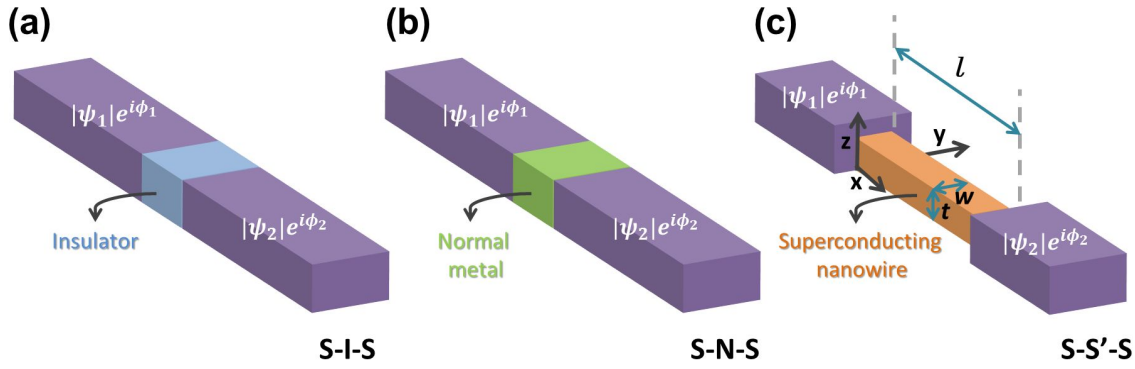

Figure 2.7: Different types of weak links: (a) superconductor-insulator-superconductor (S-I-S); (b) superconductor-normal metal-superconductor (S-N-S); (c) superconductor-superconducting narrow bridge-superconductor (S-S'-S).

- In the limit of short ($l \ll \xi$) and one dimensional ($w, t \ll \xi$) bridge, the current-phase relation (CPR) between the wide electrodes, derived by Aslamazov and Larkin from the GL equation (2.7), has the following expression:

$$J_s^{AL} = \frac{\Phi_0}{2\pi\mu_0\lambda_L^2 l}\sin\phi \,. \tag{2.23}$$

  As a consequence of this equation, all the weak links are characterized by a sinusoidal CPR near T_C, where ξ diverges, similarly to superconducting tunnel junction (eq. 2.21).

- Increasing the bridge length, the current-phase relation close to T_C evolves from sinusoidal to saw tooth-like (see Fig. 2.8), as predicted by Likharev and Yakobson [93]. In particular, if $l \leq 3.49\xi$ an ideal Josephson behavior, described by a single valued CPR, is expected. If $l > 3.49\xi$, a multivalued CPR, strongly connected to depairing effects, characterizes the bridge. The maximum current saturates in fact for $l > 10\xi$ at a value given by the depairing current density, above which the order parameter (pair density) is locally suppressed, i.e. due to the nucleation of phase slip centers. Such unstable states are described by the lower reverse branch of the current-phase relation. As regards to the stable branch, instead, it can be derived from the GL equations, considering that in the limit of long ($l \gg \xi$) and one-dimensional ($w, t \ll \xi$ and $wt \ll \lambda^2$) bridge the free energy writes as in eq. (2.13). Defining the following order parameter inside the wire:

$$\Psi^{LY}(x) = |\Psi^{LY}|\, e^{ix\phi/l} \,, \tag{2.24}$$

  the modulus of the wave function can be derived, as previously done in eq. (2.14):

$$|\Psi^{LY}|^2 = |\Psi_\infty^{LY}|^2 \left[1 - \left(\frac{\phi\xi}{l}\right)^2\right] \,, \tag{2.25}$$

  where $|\Psi_\infty^{LY}|^2$ is the modulus of the wave function at zero phase difference. Finally the current-phase relation for a long one-dimentional bridge can be determined,

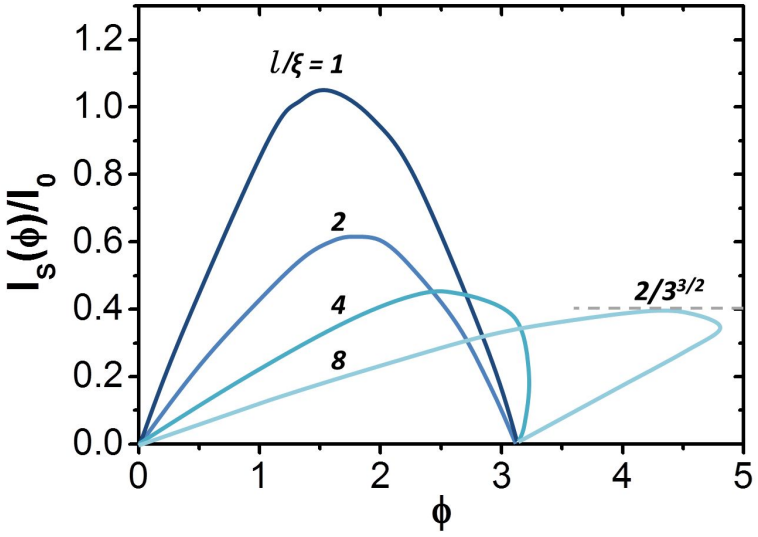

Figure 2.8: Current phase relation for different bridge lengths. The currents are normalized to the value $I_0 = \Phi_0/2\pi\mu_0\lambda_L^2\xi$. (Adapted from [93])

inserting eq. (2.24) and eq. (2.25) into eq. (2.7):

$$J_s^{LY} = \frac{\Phi_0}{2\pi\mu_0\xi{\lambda_L}^2}\left[\left(\frac{\xi}{l}\right)\phi - \left(\frac{\xi}{l}\right)^3\phi^3\right] . \tag{2.26}$$

Maximizing the previous equation with respect to ϕ/l, we determine the maximum value ϕ_d of the phase gradient

$$\phi_d = l/\sqrt{3}\xi , \tag{2.27}$$

corresponding to the depairing critical current density J_d given by:

$$J_d = \frac{\Phi_0}{3\sqrt{3}\pi\mu_0\lambda_L^2\xi} . \tag{2.28}$$

It is worth noticing that, since $l \gg \xi$, this CPR is defined in a range $-l/\sqrt{3}\xi < \phi < l/\sqrt{3}\xi$, which is much larger than that of an ideal Josephson junction (2π).

- The effect of increasing the width of the bridge on the current-phase relation, studied by Likharev [94], is shown in Fig. 2.9. In particular, a different regime is expected for bridges wider $w > 4.44\xi$, if $l > 3.49\xi$, due to the coherent motion of Abrikosov vortices inside the structure. However, the current can be considered homogeneous in the limit $t < \lambda_L$ and $w < \lambda_P$, with $\lambda_P = \lambda_L^2/t$ the Pearl length, allowing to reduce the GL equations to the 1-dimensional form[95]. As a consequence, the stable branch of the CPR writes again as eq. (2.26), with the only difference that the maximum critical current density is not given by depairing effects, i.e. phase slips, but by Abrikosov vortices, driven by the Lorentz force, overcoming the bridge edge barrier. According to Bulaevskii et al. [96], this occurs for a phase difference $\phi_v = l/2.718\xi \simeq 0.64\phi_d$. As a consequence,

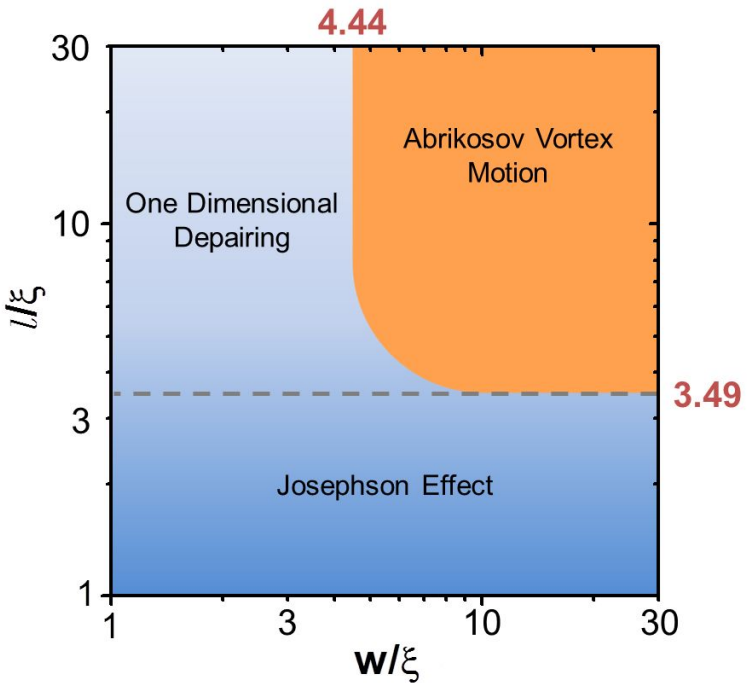

Figure 2.9: Likharev criteria for the origin of the current phase relation in SS'S weak links, for different bridge dimensions. (Adapted from [94])

the critical current density J_v due to vortex entry is smaller than the depairing critical current:

$$J_v \simeq 0.826 J_d \, . \tag{2.29}$$

For $|\phi| < \phi_v$ the expression of the CPR (eq. 2.26) can be reasonably approximated by the linear term:

$$I = \frac{\Phi_0}{2\pi L_k}\phi \, , \tag{2.30}$$

where $I = J_v \cdot wt$ is the supercurrent passing through the bridge and L_k is the kinetic inductance of the bridge, given by $(\mu_0 \lambda^2 l)/(wt)$. Indeed, the inductance of a bridge with cross section $wt \ll \lambda^2$ is dominated by the kinetic inductance with a negligible contribution of the geometric inductance $L_g \simeq \mu_0 l$.

2.3.4 Thermal suppression of superconductivity

In systems with reduced dimensionality it can be observed that the superconducting phase transition is frequently not sharp and the measured dependence of the sample resistance $R(T)$ in the vicinity of the critical temperature T_C may have a finite width, even in absence of any sample inhomogeneity. This broadening is due to thermal fluctuations. In 1D wires ($w, t \ll \xi$) such fluctuations, called thermally activated phase slips (TAPS), with spacial extensions of the order of the coherence length, hence of the wire diameter, disrupt locally the flow of supercurrent, thereby imparting a non-zero resistance to the wire [97, 98, 99]. In 3D wires instead the resistive state is triggered by vortices crossing the wire, appearing below T_C even at low bias currents [96, 100].

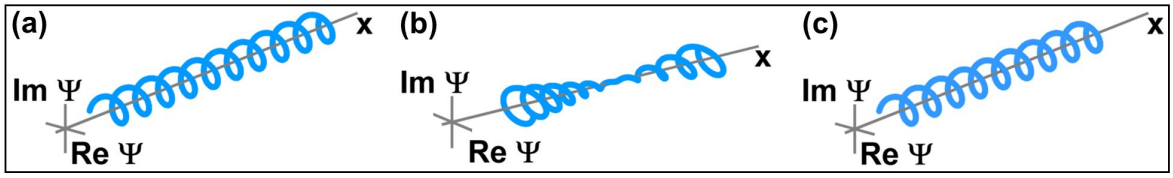

Figure 2.10: Polar plot of the complex GL wave function (a) before, (b) during and (c) after a phase slip event. (Adapted from [39])

Eventually, in 1D wires the broadening in the transition may even lead to a non-vanishing resistivity down to $T = 0$: the physical reason behind such smearing of the transition has been attributed to temperature-independent quantum phase slip events (QPS) [101]. However, we will not focus on them since they've been observed only in LTS nanostructures so far [102].

Phase slips

Little in 1967 introduced the concept of TAPS to explain the presence of a finite resistance below T_C in one dimensional superconducting nanowires, with width w, thickness t and length l [97]. Thermal fluctuations cause a deviation of the superconducting order parameter from its steady state, which is represented in the Argand plane by an helix of pitch $2\pi/q$ (with $q = \phi/l$ the phase gradient) and radius $|\Psi|$ (see Fig. 2.10a). In particular, the modulus can be suppressed temporally down to zero at some point inside the wire. As a consequence the phase, becoming unrestricted, can "slip", but only by 2π or integer multiples of it, since the order parameter in the macroscopic leads is defined modulo 2π. At the end of this process the system returns in its initial steady state, accumulating a net phase shift 2π (provided phase slips are sufficiently rare, we can ignore fluctuations with $|n| \geq 2$, restricting $n = \pm 1$). Schematically, this process can be mimicked in the Argand plane, considering that the helix tightens up until its radius reaches zero at some point (see Fig. 2.10b), a phase slip occurs and the radius returns to $|\Psi|$.

According to eq. (2.22), each phase slip event determines a voltage drop V across the wire. However, if a bias current is not applied, the net voltage drop is zero, since the number of positive ($n = +1$) and negative ($n = -1$) phase slips is stochastically the same. Vice versa, if a current $I \propto |\Psi|^2 \Delta\phi$ is applied, a phase gradient is created along the wire, favoring positive phase slips: thence, a non-zero voltage drop is present due to TAPS, causing the appearance in the wire of a resistance $R = V/I$, different than zero even below T_C [103]. Quantitative theories predict that this resistance R is determined by the activation exponent

$$R(T) \propto \exp\left(-\frac{\Delta F(T)}{k_B T}\right) , \tag{2.31}$$

where k_B is the Boltzmann constant and $\Delta F(T)$ is the energy barrier for phase slips, depending on temperature and going to zero at $T = T_C$, which is proportional to the product of the condensation energy density and the cross section volume $\xi(T)wt$ in

which superconductivity can be destroyed by thermal fluctuation [98, 99]:

$$\Delta F(T) \propto \frac{\mu_0 H_C^2(T)}{2}\xi(T)wt \ . \tag{2.32}$$

In particular, according to Langer-Ambegaokar-McCumber-Halperin (LAMH), who developed this theory, eq. (2.31) writes as [98, 99]

$$R_{LAMH}(T) = \left(\frac{h}{4e^2}\right)\left(\frac{\hbar\Omega_D}{k_B T}\right)\exp\left(-\frac{\Delta F(T)}{k_B T}\right) \ , \tag{2.33}$$

where $\Omega_D = (l/\xi)\sqrt{(\Delta F/k_B T)}\tau_{GL}^{-1}$ is the attempt frequency of phase slip events, and $\tau_{GL} = \pi\hbar/8k_B(T_C - T)$ is the GL relaxation time. The total resistance of the wire close to the transition can be expressed as the parallel combination of the resistance due to phase slip events and the normal resistance of the wire R_N:

$$R(T) = \left(R_{LAMH}^{-1}(T) + R_N^{-1}\right)^{-1} \ . \tag{2.34}$$

However, the prefactor (i.e. the attempt frequency) in the LAMH expression (eq. 2.33) has been recently shown to be incorrect [104]. As a consequence, the resistance of the wire (eq. 2.31) can be better approximated with the "Little fit" [102], where the normal resistance of the wire is explicitly included in the prefactor:

$$R_{Little}(T) = R_N \exp\left(-\frac{\Delta F(T)}{k_B T}\right) \ . \tag{2.35}$$

Vortex slips

In case of 3D wires ($w > 4.44\xi$, $l > 3.49\xi$), the resistance below the transition can be still written according to the form of eq. (2.31), but the energy barrier for phase slips ΔF has to be substituted with that for vortex entry, which can be written as a function of position y (parallel to the width) in presence of a uniform bias current as follows [96]:

$$\Delta U(y, I_b, T) = \mu^2 \epsilon_0 \left[\ln\left(\frac{2w}{\pi\xi}\sin\frac{y\pi}{w}\right) - \frac{I_b}{\mu^2 I_0}\frac{y\pi}{w}\right] \ , \tag{2.36}$$

with $I_0 = \Phi_0 t/4\mu_0\lambda_L^2$ and $\epsilon_0 = \Phi_0^2 t/4\pi\mu_0\lambda_L^2$ the characteristic energy of a vortex in thin films. μ^2 describes the order parameter suppression due to the bias current:

$$\mu^2 = \frac{|\Psi|^2}{|\Psi_\infty|^2} = 1 - \left(\frac{\phi\xi}{l}\right)^2 \ . \tag{2.37}$$

In the limit of zero bias, the resistance of the wire affected by vortex tunneling below T_C writes as [105]

$$R_v(T) = R_\square\sqrt{2\pi}(1+\pi)\frac{l\xi}{w^2}\left(\frac{\mu^2}{k_B T}\frac{\Phi_0^2 t}{4\pi\mu_0\lambda_L^2}\right)^{3/2}\exp\left(-\frac{\mu^2}{k_B T}\frac{\Phi_0^2 t}{4\pi\mu_0\lambda_L^2}\ln\frac{w}{\pi\xi}\right) \ , \tag{2.38}$$

where $R_\square$ is the sheet resistance of the wire and μ^2 is equal to 1 in the zero bias limit.

2.4 Nanowire-based superconducting sensors

In recent years, superconducting nanowires have been employed in nanosized quantum limited sensors, allowing the detection of magnetic field and photons with unprecedented resolution [26, 34].

In particular, nanowires are substituting traditional tunnel Josephson junctions in superconducting quantum interference devices (SQUIDs), which are extremely sensitive sensors of magnetic flux. The development of nanosized devices is boosted by the possibility to achieve performances in terms of sensitivity and low noise, which could allow the investigation of few atomic spins (for more details, see chapter 6).

On the other hand, superconducting nanowires for single photon detection (SNSPDs) have gained great interest during the last decade [34, 106]. Indeed the theoretical performances of these devices in terms of detection efficiencies (close to 100% up to the near infrared wavelength region), together with the extremely low dark counts (< 1 s^{-1}), fast time response (few ps) and low time jitters (< 30 ps) [34], are very attractive for fast detector applications (for more details, see chapter 8).

In what follows, we will briefly summarize the basics of the SQUIDs, either when they employ standard Josephson junctions with sinusoidal CPR, and when Josephson junctions are substituted by nanowires.

2.4.1 Dayem nanobridge Superconducting QUantum Interference Devices

The dc-SQUID consists of two Josephson junctions in a superconducting loop (see Fig. 2.11a).

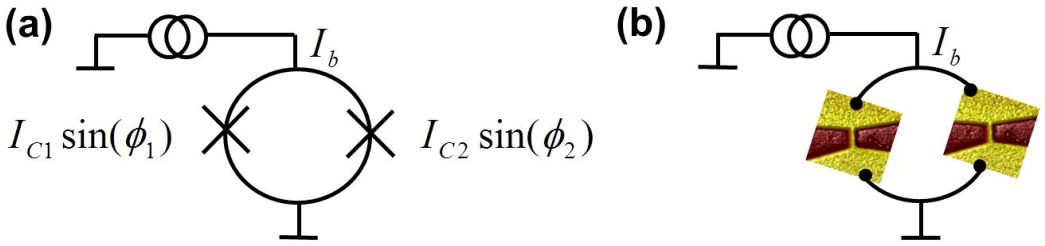

Figure 2.11: (a) Sketch of a typical SQUID, implementing tunnel Josephson junctions. (b) Sketch of a Dayem bridge nanoSQUID, where the Josephson junctions are substituted by nanowires.

The total current through the SQUID is given by adding the currents flowing through each junction, according to eq. (2.21):

$$I_{SQUID} = I_{C1}\sin\phi_1 + I_{C2}\sin\phi_2 \ . \tag{2.39}$$

In a magnetic field, and neglecting the contribution of the inductance of the SQUID arms, ϕ_1 and ϕ_2 are related to each other by the flux through the loop area. In the closed path of eq. (2.10) each junction contributes with a phase difference across the junction. Thence, we obtain

$$2\pi n = \phi_1 - \phi_2 + 2\pi\frac{\Phi}{\Phi_0} \ , \tag{2.40}$$

where Φ is the external magnetic flux. From eqs. (2.39-2.40), then using simple algebraic relations, it follows that the maximum SQUID supercurrent modulates as a function of the magnetic flux through the loop according to (see blue curve in Fig. 2.12a):

$$I_{SQUID} = 2I_C \left| \cos\pi \frac{\Phi}{\Phi_0} \right| , \tag{2.41}$$

where we have assumed the SQUID to be symmetric, i.e. both junctions carrying the same critical current $I_{C1} = I_{C2} = I_C$.

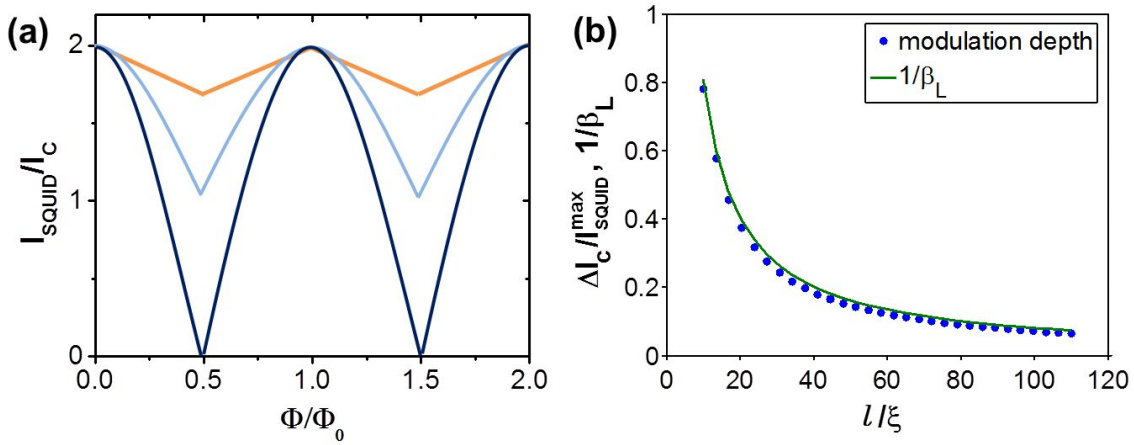

Figure 2.12: (a) Modulation of the critical current as a function of the applied magnetic flux for a standard SQUID, whether the contribution of the inductance is negligible (*blue curve*, $\beta_L = 0$) or it has to be considered (*light blue* and *orange curve*, $\beta_L = 1$ and 5, respectively). (Adapted from [107]) (b) Calculated relative modulation depth of a Dayem bridge nanoSQUID as a function of the wire length.

If we now consider also the contribution of the inductances L_1 and L_2 of the two SQUID arms, the resulting magnetic field pattern will be modified. The total supercurrent through the SQUID loop is still given by eq. (2.39), while the equation (2.40), in its more general form, writes as

$$2\pi n = \phi_1 - \phi_2 + 2\pi \frac{\Phi}{\Phi_0} + 2\pi\beta_{L,1}\sin\phi_1 + 2\pi\beta_{L,2}\sin\phi_2 , \tag{2.42}$$

with $\beta_{L,1} = L_1 I_{C1}/\Phi_0$ and $\beta_{L,2} = L_2 I_{C2}/\Phi_0$ expressing the effect of the self-induced field. To determine the modulation of the critical current as a function of the applied magnetic field, one value for Φ/Φ_0 and one of the junction phase difference (either ϕ_1 or ϕ_2) have to be assumed, then the phase of the second junction has to be varied until eq. (2.42) is satisfied. The values for ϕ_1 and ϕ_2 are substituted in eq. (2.39) to find the total current. The maximum value for I, after repeating this procedure for all initial values of ϕ_1 and ϕ_2, is the critical current for the value of Φ/Φ_0 previously chosen. By iterating this procedure for different values of Φ/Φ_0, the final $I_{SQUID}(\Phi)$ characteristic is achieved (see light blue and orange curves in Fig. 2.12a) [108]. The modulation depth of the magnetic pattern is reduced, according to the value of the screening inductance factor $\beta_L = L_{loop} I^{max}_{SQUID}/\Phi_0$. In particular, Tesche and Clarke

[109] proved that, in the limit $L_{loop}I_{SQUID}^{max} \gg \Phi_0$, with L_{loop} total inductance of the SQUID loop, the scaling behavior of the modulation depth ΔI_C on β_L is the following:

$$\frac{\Delta I_C}{I_{SQUID}^{max}} = \frac{1}{\beta_L} \,. \tag{2.43}$$

In Dayem bridge nanoSQUIDs, the two Josephson junctions are substituted by two nanowires (see Fig. 2.11b). Depending on the nanowire dimensions, the CPR may change from sinusoidal single valued to "sawtooth" like multivalued (see Fig. 2.8) and the magnetic pattern may consequently be nonstandard. In particular, if YBCO nanowires are used ($w, t \gg \xi$), the current-phase relation of each wire inside the loop assumes the form of eq. (2.30), and the inductance contribution cannot be ignored. The $I_{SQUID}(\Phi)$ characteristic can be numerically calculated, following the aforementioned procedure, but substituting the sinusoidal CPR of the Josephson junctions in eq. (2.42) with the CPR of the nanowires (eq. 2.30). In Fig. 2.12b we show the calculated relative modulation depth as a function of the wire length. Here, for simplicity we neglected the contribution of the SQUID arms on the total inductance. The solid line is the expression for $1/\beta_L$, assuming that the total loop inductance is given by the kinetic inductance of the wires. Indeed, as it can be seen from Fig. 2.12b, the scaling behavior of the modulation depth ΔI_C on β_L is still given with good approximation by eq. (2.43).

3

Growth and characterization of YBCO films

The possibility to nanostructure oxide superconductors both for fundamental studies and for applications is strongly related to crystalline structure and surface morphology of these materials, which are a direct result of the thin film growth, influenced by the deposition conditions and the substrate properties.

In this chapter we will discuss the work done to optimize the thin film growth of YBCO on various substrates.

3.1 Untwinned and twinned YBCO

Highly textured YBCO thin films are generally deposited by sputtering or by pulsed laser deposition (PLD) at temperatures in the range 700 - 900 °C. Due to these high temperatures, YBCO grows in the oxygen depleted tetragonal phase ($0.6 \leq \delta \leq 1$). During the subsequent cool down in highly-pressurized oxygen atmosphere, the oxygen atoms diffuse into the film, causing a phase transition from tetragonal to orthorhombic. During this step, four different twin orientations are formed: in order to accomodate strain energy, the diagonals of the *a*-*b* plane of the emerging orthorhombic phase adopt the directions of the diagonals of the *a*-*b* plane of the tetragonal phase [110, 111] (see Fig. 3.1). Two twin orientations, named S_1^+ and S_2^-, align along the [110] diagonal of the tetragonal *a*-*b* plane, while a second pair, formed by the two orientations S_1^- and S_2^+, align along the $[\bar{1}\bar{1}0]$ diagonal of the tetragonal *a*-*b* plane. S_1^+ and S_2^-, as well as S_1^- and S_2^+ can be transferred into each other by a reflection in a $\{110\}$ plane, while S_1^+ and S_2^+, as well as S_1^- and S_2^- can be transferred into each other by a 90° rotation. The orientation angle between S_1^+ and S_1^- and between S_2^+ and S_2^- is $2\eta = 2[\arctan(b/a) - 45°] = 1.04°$, using the lattice parameters of sec. (2.2.1).

The final twinning state in the *a*-*b* plane of the YBCO film is strongly dependent on the in-plane symmetry of the substrate, since in-plane lattice parameter of the film are subject to a strain induced by the substrate.

In most of the cases, none or only one twin pair is suppressed, and consequently the YBCO films are *twinned*. For instance, the substrates with a cubic symmetry, as the (001) oriented MgO, $SrTiO_3$ and $LaAlO_3$, have the in-plane lattice which can be transformed into itself both by a 90° rotation and by a reflection in a $\{110\}$ plane: as

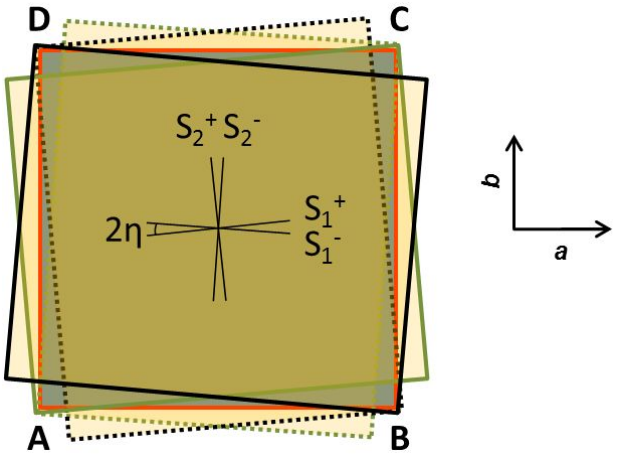

Figure 3.1: Epitaxial relationship between the tetragonal phase (the ABCD square, highlighted by a red outline) and the orthorhombic phase of YBCO (the twin orientations S_1^+ and S_2^- have been outlined in green, with solid and dotted line respectively, while the twin orientations S_1^- and S_2^+ have been outlined in black, with solid and dotted line respectively).

a consequence, all the four twinning orientations S_1^+, S_1^-, S_2^+, S_2^- are equivalent and will be present in the YBCO films [111]. In twinned YBCO films, a random exchange of the a and b axis is present, and the in-plane anisotropy of the electronic structure, mentioned in sec. 2.2.3, is completely lost. All the physical properties, i.e. the cell dimensions, the critical current densities, measured in the two orthogonal in-plane directions will be equal, corresponding to an average of the a and b axes. Moreover twin planes, separating domains in which a and b directions interchange, act as defects (pinning centers), which weaken locally the superconductivity and become preferential channels for magnetic-flux penetration [112].

The YBCO films are instead *untwinned* if they grow on substrates which suppress both the twin pairs. In this case, the random exchange of the a and the b axes is eliminated: the pristine crystal structure and the superconducting properties, related to the presence of CuO chains along the b direction, are preserved, so enabling the study of the angle resolved electronic properties in the ab plane [73]. To remove the twinning domains, up to now substrates with vicinal angle [73, 113] have been used.

3.2 Choice of the substrates

The achievement of homogeneous and epitaxial YBCO films and the definition of their epitaxial orientation are strongly related to the initial choice of the substrate. As already discussed in sec. (3.1), the crystallographic structure of YBCO, and its superconducting propertes, may differ from that of the parent bulk, when it is prepared in epitaxial thin film form. This is due to the biaxial stress determined by the substrate that results in a strained film structure. A relevant parameter quantifying such stress is the film/substrate lattice mismatch δ^m, defined as

$$\delta^m = \frac{a_{substrate} - a_{film}}{a_{substrate}} , \tag{3.1}$$

where $a_{substrate}$ and a_{film} are respectively the in-plane lattice parameters of the substrate and the film.

To minimize defects, the use of substrates with lattice parameters very close to those of YBCO should be in principle considered. For this reason substrates as $SrTiO_3$ (STO) and $LaAlO_3$ (LAO) are commonly used, which results in a very small tensile ($\delta^m = +2.2\%$ for STO) and compressive ($\delta^m = -0.7\%$ for LAO) stress of the YBCO cell. However, STO cannot be used in devices where a good coupling with the microwave radiation is required, because of its high dielectric constant and loss tangent, especially at low temperature; LAO instead is affected by twin boundaries that have been reported to cause inhomogeneities in the YBCO films [114], negatively affecting for example their microwave properties [115]. Moreover, both these crystals have a cubic cell, favoring the growth of twinned YBCO films.

MgO crystals, instead, although presenting a large lattice misfit with YBCO (9% in case of (001) orientation), are free from twinning and strain defects. They have a thermal expansion coefficient ($\approx 1 \cdot 10^{-5}$ K^{-1} at 273 K) similar to that of YBCO, and are characterized by low dielectric constant (≈ 10) and microwave losses (loss tangent $\approx 10^{-5}$ at 10 GHz and 90 K) [116]. Moreover, the usage of (110) oriented MgO substrates, with even larger lattice misfit with the two in-plane directions, introduces a strong in-plane anisotropy.

We have chosen MgO (110) as the main substrate to deposit high quality YBCO thin films. However, we have also optimized the growth of YBCO on MgO (001), STO (001) and LAO (001) substrates. These films have been used both for comparison and, as it will be clarified during the next sections, for some specific experiments.

3.3 Thin film growth

The growth of YBCO thin films is rather complicated: this is mainly a consequence of the strong dependence of the compound properties on the ratios of different elements (in particular the oxygen doping) and of the difficulty to keep the correct stoichiometry in the films. The homogeneity and smoothness of YBCO thin films are crucial requirements to get reliable transport properties at the nanoscale. They are strongly dependent on the employed deposition techniques and on the deposition conditions of thin films.

High quality thin films of YBCO have been fabricated during the years by various methods such as rf magneton sputtering, high-pressure dc sputtering, thermal co-evaporation, chemical vapor deposition and pulsed laser deposition (PLD). Among these techniques, high-pressure dc sputtering and PLD, each of them with its pros and cons, are regarded as the most effective methods to produce stoichiometric films.

We have deposited YBCO thin films by PLD on different substrates. A sketch of the used system is in Fig. (3.2). The basic working principle of this tecnique is the following: a pulsed high-energetic laser beam is focused on a target, resulting in the ablation of some material. This mixture of atoms, molecules, ions and clusters forms the so-called *plasma plume*, which expands from the target and condenses on a heated substrate placed in front of the target.

For each substrate, different parameters have to be considered in order to get films

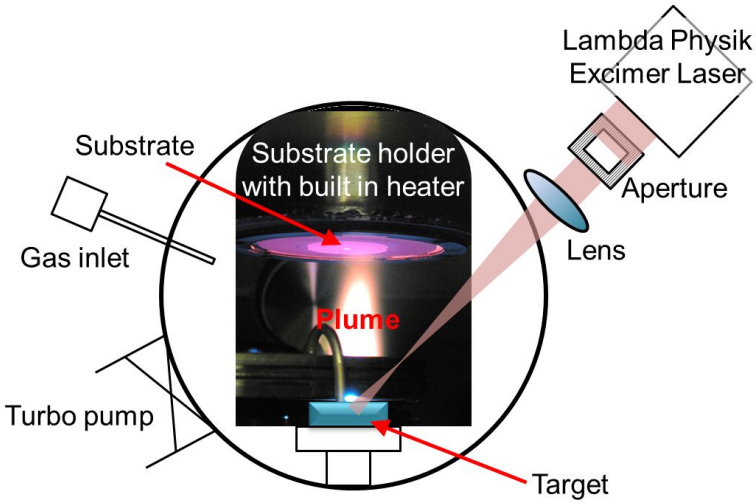

Figure 3.2: A sketch of the PLD system used in this thesis.

with the required properties. The parameters influencing the size and shape of the plume and that control the surface kinetics of the deposited atoms, are the fluence and pulse repetition rate of the laser, the oxygen pressure (p_{dep}) and substrate temperature (T_{dep}) during the deposition, the distance between target and substrate (d_{T-S}). As already mentioned in sec. (3.1), the oxygen diffusing into the film during the cool down to ambient temperature is responsible of the doping level of YBCO films. The post-annealing conditions (oxygen pressure p_{ann} and cooling rate) are therefore extremely important.

We have optimized the growth conditions for 50 nm thick YBCO films on four different substrates. Some parameters, like the laser fluence (2 J/cm^2) and the laser pulse repetition rate (4-6 Hz) have been fixed independently of the substrate. The other parameters are listed in Table (3.1) for different substrates.

Parameter	MgO(110)	MgO(001)	LAO(001)	STO(001)
T_{dep} (°C)	750	770	810	770
p_{dep} (mbar)	0.7	0.7	0.6	0.6
d_{T-S} (mm)	53.5	53.5	53.5	53
p_{ann} (mbar)	900	900	900	900
Cooling rate (°C/min)	5	5	5*	5*

Table 3.1: Parameters used to deposit YBCO thin films by PLD on different substrates. The starred cooling rates refer to films that have been annealed one hour at 550 °C after the deposition.

The deposition parameters have been chosen to get the right compromise between surface smoothness and critical temperature T_C of the film. In particular, an increase of T_{dep} leads to a high superconducting critical temperature at the expense of the surface morfology; a reduced T_{dep} leads to smooth surfaces at the expence of the critical temperature and sharpness of the superconducting transition.

Depending on the substrates, the YBCO thin films are characterized by different structural and transport properties. In the next two sections, we will focus on the morphological and electrical characterization of YBCO films deposited on MgO (110) and LAO (001), representing the substrates used in my thesis work.

3.4 YBCO films on MgO(110)

The properties of the YBCO films deposited on (110) oriented MgO substrates are strongly related to the large mismatch between the in plane lattice parameters of YBCO ($a = 3.82$ Å, $b = 3.89$ Å) and those of MgO ($[0, 0, 1] = 4.21$ Å, $[1, -1, 0] = 5.96$ Å).

As a first consequence, Resistance vs Temperature $R(T)$ measurements show a critical temperature T_C (defined at the onset of the superconducting transition) of ≈ 86 K, well below the T_C of the bulk, but still among the highest values reported in literature so far for MgO substrates [117]. The homogeneity of the films is proven by a rather sharp transition of about 1 K.

Surface morphology has been studied by Atomic Force Microscopy (AFM) and Scanning Electron Microscopy (SEM) (see Fig. 3.3). The films present smooth surfaces, characterized by the typical c-axis domains with a tridimensional spiral-like growth, few holes and an average roughness of 1.5-2 nm.

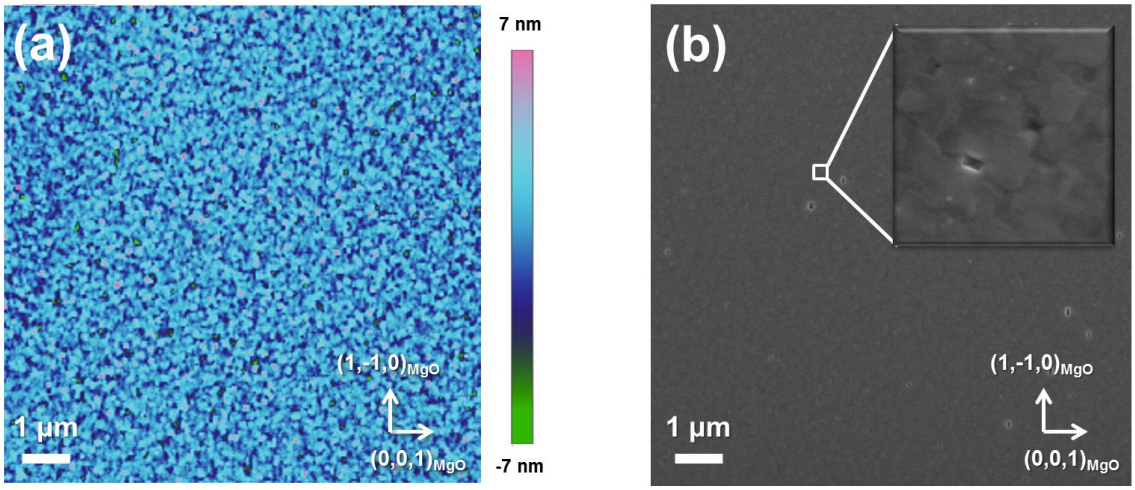

Figure 3.3: (a) AFM image of a YBCO film on MgO (110), showing a roughness of 1.5 nm, slightly higher than the thickness of single atomic cell, on a 10×10 μm^2 region. (b) SEM picture on the same film of panel (a). In the inset, c-axis spiral domains are visible, with an average size of about 50-100 nm.

The structural properties have been determined by X-Ray Diffraction (XRD) analysis. Symmetric $2\theta - \omega$ scans confirm that the films are highly crystalline and c-axis oriented (see Fig. 3.4). From the angular position of the (0,0,n) peaks a value of 11.71 Å could be estimated for the c-axis: such elongation could be attributed to a compressive in-plane strain induced by the substrate. Alternatively, the hyphotesis of slighly underdoped films can be considered, supported by the reduced values of T_C

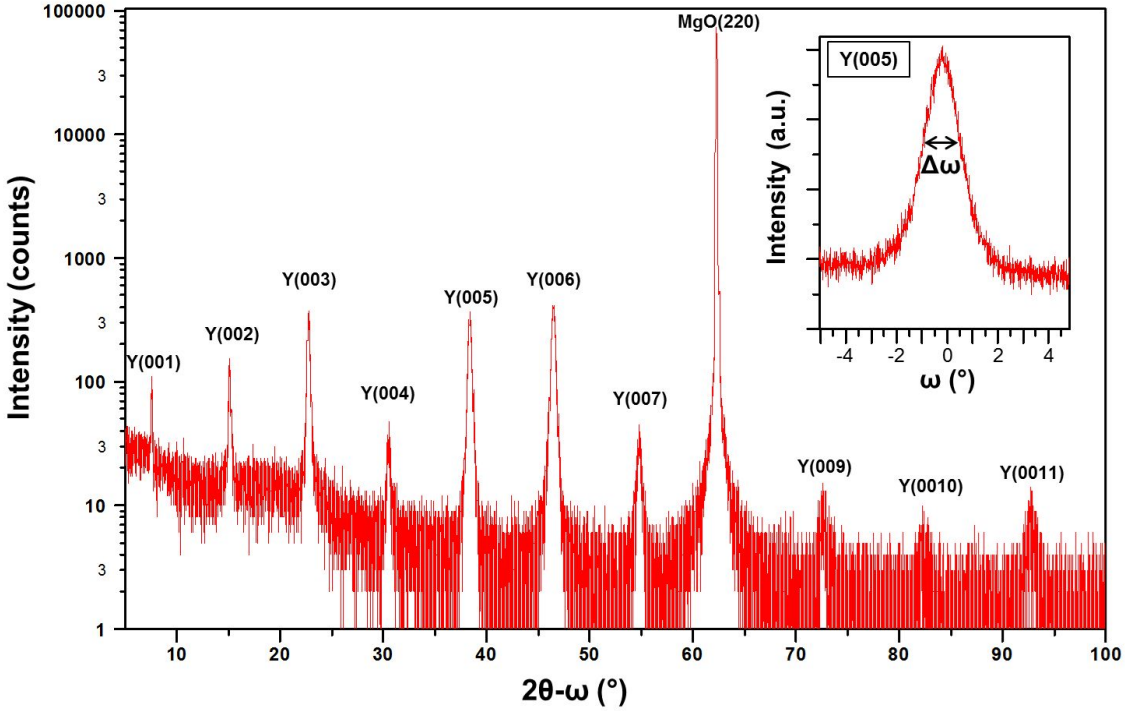

Figure 3.4: XRD $2\theta - \omega$ scan of a 50 nm thick YBCO film on MgO (110). Only $(00n)$ YBCO reflections are observed. In the inset, a rocking curve of the (005) YBCO reflection is shown, with a FWHM of $\approx 1°$.

we have measured in these films. The rocking curves of the (0,0,n) peaks have been also measured, with a full width at half maximum (FWHM) of the peaks, $\Delta\omega \approx 1°$, supporting the idea of highly textured films.

The in-plane texture of the films has been examinated by ϕ-scans (where ϕ is the rotation angle around the sample surface normal direction) and pole-figure analysis (where the diffracted intensity is collected by varying both ϕ and χ representing the tilt angle from the sample surface normal direction). In particular, the reflections from the (103) planes of YBCO in the ϕ-scans (see Fig. 3.5a) show that the in-plane orientation of the YBCO unit cell is parallel to the substrate. Four reflections are visible, but the typical 90° symmetry of twinned films is broken by the appearance of two splitted peaks at 90° and 270°. Polar figures (see Fig. 3.5b) confirm that the in-plane symmetry is 180°. The elongation of the two peaks at $\phi = 0°$ and $\phi = 180°$, together with the splitting of the peaks at $\phi = 90°$ and $\phi = 270°$, highlights the presence of a more complex in-plane texture.

However, these analyses cannot give conclusive indications about the twinning in the films and the film-substrate orientation relationship: the (103) and the (013) reflections of YBCO, associated to the in plane presence of the a and the b axis respectively, are too close to be resolved, because the length of these two axes is similar. To resolve the splitting of the reflections associated to a and b, we have performed $2\theta - \omega$ maps around the (038)-(308) reflections, which in relaxed films should be at $2\theta = 105.31°$ and $2\theta = 106.80°$ respectively. In our case, fixing $\phi = 0°$, we observe only one peak,whose maximum is at $2\theta = 105.86°$ (see Fig. 3.6a); fixing $\phi = 90°$, we observe again only

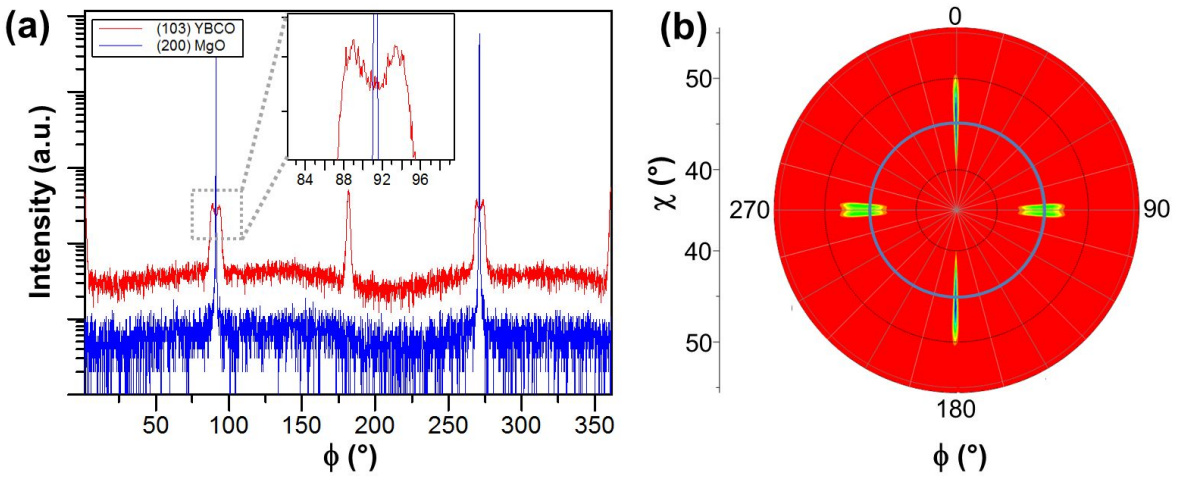

Figure 3.5: (a) XRD ϕ scan around the (103) YBCO reflections and around the (200) MgO reflections. Two peaks of YBCO are splitted, at $\phi = 90°$ and $\phi = 270°$ (the signal background is only due to backscattering of X-rays). (b) Polar figure ($\phi - \chi$ map) around the (103) YBCO reflections. The breakage of the 90° symmetry is even more clear: the two peaks at $\phi = 90°$ and $\phi = 270°$, which are splitted in ϕ, are also less elongated in χ. The blue circumference is the single ϕ scan shown in panel (a).

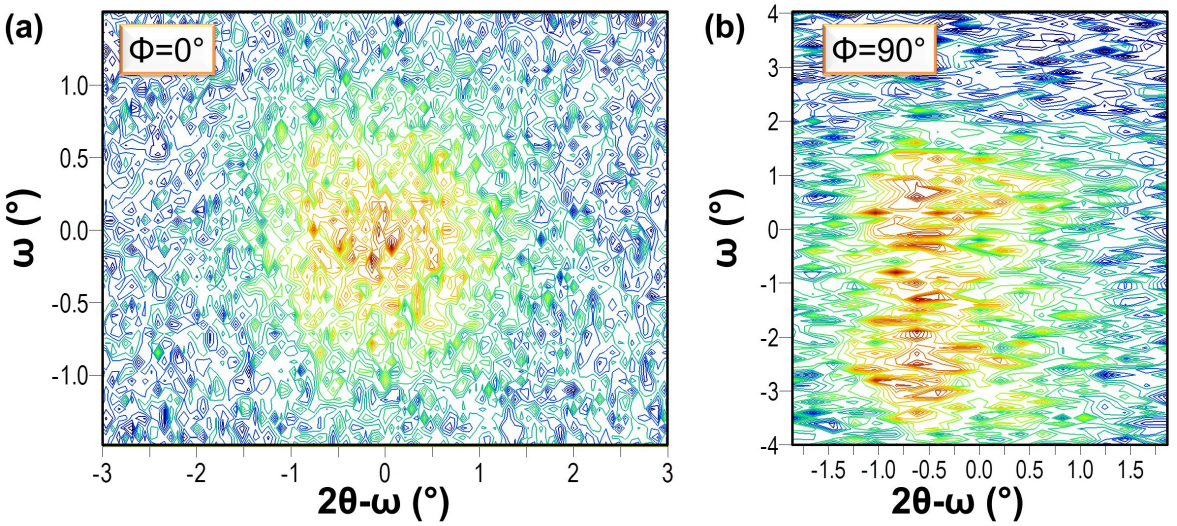

Figure 3.6: XRD $2\theta - \omega$ maps around the (308)/(038) reflections of YBCO fixing (a) $\phi = 0°$, (b) $\phi = 90°$. The center of both the scan in $2\theta = 106.0°$). It is worth noticing that the ω scale in panel (b) is more than double than that of panel (a). Thence the peak at $\phi = 90°$ is much more elongated in ω than that at $\phi = 0°$.

one peak, but in a different position (the maximum is at $2\theta = 105.38°$, see Fig. 3.6b). From the position of the peak at $\phi = 0°$ and $\phi = 90°$, we can identify the (308) reflection as that appearing at $\phi = 0°$, corresponding to $a = 3.85$ Å, and the (038) that appearing at $\phi = 90°$, corresponding to $b = 3.87$ Å. The random exchange of a and b axes is eliminated: for the first time, we have achieved untwinned YBCO films using a substrate without vicinal angle cut but with a strong in-plane anisotropy. With regards to the film-substrate orientation relationship, the (038)/(308) maps (see Fig. 3.6b) show that the b axis is aligned along the direction corresponding to $\phi = 90°$. The ϕ scan (see Fig. 3.5a) shows that along the same direction the (200) reflection of MgO is present. In conclusion, we have deposited untwinned YBCO films on MgO (110) substrates, with the following in-plane epitaxial relations: (100) YBCO//(1,-1,0) MgO and (010) YBCO//(0,0,1) MgO (see Fig. 3.7). The (038)/(308) maps also confirm the

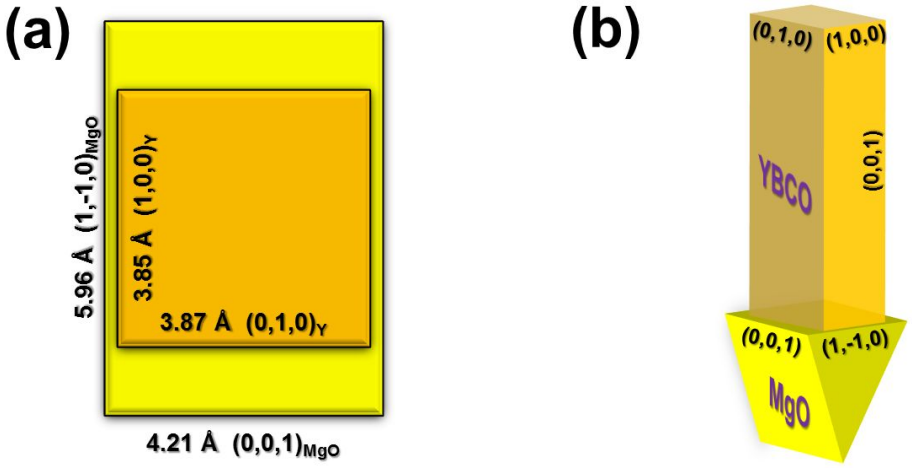

Figure 3.7: Sketches from top (a) and side (b) view of the YBCO/MgO epitaxial relations. YBCO is twinned, with the a axis aligned to the (1,-1,0) axis of MgO and the b axis aligned to the (0, 0, 1) axis of MgO.

very complex in-plane texture of our films. In particular, the elongation along ω of the (038) reflection (see Fig. 3.6b) is compatible with an in-plane waving of the b axis. These features, associated to the strong anisotropic strain induced in the YBCO layer by a substrate with such a large mismatch, have to be further characterized. Analysis with atomic resolution Transmission Electron Microscopy (TEM) and nanodiffraction experiments are current in progress.

3.5 YBCO films on LAO(001)

As a consequence of the very good matching between in-plane lattice parameter of YBCO ($a = 3.82$ Å, $b = 3.89$ Å) and LAO ($a = b = 3.79$ Å), we have been able to deposit 50 nm thick films of YBCO with T_C up to 91 K. To reach such critical temperatures, a very high deposition temperature $T_{dep} = 865°$C is required, at the expenses of the surface properties, strongly degraded.

We have therefore used lower deposition temperatures ($T_{dep} = 810°$C) to achieve smoother surfaces of crucial relevance for nanopatterning. Soon after the deposition

of the films, and before starting the cool down, the films have been heated up to a temperature corresponding to the T_{dep} (865 °C, which optimizes the T_C) for few minutes. This procedure improves the T_C, preserving the surface morphology. In this way we have obtained films with T_C of ≈ 89 K and very sharp transition (0.5-0.8 K).

AFM and SEM images (see Fig. 3.8) show atomically flat sufaces, with a roughness smaller than a single YBCO atomic cell, characterized by growth spirals and squared nanosize particles aligned along the a and b directions.

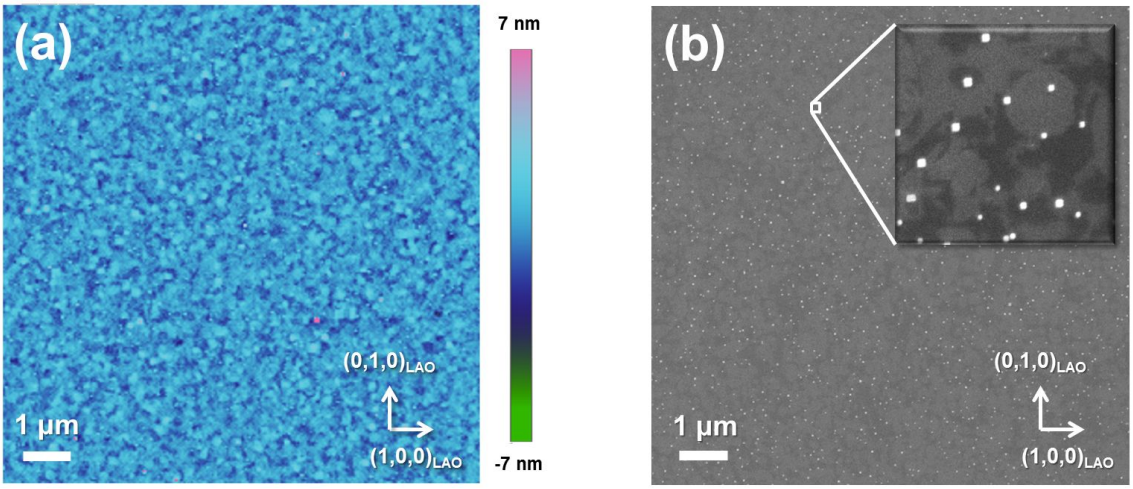

Figure 3.8: (a) AFM image of a YBCO film on LAO (001), showing atomically flat surfaces over large areas (roughness < 1 nm). (b) SEM image of the same film. Both the growth spirals and the squared nanosize particles are highlighted in the inset.

Figure 3.9 shows the XRD symmetric $2\theta-\omega$ scan of a film, with all the $(00n)$ peaks indicating that the film are highly oriented along the c-axis direction. The degree of epitaxy and the structure quality is higher than on films grown on MgO (001), as demonstrated by the narrow rocking curves of the $(00n)$ peaks, having a FWHM of only $\approx 0.3° - 0.5°$. The average c-axis lattice parameter of YBCO, as extracted by all the $(00n)$ Bragg peaks, is 11.71 Å. It is slightly larger than that of bulk YBCO, as it is expected for a non-relaxed film where the in-plane lattice parameters are locked by the biaxial compressive strain of the LAO substrate ($\delta^m < 0$).

The in-plane epitaxy of the films has been examined by using XRD ϕ-scan around the (025) YBCO reflections (see Fig. 3.10a). We have detected four peaks spaced at 90° and aligned with the substrate peaks. The four fold symmetry is an indication of the random exchange of the a and the b axes. The twinning structure is studied by $2\theta-\omega$ mappings around the (038)/(308) YBCO reflections (see Fig. 3.11). Two peaks of similar intensity are found both at $\phi = 0°$ and $\phi = 90°$ (for each value of ϕ, the relative intensity between the two peaks can be changed by slightly varying the tilt of the sample). This implies the existence of (100) and (010) domains, aligned along both the a and the b axes of the substrate. Therefore these films are twinned, as we would expect considering the cubic symmetry of the LAO substrates. From the relative peak intensity area and intensity area ratio it is possible to conclude that the densities of the a and b-axis domains are of the same magnitude. The measured in-plane epitaxial

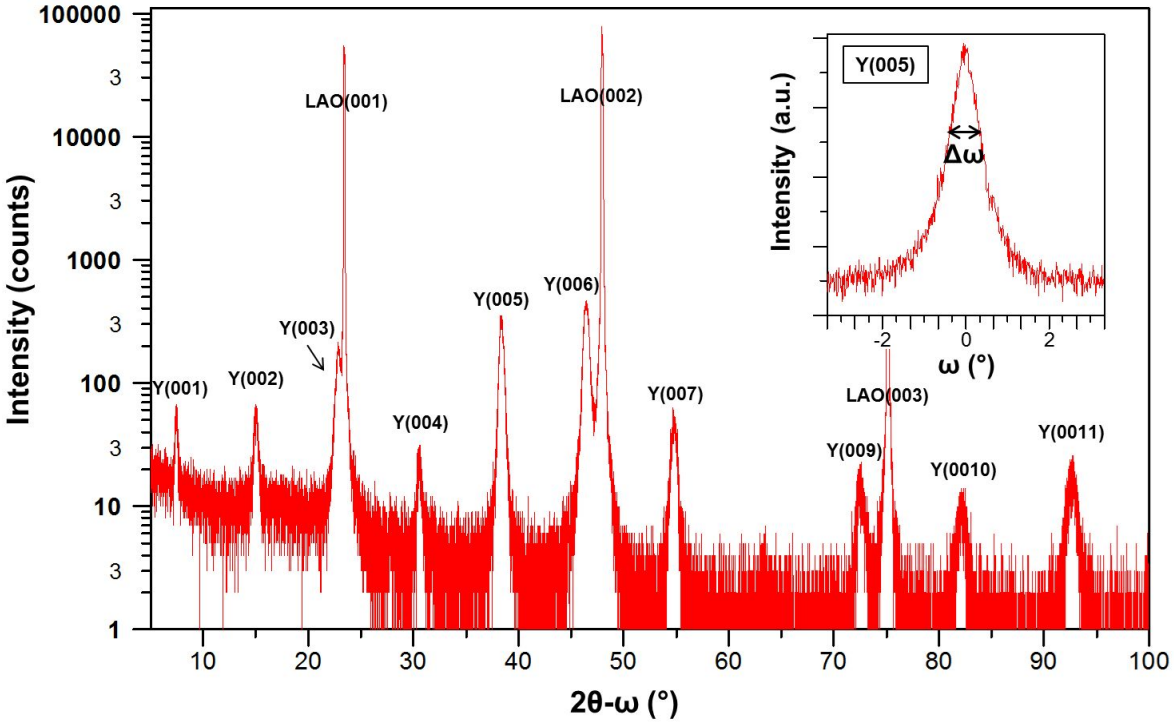

Figure 3.9: XRD $2\theta - \omega$ scan of a 50 nm thick YBCO film on LAO (001). Only the $(00n)$ Bragg peaks of YBCO are present, implying a c-axis growth of the film. In the inset, a rocking curve of the (005) YBCO reflection is shown, with a FWHM of only 0.45°.

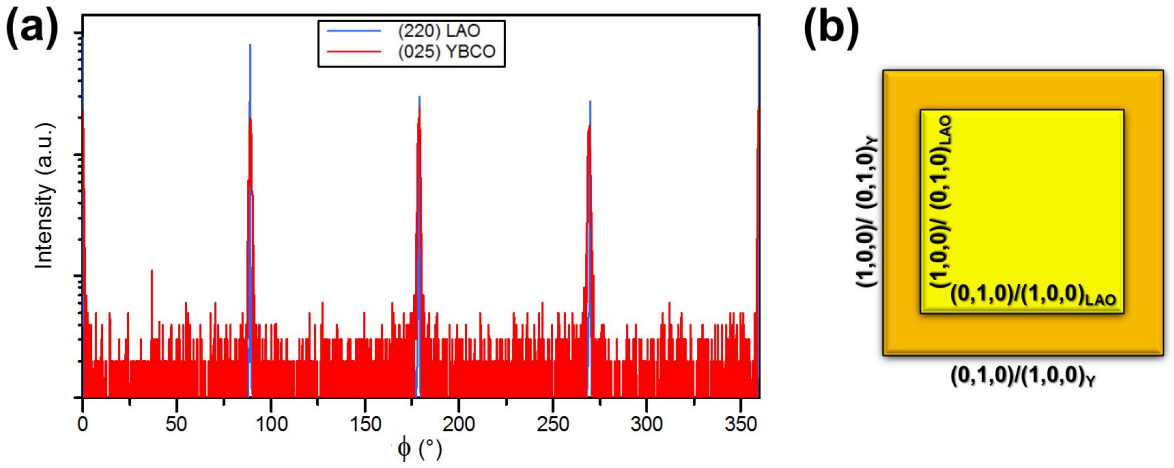

Figure 3.10: (a) XRD ϕ scan around the (025) YBCO reflection and around the (220) LAO reflection. (b) In-plane epitaxial relations of YBCO films grown on LAO (001). The cell of YBCO is aligned with that of the substrate. In addition, YBCO is twinned: a combination of the a and the b axes is present along each in plane lattice parameter of the substrate.

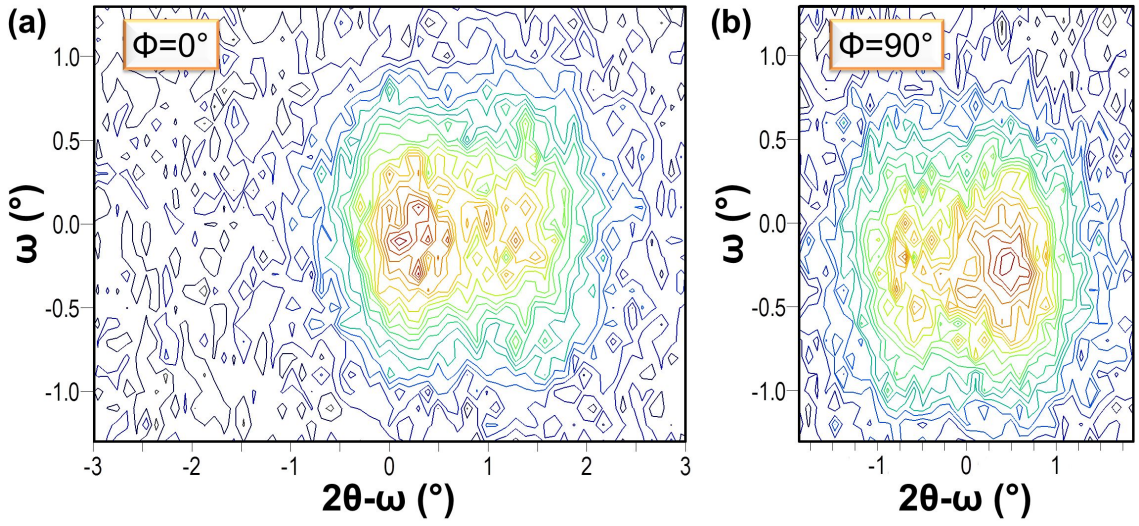

Figure 3.11: XRD $2\theta-\omega$ maps around the (308)/(038) reflections of YBCO (a) fixing $\phi = 0°$ (the center of the scan in 2θ is 105.3°); (b) $\phi = 90°$ (the center of the scan in 2θ is 106.1°). In both the cases the tilt angle χ has been chosen so to get different intensities from the two peaks, highlighting the two distint reflections, which occurr at $2\theta = 105.4°$ and $2\theta = 106.6°$. From the position of these two peaks we can extract the following in-plane parameters: $a = 3.82$ Å, $b = 3.88$ Å, which are rather close to the relaxed values.

relations are schematized in Fig. 3.10b.

3.5.1 Underdoped YBCO films

The YBCO thin films grown on LAO (001) at high deposition temperature (T_{dep} = 865°C), with T_C higher than 91 K, can be considered in the optimally doped regime. By changing the deposition conditions, i.e. decreasing the post-annealing pressure, for example, we may reduce the oxygen diffusing into the film during the cool down and therefore the superconducting critical temperature. In this way, we can explore the underdoped region of the superconducting dome. In literature similar experiments are reported, in which an annealing in a reduced oxygen pressure is done ex-situ to reduce the oxygen content [118]. In our case, we preferred an in-situ annealing to achieve a better degree of homogeneity and reproducible results.

We have deposited different films, decreasing the post-annealing pressure by more than 5 orders of magnitude. $R(T)$ measurements have shown that we have been able to reduce the T_C down to ≈ 60 K (see Fig. 3.12), so exploring a region of the superconducting dome going from the optimally doped plateau down to the 60 K plateau. The homogeneity of the films is confirmed by the width of the superconducting transition that, although increasing at lower T_C, is always smaller than 3 K.

The reduction of oxygen doping is associated to an elongation of the c-axis length [119, 120]. As a consequence, we have observed that the symmetric $(00n)$ Bragg peaks in the XRD $2\theta - \omega$ scans appreciably shift toward lower diffraction angles (see Fig. 3.13a). The extracted c-axis lattice parameters of YBCO are shown as a function of the in-situ post-annealing pressure in Fig. 3.13b. Following Ref. [121] we can derive

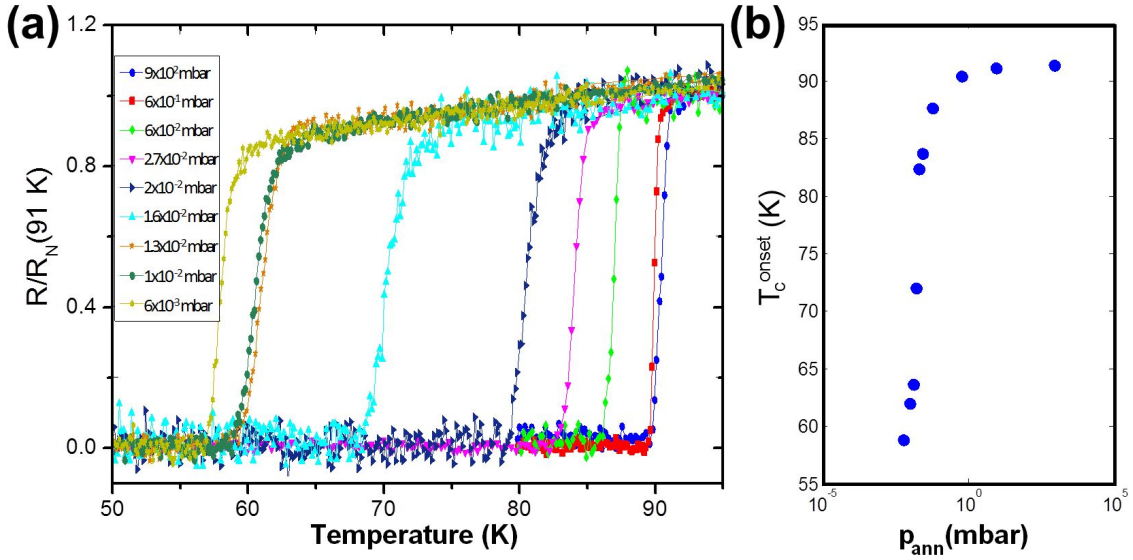

Figure 3.12: (a) Resistance (normalized to its value at 91 K) vs temperaure of the YBCO films deposited at different post-annealing pressures. The onsets of the superconducting transition all these films are plotted in (b), as a function of the post-annealing pressure.

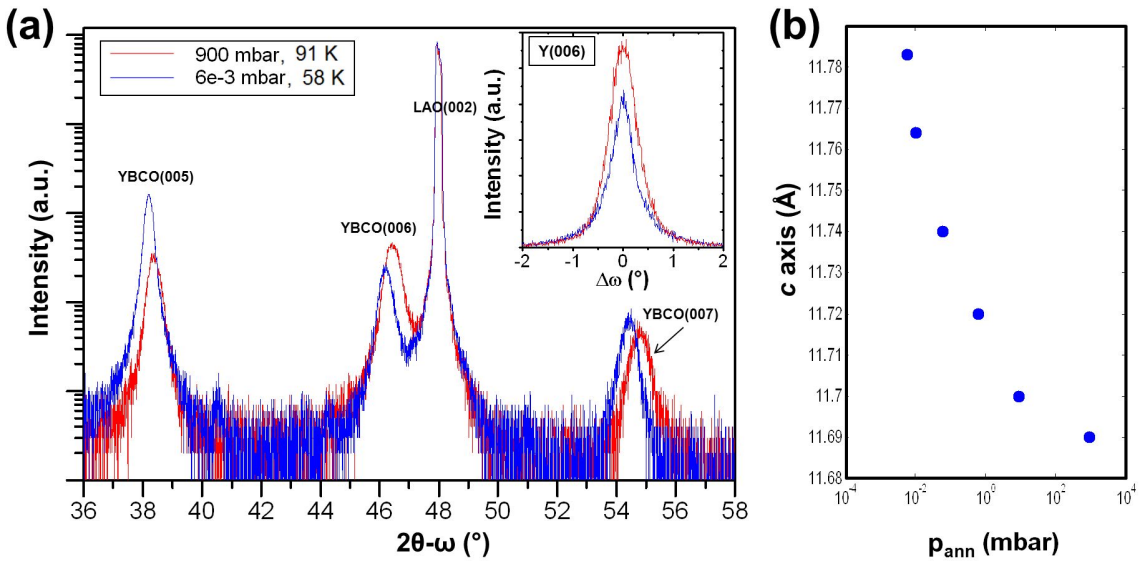

Figure 3.13: (a) XRD $2\theta - \omega$ scans of an optimally doped YBCO film and of an underdoped film, with the lowest critical temperature ($T_C \approx 58$ K). All the $(00n)$ peaks of the underdoped film are shifted toward the left. In the inset, the rocking curves of the (006) peak of these two films are shown, both characterized by a FWHM narrower than 1°. (b) The c-axis lattice parameters of YBCO, extracted from the position of the $(00n)$ Bragg peaks in the XRD $2\theta - \omega$ scans, are shown as a function of the in-situ post-annealing pressure.

for each value of c-axis parameter the value of the oxygen content n (defined in sec. 2.2.2) in the YBCO cell, according to the experimentally determined equation:

$$n = 75.250 - 5.856 \cdot c \, . \tag{3.2}$$

The result is that, decreasing the post-annealing pressure, we have reduced the oxygen content roughly from 6.9 to 6.4. By comparison with the phase diagram in Fig. 2.2, we may conclude that the agreement between c-axis parameters extracted from XRD measurements and T_C values measured from $R(T)$ curves is rather good. As a further proof of the quality of our underdoped films, the FWHM of the rocking curves of the $(00n)$ peaks are narrower than 1° in the whole range of doping (see Fig. 3.13a).

SEM images show that several particles are already present in optimally doped films, since the surface morphology has not been optimized for these films, as previously discussed (see Fig. 3.14a). Decreasing the oxygen doping, the density of these particles increase, and elongated grains, similar to a-axis domains, appear (see Fig. 3.14b). This occurrence limits the usage of these films for the fabrication of nanostructures.

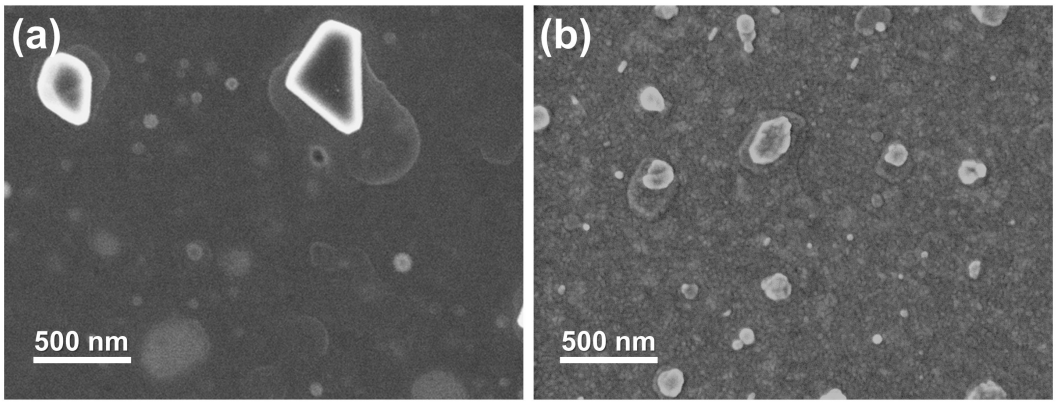

Figure 3.14: SEM images of (a) an optimally doped film, with $T_C = 91$ K; (b) an underdoped film, with $T_C = 58$ K.

3.5.2 YBCO/LSMO bilayers

YBCO films capped with a ferromagnetic $La_{0.7}Sr_{0.3}MnO_3$ (LSMO) layer have been also fabricated. As it will be discussed in the next chapter, gold is generally used as a capping layer, to preserve the properties of YBCO nanostructures during the patterning procedure. However, for optical applications a gold capping cannot be used, because of its high conductivity. At the same time the physics of ferromagnetic/superconducting interfaces has recently received a lot of attention [122]; in the context of photodetectors, in nonequilibrium pump-probe experiments the use of LSMO has demonstrated an important functionality by reducing the electronic relaxation times when compared to bare YBCO films[123].

YBCO films grown on LAO have been preferred because of their atomically flat surfaces, which make them suitable for heterostructures. On top of the YBCO layer a 15 nm thick LSMO film has been deposited ex-situ by PLD, at 0.2 mbar O_2 pressure

and at a temperature of 730°C. Here, the growth conditions have been optimized to get the right compromise between surface smoothness and Curie temperature T_{Curie} of the ferromagnetic LSMO layer. Post-annealing of the bilayers at 800 mbar of O_2 has been employed to promote full oxidation of YBCO through the LSMO capping.

The final YBCO/LSMO bilayer has a surface roughness smaller than 2 nm and a T_C $\sim$ 90 K, with a rather sharp transition with a width below 1 K (see inset of Fig. 3.15). The enhancement of the T_C in the bilayer, with respect to the single YBCO film is

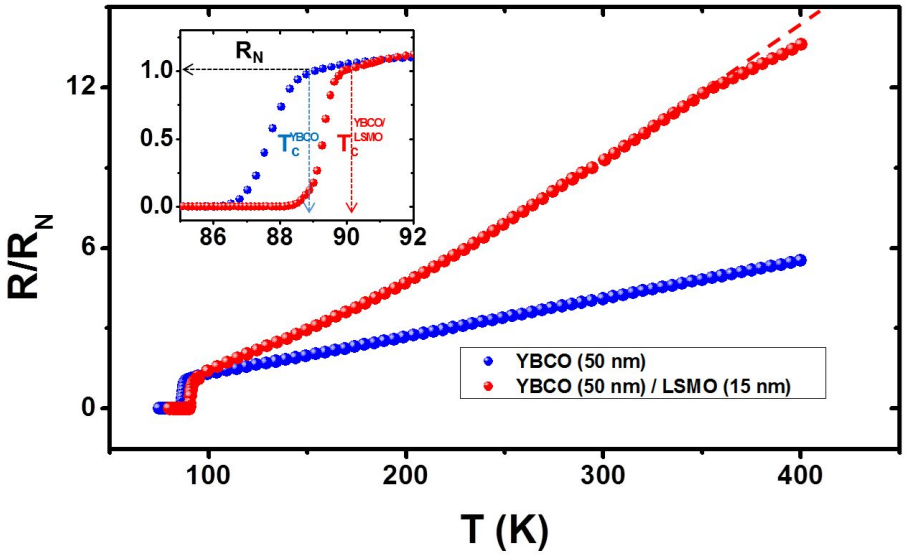

Figure 3.15: Resistance (normalized to the normal resistance R_N) of a 50 nm thick YBCO film before (blue points) and after (red points) the depostion of the 15 nm thick LSMO capping layer. The red dashed line highlights the bending of the R(T) of the bilayer, related to the metal-insulator transition of LSMO, from which T_{Curie} can be obtained. In the inset the T_C enhancement subsequent to the deposition of LSMO is shown.

quite surprising, considering that in literature a diminishing T_C has been reported, and attributed to a suppression of the superconducting properties induced by diffusion of spin-polarized quasiparticles or F/S proximity effect [124, 125]. However, these effects are strongly dependent on the length scales and become dominant if the YBCO layer is very thin ($\sim$ 10 nanometers): in our case instead by assuming only an interface effect between the two layers we possibly have a small variation in the oxygen content of YBCO toward the optimal value [126]. Moreover, by measuring the $R(T)$, we have obtained that the T_{Curie} of LSMO is of $\sim$ 355 K, slightly lower than the optimal value reported for the bulk LSMO (see Fig. 3.15).[1]

TEM investigation has been made on these bilayers, in collaboration with the Institute of Electron Technology of Warsaw. Cross-sectional high resolution images show

[1]One of the most remarkable properties of LSMO is the strong influence of the magnetic transition on the electronic conduction, induced by the *double exchange* interaction: a transition occurs from the high temperature paramagnetic, highly resistive phase to the low temperature ferromagnetic metallic phase. So, at temperatures above T_{Curie} it is a bad conductor and $d\rho/dT < 0$, while below T_{Curie} $d\rho/dT > 0$: the resistance has therefore its maximum around T_{Curie}.

atomically sharp, nearly defect-free interfaces between YBCO and LSMO layer, and a "cube-on-cube" epitaxial relationship (see Fig. 3.16).

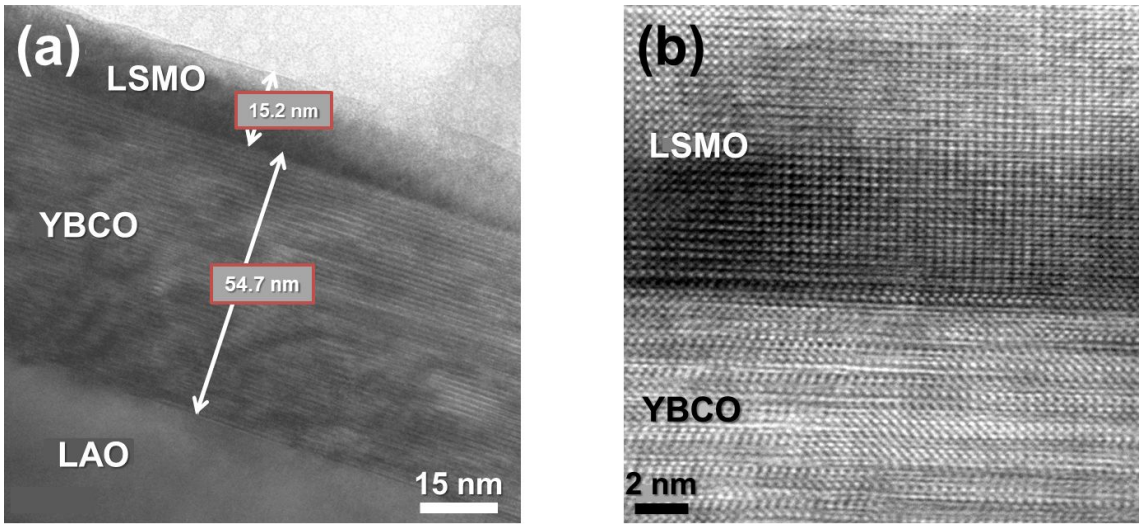

Figure 3.16: Cross-sectional high-resolution TEM images of the YBCO/LSMO bilayers. In (b) the atomically flat and nearly defect-free interface between YBCO and LSMO is highlighted. (Courtesy of the Institute of Electron Technology of Warsaw)

3.6 Summary of the film properties

The main results presented in the previous sections are listed in Table (3.2), together with the results of the transport and morphological characterizations that have been done on YBCO films deposited on (001) oriented MgO and STO (001) substrates.

Parameter	MgO(110)	MgO(001)	LAO(001)	STO(001)
T_C (K)	≈ 85	≈ 86	≈ 89	≈ 88
roughness (nm)	≈ 1.5	≈ 2	≈ 0.8	≈ 0.8
c-axis (Å)	11.71	11.70	11.71	11.65
twinned	no	yes	yes	yes

Table 3.2: Transport and structural properties of the YBCO films whose growth we have optimized.

4

Fabrication of YBCO nanowires

The realization of homogeneous nanostructures preserving pristine superconducting properties represents a challenge for HTS cuprates. The chemical instability of these materials, mostly related to oxygen-out-diffusion, and the extreme sensitivity to defects and disorder due to the very short ξ (of the order of 1 nm), do represent real issues in establishing reliable nanofabrication routines.

For these reasons, different approaches have been followed in the last two decades to achieve YBCO sub micron wires:

- Focused ion beam (FIB) milling and ion implantation have been used to pattern YBCO nanowires in configurations suitable for the detection of magnetic flux [127] and photons [128].

- Arrays of YBCO superconducting nanowires with lengths of several micrometers have been grown in porous alumina acting as morphology-directing hard template [129]. Similarly, porous insulating thin film templates of STO have been deposited between two *c*-axis oriented YBCO thin films and used to achieve *c*-axis YBCO nanowires, with widths smaller than 100 nm [130]. Amorphous STO templates have been also used to fabricate submicron YBCO wires avoiding both chemical and physical etchings [131].

- AFM has been used, in contact mode, as a lithographic tool achieving YBCO nanobridges with widths down to 500 nm [132].

- A special superlattice-nanowire-pattern-transfer technique has been employed to fabricate YBCO nanowires with widths down to 10 nm and lengths of the order of micrometers [133].

- Besides all these different techniques, the patterning of YBCO nanowires is more commonly realized by electron beam lithography and ion beam etching in combination with an hard mask [19, 20, 21, 22, 134, 135]. In particular, the best performances in terms of critical current density, which represents a measure of the highly uniform superconducting properties of these structures, have been recently reported for YBCO nanowires fabricated using this procedure [18].

In this work we have used e-beam lithography, in combination with an amorphous carbon mask and a soft Ar^+ ion etching to achieve nanowires with cross sections as small as 40×50 nm^2 and lengths spanning in a wide range from 100 nm to several microns [136, 137, 138]. A 50 nm Au capping layer is also kept on top of the nanostructures.

4.1 The nanopatterning procedure

In the following, we will show step by step our improved nanopatterning procedure for the realization of YBCO nanowires. The superconducting properties of the patterned nanostructures are strongly affected by the choice of the masking materials and of the parameters for the patterning, in particular the resist baking temperature and the ion milling etching parameters. For more details, we refer to the Appendix A. In what follows we briefly summarize the main steps (see legend in Fig. 4.1):

Figure 4.1: Legend of the colors, which are used in the schematic representations of the nanofabrication steps in the following pages.

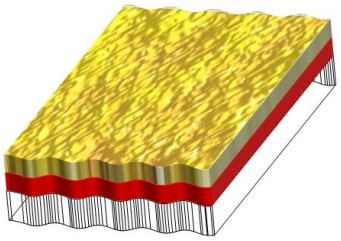

- The YBCO film is covered ex-situ, soon after its deposition, by a 50 nm thick Au film acting as a protective capping layer, so as to prevent any oxygen loss and to avoid any possible contaminations.

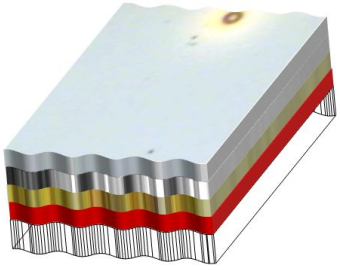

- A carbon (C) layer is used as a mask. The choice of this material is due to its robustness to Ar^+ ion milling (2-3 times harder than YBCO) and to its property to be removed by oxygen plasma (e.g. differently than titanium [135]). After carbon deposition, a double layer resist is spun.

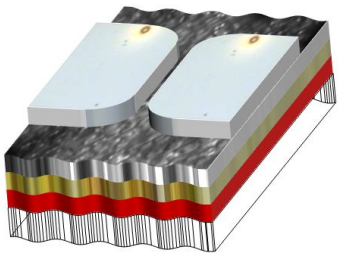

- The nanowire geometry is defined by electron beam lithography at 100 kV. The exposed areas of the resists are than removed during the resist development.

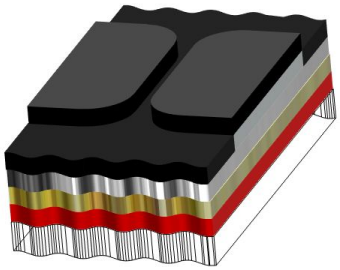

- A thin layer of chromium (Cr), acting as a mask for the carbon, is evaporated on top of the exposed double layer resist.

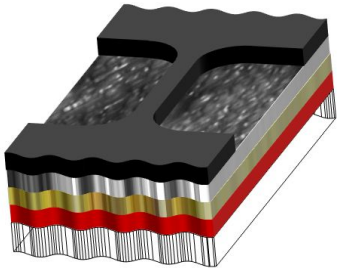

- The mask is defined after the Cr layer is lifted-off.

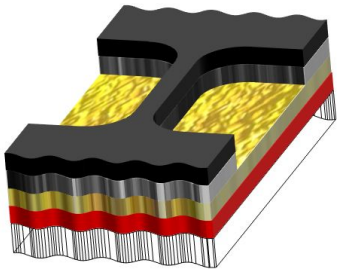

- The carbon layer not covered by chromium is removed by low power oxygen plasma etching.

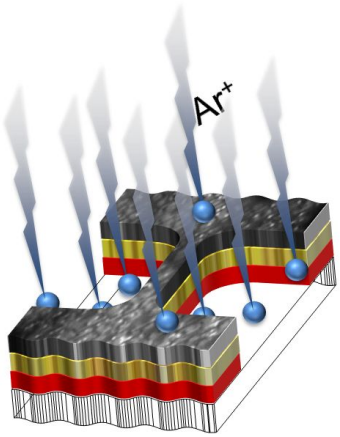

- The Cr layer, the Au and YBCO which are not covered by C, are etched by Ar^+ ion-beam milling. The etching parameters (beam voltage and current, time) have been carefully calibrated in order to minimize the interaction of the ions with the nanostructures. In particular, we have chosen to work close to the etching voltage threshold for YBCO. The overheating of the YBCO has been also reduced by means of the presence of the Au capping.

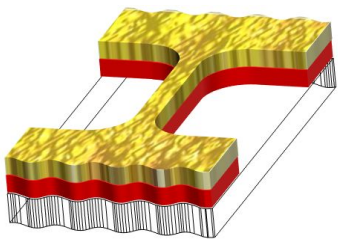

- The C layer is removed by plasma etching, while the Au capping is kept, so to avoid any interaction between the Ar^+ ions and the surface of the YBCO wires.

Pristine structures and reproducible results at the nanoscale are intimately related to a good control of the etching process. For this reason, we have engineered an extremely gentle and slow ion milling procedure. Indeed, the interaction of Ar^+ ions with YBCO can strongly affect the transport properties because of severe changes in film stoichiometry and disorder. As it will be clarified in Chapter 5, big differences can be observed in the transport properties, in particular the value of the critical current density and its temperature dependence, by tiny changes of the etching parameters. Moreover, to prevent any redeposition of etched YBCO in the vicinity of the final nanowires, which may cause unwanted parallel shorts along the lateral sides, we overetch 50 nm into the substrate[1].

As regards the Au capping layer, it protects YBCO during all the nanopatterning steps, it favors the thermalization inside YBCO during the ion etching and it minimizes the interaction of the milling species with the YBCO nanostructures. Its thickness is also a crucial parameter. By doing a systematic characterization of the nanowires as a function of the Au thickness, we have noticed that the superconducting properties of the wires (i.e. the current densities, see Chapter 5) strongly degrade by reducing the Au thickness to 30 nm. On the other side, a thicker Au coverage, of the order of 100 nm, limits the minimum achievable lateral size of the nanowires to 80-100 nm, because of the erosion of the C mask caused by longer etching times.

4.2 YBCO nanowires

Following the procedure described in sec. (4.1), we have achieved YBCO nanowires with widths down to 40 nm and lengths from 200 nm to several microns (see Fig. 4.2).

A combination of AFM and SEM has been used for the determination of the cross sections of the nanostructures. The YBCO bridge thickness is known from our calibration of the PLD deposition rate for YBCO films. From the AFM images we obtain the total thickness of the patterned structure, which is typically 150 nm. It consists (from top to bottom) of 50 nm Au, 50 nm YBCO and 50 nm substrate (see Fig. 4.3a). Moreover, from AFM we can extract the minimum angle between the substrate surface and nanobridge sidewalls ($\approx 75°$), which is only limited by the shape of the AFM tip. The SEM images give instead a very good "direct" measure of the width of the bridge on the top (w_{min}, interface of gold capping layer with vacuum) and bottom (w_{max}, interface of YBCO film with substrate) (see Fig. 4.3b). The determinations of the width of the bridge side walls using SEM, given by $w_{sw} = (w_{max} - w_{min})/2$, is very similar to the one extracted from AFM and they do indeed coincide within few nanometers. Therefore the absolute error of the bridge width w determination is less than 5 nm.

[1]The unavoidable redeposited substrate material should not have any influence on the superconducting properties.

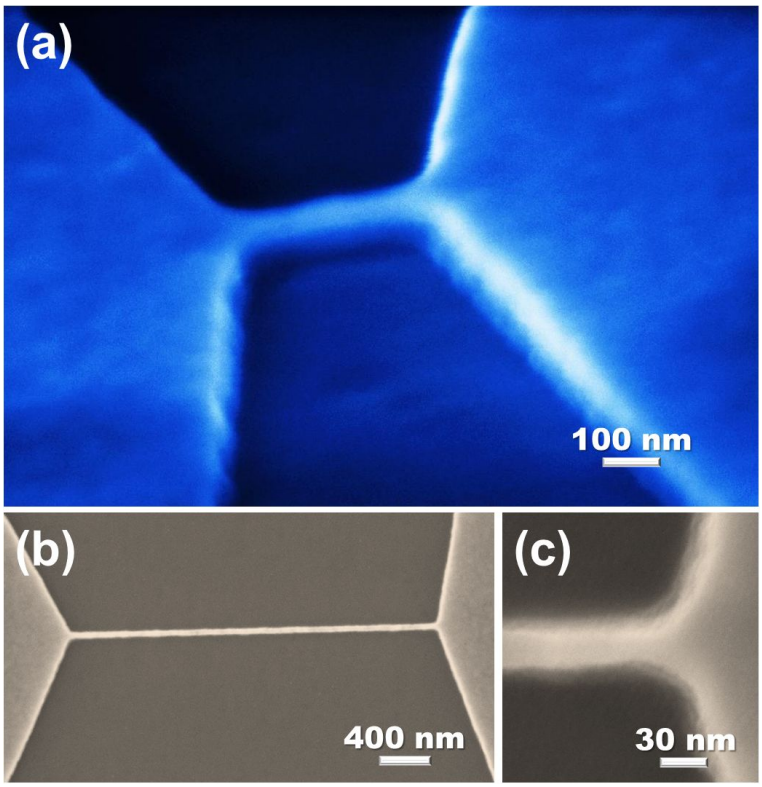

Figure 4.2: (a) Tilted angle SEM image of a 40 nm wide and 200 nm long YBCO nanowire. (b) SEM image of a 40 nm wide and 3 μm long YBCO nanowire, whose enlargement, confirming the uniformity of the nanostructure, is shown in panel (c).

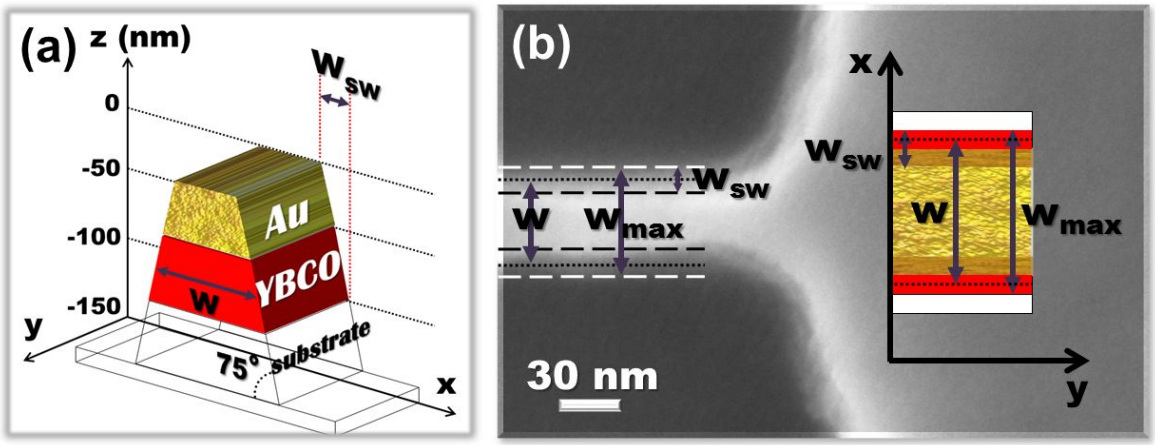

Figure 4.3: (a) Schematics of a typical AFM line scan along the cross section of a nanobridge. (b) a SEM picture of a nanowire is combined to the schematics of the top view of the AFM cross section, showing the wire from the SEM perspective. The w can be calculated as $w = w_{max} - w_{sw}$.

5

Transport characterization of YBCO nanowires

As already pointed out in Chapter 4, HTS nanostructures may undergo a strong degradation during the patterning. As a consequence, their superconducting properties are seriously affected. To assess the homogeneity of these structures, a valuable test is the measurement of the critical current density J_C (defined as the ratio between the measured critical current and the wire cross section), which is very sensitive to any local non-uniformity and damage inside the wire [139].

Theoretically, an infinite long wire with width smaller than the Pearl length $\lambda_P = \lambda_L^2/t$ (which is ≈ 800 nm in case of a 50 nm thick wire) and much larger than ξ (which is the case for YBCO nanowires) is characterized by a uniform current distribution, with a J_C value, only limited by entry of Abrikosov vortices. Indeed, as already stated in sec. (2.3.3), when ramping up the bias current applied to a bridge, the critical supercurrent is reached once the local current density at the edges of the bridge equals a value close to the depairing current density [95]. At this point vortices can enter the bridge, causing a transition from the zero voltage state to the finite voltage state. The expression for the depairing limit is equal to $J_d = \Phi_0/(3\sqrt{3}\pi\mu_0\lambda_L^2\xi)$ according to the Ginzburg-Landau theory, and its value for YBCO at 4.2 K is equal to $\approx 1.3 \times 10^8$ A/cm^2 (with $\xi = 1.5$ nm and $\lambda_L = 230$ nm).

The J_C values of HTS nanowires available in literature present a huge spread of values, together with an unexpected reduction by reducing the width, which has been mainly attributed to damages occurring during the patterning (see Fig. 5.1). In Ref. [22] the authors find a steady reduction of the J_C from $w \approx 1$ μm till 200 nm with values never exceeding 10^7 A/cm^2 at 4.2 K. An almost constant J_C for nanowires in the range 50 nm $< w <$ 150 nm has been obtained in Ref. [20]. However in this case the maximum achieved J_C is of the order of 2×10^7 A/cm^2. Xu et al. [133], with their parallel arrays of hundreds of YBCO nanowires, have reached the ultimate lateral size, at the expenses of the superconductivity, which is strongly affected by the nanopatterning procedure, with average J_C for a single 15 nm wide wire as low as 10^5 A/cm^2 and a transition temperature below 20 K. In the attempt to improve the superconducting properties of YBCO nanowires, Papari et al. [18] have made preliminary studies of the role of a protecting layer of Au. They have obtained substantial improvement in the performances for nanowires widths ≈ 150 nm with J_C as high as 7×10^7 A/cm^2.

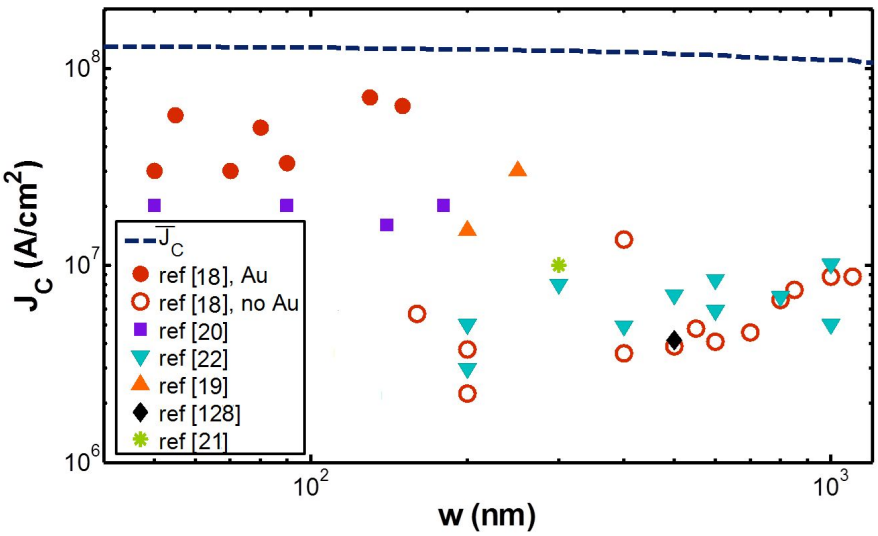

Figure 5.1: Critical current density J_C measured at 4.2 K as a function of the width w for different YBCO nanowires, available in literature (adapted from [18]). The dashed line represents the numerically calculated critical current density $\bar{J}_C$ for an infinite long (type II) wire, with thickness $t < \lambda_P$, as a function of the width w. If $w < \lambda_P$, which is $\approx$ 800 nm for $t = 50$ nm, such a value saturates to the depairing limit.

However for narrower wires they still observe a decreasing J_C by reducing the wire's width with values not exceeding 3×10^7 A/cm^2 for 50 nm wide wires. More importantly in their work the narrower nanowires showed a transition temperature several degrees lower compared to the larger one. This indicates significant damages at the smallest nanowire widths, possibly due to a too thin Au protecting layer of only 20 nm and to a non-optimal Ar^+ ion etching parameters for very narrow wires.

In this chapter we will show the transport characterization of our YBCO nanowires. As a consequence of the soft ion milling procedure we have performed and of the presence of the Au capping layer on top, our nanostructures demonstrate that the superconducting properties, close to the as grown films, are preserved. Thence, they represent model systems, which may open new directions in engineering novel HTS devices at the nanoscale for both fundamental and applied purposes. In particular, the wide range of lengths we have been able to achieve allows their integration in magnetometers for the shortest wires and in devices for photodetection experiments for the longest ones.

5.1 Current-voltage characteristics

The electrical transport properties of the nanowires have been measured in a ^{3}He cryostat (for more details, see Appendix B) using a four point probe configuration. Fig. 5.2a shows a current-voltage characteristic (IVC): it is flux-flow like at high bias voltages, with the presence of a small switch from the zero voltage state to a finite voltage state at I_C (see inset of Fig. 5.2a). Differently from LTS materials, the high value of the thermal conductivity in YBCO (≈ 2 Wm^{-1}K^{-1}) [140] prevents self-heating

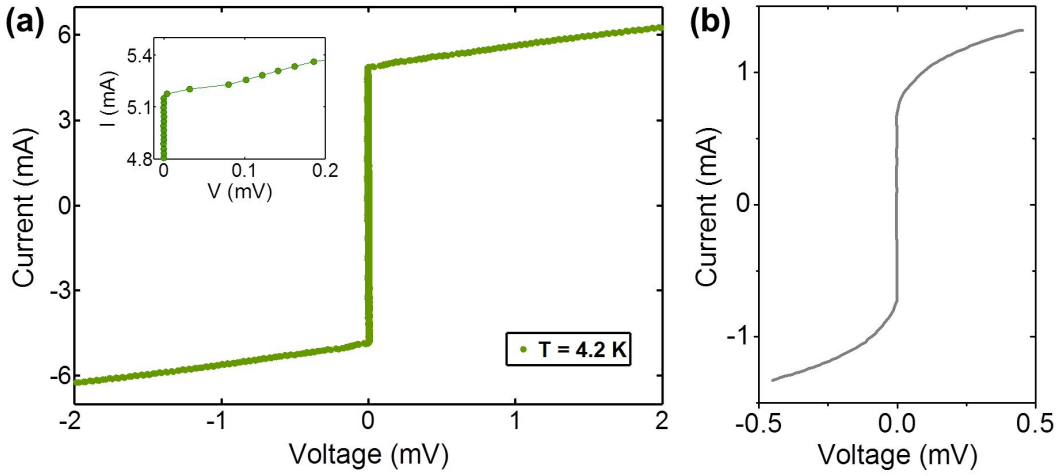

Figure 5.2: (a) IVC measured at 4.2 K for a 90 nm wide and 200 nm long YBCO nanowire. In the inset, the small voltage step driving the superconducting channel to the resistive state is highlighted. This step represents the most significative deviation of our IVC from typical flux-flow behavior (shown in (b) for comparison. Adapted from [28]).

effects, which could bring the whole device to the normal state just above the critical current.

Similarly to the J_C values, also the IVCs of YBCO nanowires, available in literature, present a large spread of behaviors. Several authors have reported the presence of very large voltage switches/steps ($\Delta V = 50 - 150$ mV) above I_C in the IVC of YBCO nanowires, at high bias voltages [18, 141]. These switches, which are accompanied by a large hysteresis (exceeding 30% of the total current) have been explained in terms of the appearance of phase slip centers and hot spots, triggering the nanostructures from the superconducting to the resistive and normal state. In Ref. [142] flux-flow like IVCs have been reported, characterized by a series of small voltage steps ($\Delta V \leq 1$ mV) in the resistive branch. These voltage steps have been attributed to an incoherent motion of vortices across the nanowire at currents above I_C. None of these mentioned features is present in our case. The origin of the small voltage switch we measure above I_C is still under investigation.

5.1.1 Critical current density vs wire width

Once the cross sections A_w have been accurately determined with SEM and AFM, we have extracted from the IVC the critical current density $J_C = I_C/A_w$ of more than 200 nanowires, varying in width from 40 nm to 2 μm and length from 100 nm to 3 μm.

In Fig. 5.3a (red circles), the J_C at 4.2 K of our YBCO nanowires with a fixed length of 200 nm and belonging to the same chip, are reported as a function of the width. We have observed two important features:

- The decrease of J_C with decreasing wire width w, observed several times in literature (see Fig. 5.1), is not present in our case.

- The narrowest wires have a J_C larger than 10^8 A/cm^2, approaching the Ginzburg-

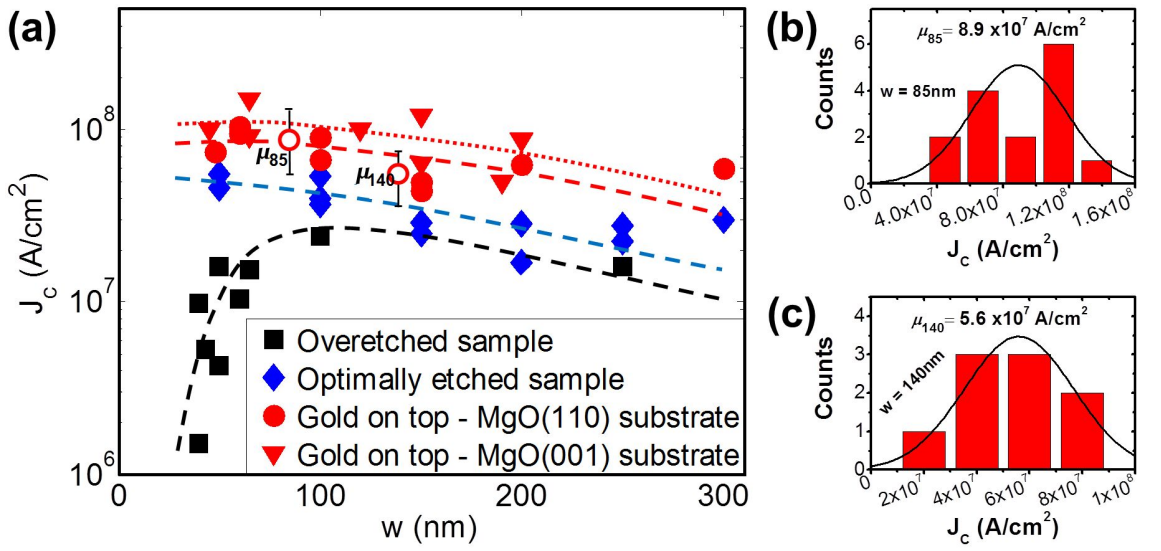

Figure 5.3: Critical current density J_C measured at 4.2 K as a function of the width w for 200 nm long YBCO wires with and without a Au capping layer. The dashed lines are guides for the eyes. The two open circles represent the mean values of the two sets of nanowires with fixed width $w = 85$ nm (panel b) and $w = 140$ nm (panel c).

Landau depairing limit. Such a value is about $1 - 3 \times 10^8$ A/cm^2, (eq. (2.28)[1], for (001) YBCO films with T_C of 85 K, characterized at low temperature by a coherence length and a London penetration depth given respectively by $\xi_0 = 1.4 - 2$ nm and $\lambda_0 = 150 - 250$ nm [18, 144]).

To strengthen these findings, we have added in Fig. 5.3a the results of two more chips, fabricated with the same nanopatterning procedure. The first one was prepared with the idea to acquire large statistics of the distribution of the J_C values for a specific width and it includes only nanowires with fixed width of 85 nm and 140 nm. The J_C distributions for the two widths are reported Figs. 5.3b and 5.3c: the two mean values μ_{85} and μ_{140}, shown as open circles in Fig. 5.3a together with the standard deviations, agree extremely well with the expected J_C for those widths. The second chip is made by nanowires fabricated on a commercial (001) YBCO film grown on a (001) MgO substrate, provided by Theva GmbH [145], characterized by a slightly higher T_C of ≈ 1 K compared with our YBCO films on MgO (110) and comparable structural and morphological properties. The J_C values measured on these wires as a function of their width are reported in Fig. 5.3a as red triangles: also in this case we have the same $J_C(w)$ behavior already observed for YBCO grown on MgO (110), with values even a little higher.

Moreover, in Fig. 5.4 the critical current densities measured at 4.2 K for 100 nm wide bridges, all belonging to the same chip, are shown as a function of the bridge length. The independence on length of the critical current density values rules out any

[1]Here it is important to note that this equation is strictly valid only at temperatures close to the critical one. However, calculations for the depairing critical current density in the clean and dirty limit at $T = 0$ K predict a deviation from the GL limit by a maximum factor of 1.5 [143].

kind of artifact in the determination of our very high values of J_C, due to redeposition of YBCO in the vicinity of the wires or to a non-correct estimate of the widths of the narrowest wires.

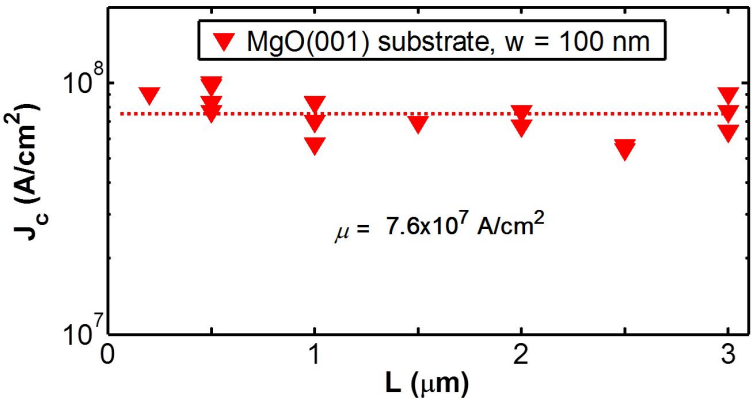

Figure 5.4: Critical current density J_C measured at 4.2 K as a function of the length l for 100 nm wide YBCO wires. The dashed line is the mean value of the J_C distribution for these nanowires.

We have fabricated a sample in which the Au layer has been completely removed from the top of the wires. To minimize the damages on the superconducting nanostructures, the gold has been "optimally etched" with the help of an end point detector installed in our milling system together with a careful inspection of the sample under optical microscope and AFM every 1-2 minutes for the latest part of the Au etching. The resulting J_C, represented as blue diamonds in Fig. 5.3a, does not decrease with decreasing width, differently to what previously reported in literature. On the contrary, the J_C exhibits the same behavior as a function of the width we already observed for Au capped nanowires, although with a little lower values.

To further prove that the reduced Ar^+ ion bombardment of YBCO nanostructures was the turning point in our research, we have fabricated different samples slightly overetching the YBCO nanowires. The black squares in Fig. 5.3a, which all refer to the same sample, show that the J_C decreases with decreasing the nanowire width below 100 nm, in agreement with what has been published in literature during the past years.

All these results prove that we have engineered pristine YBCO nanowires, preserving the properties of the as-grown films. By means of the soft etching procedure and keeping the gold on top, i.e. minimizing the interaction of the Ar^+ ions with the nanowires, we may conclude that the damage of the sides is so minimal that it does affect neither the global nor the local superconductive properties of the nanowires.

5.1.2 Current crowding

The $J_C(w)$ behavior of our Au capped nanowires is different from what previously reported in literature (see Fig. 5.1), but still different from the theoretical prediction of the J_C of an infinite long wire, which should be constant and equal to the GL depairing value for cross sections smaller than λ_P. On the contrary, in our case (see Fig. 5.3) a monotonic increase of J_C can be clearly observed when decreasing the wire width w below λ_P (≈ 500 nm), with the depairing limit reached only by the narrowest

wires ($w \lesssim 60$ nm). However, it has been recently predicted [146] and experimentally confirmed [147, 148] that the critical current of a superconducting nanowire is reduced with respect to the depairing limit even for widths smaller than the Pearl length, if the influence of the wide electrodes connecting the nanowire to the bias circuitry is taken into account. This effect has been associated to the current crowding at the corners between the wire and the electrodes, leading to an enhancement of the local current density at the corners with respect to its average value at the center of the wire. As a consequence, the average critical current density of the wire $\bar{J}_C$ is smaller than the depairing limit even for $w < \lambda_P$.

To assess the role of the current crowding in the experimentally determined $J_C(w)$, we have numerically calculated the current distribution in our structures, with and without taking into account the influence of the on-chip wide electrodes connecting the wire to the bias circuitry. Since the thickness of our wires ($t = 50$ nm) is smaller than the expected in plane London penetration depth ($\lambda_L^{ab} = 150 - 300$ nm), we have limited our studies to the thin film case ($t < \lambda_L$), in which a homogeneous current distribution throughout the whole film thickness can be assumed. Moreover, we have assumed the case of a zero externally applied magnetic field. Finally, if $\xi \ll \lambda_L$, the in plane current distribution $\vec{j}(x, y)$ in the wire, to which the value of the critical supercurrent is strictly related, is given by the Maxwell and London equations [149]:

$$\mu_0 \vec{\nabla} \times (\lambda_L^2 \cdot \vec{j}) + \vec{B} = 0\,; \quad \vec{\nabla} \times \vec{B} = \mu_0 \vec{j}\,, \tag{5.1}$$

where λ_L in this case represents the London penetration depth squared tensor, and $\vec{B}$ is the magnetic field generated by the transport currents.

In the case of an infinite long wire, we found that for widths smaller than λ_P the current distributes homogeneously across the width. As a consequence, the average critical current density $\bar{J}_C$ corresponds approximately to the one-dimensional GL depairing current density: $\bar{J}_C \approx J_d$ [96].

In Fig. (5.5) we show instead the local current density, calculated by solving numerically the eq. (5.1), when considering wide electrodes connected to a wire with width $w = 0.2\lambda_P$. Here, the local current density at the inner corners is enhanced compared to the average current density at the center of the wire, $\bar{J}|_{y=0} = \int j_y(x, y = 0)dx\,/w$. Thence, when ramping up the bias current injected into the wire, the critical supercurrent is reached once the local current density at the inner corners between the wire and the electrodes equals a value close to J_d. The average critical current density can be computed from the numerically determined current distributions in the following way:

$$\bar{J}_C(w) = J_s \cdot \bar{J}|_{y=0}/j_{max}\,, \tag{5.2}$$

where J_s is approximately the depairing value, and j_{max} is the maximum value of the current density located at the inner corners.

The reduction of the average critical current density in a wire with width smaller than λ_P, with respect to the infinite long wire limit, is strongly dependent on the ratio between the inner corner bending radius and wire width. From SEM images (see Fig. 5.6a), we see that typical bending radii we obtain after the nanopatterning procedure for nominally 80° corners are in a range between 10 nm and 40 nm.

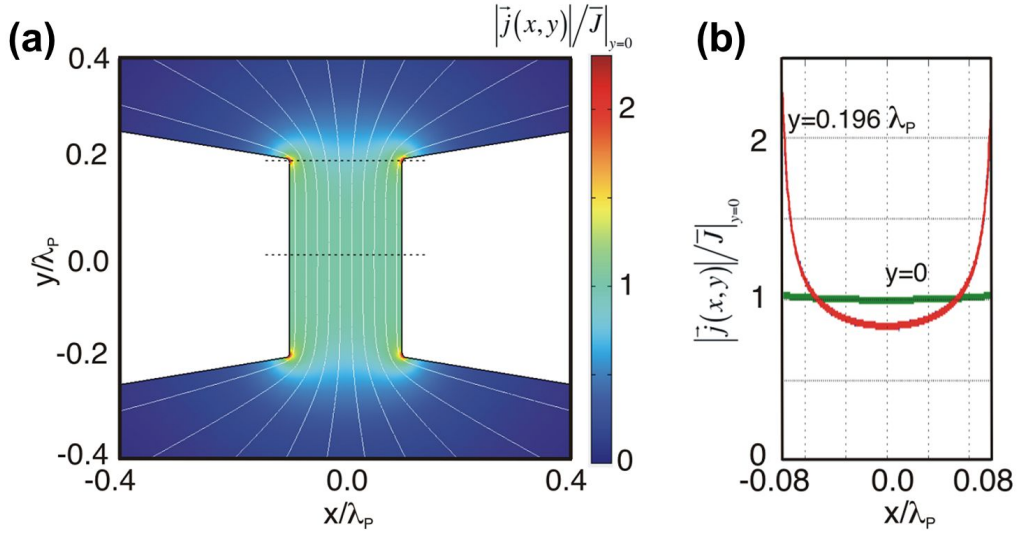

Figure 5.5: (a) Calculated absolute value of the local current density normalized to the average current density at $y = 0$. The white lines indicate the path of the current flow. (b) Line cuts of the current density at $y = 0$ and $y = 0.196\lambda_P$, indicated as dashed lines in (a), highlight the enhancement of the current at the inner corners between the wire and the electrode.

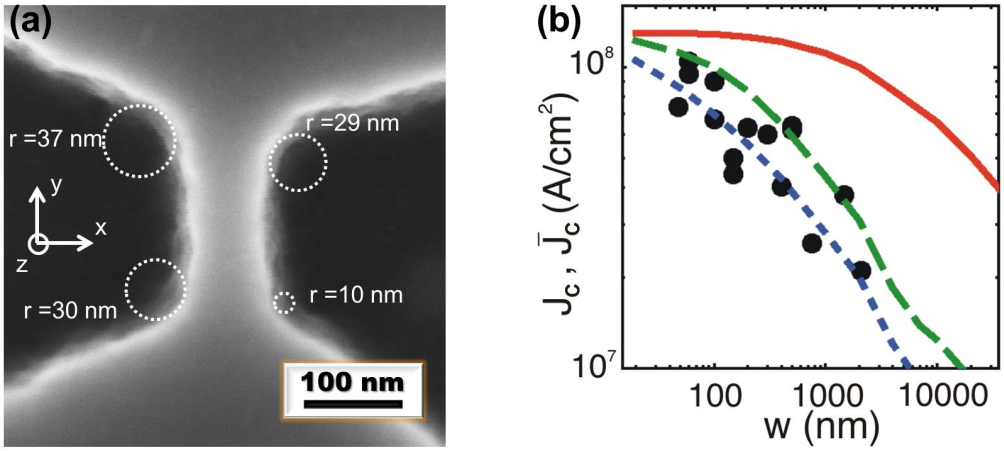

Figure 5.6: (a) SEM image of a 200 nm long and 85 nm wide YBCO wire, capped with Au. The dotted circles indicate the bending radii of the inner corners. (b) The symbols represent the critical current densities J_C measured at 4.2 K as a function of the wire width. The solid line is the numerically calculated $\bar{J}_C(w)$ for an infinite long wire. The dashed and dotted lines are the numerically calculated $\bar{J}_C(w)$, using eq. (5.2), for 200 nm long wires connected to wide electrodes with inner corner radii $r_1 = 40$ nm and $r_2 = 10$ nm, respectively.

Therefore we have numerically calculated, using eq. (5.2), the average critical current density $\bar{J}_C$ of wires of different widths, with bending radii $r_1 = 40$ nm and $r_2 = 10$ nm, and using fixed values for the Pearl length $\lambda_P = 800$ nm and $J_s = 1.3 \cdot 10^8$ A/cm^2 (see Fig. 5.6b). The agreement between the experimentally determined $J_C(w)$ and the current crowding model is very good. It is worth noticing that the critical current density of a nanobridge connected to wide electrodes approaches the depairing value only for a width smaller than half the bending radii of the inner corners.

5.1.3 Critical current density vs temperature

To further demonstrate the excellent quality of the nanowires, in terms of uniformity of the transport properties, we have measured the critical current density as a function of the temperature up to the critical temperature T_C.

The result is that the data of nanowires (even the narrowest ones) with a Au capping layer can be very well fitted (see Fig. 5.7a) by the Bardeen expression [143], valid in the dirty limit[2] ($\ell < \xi$) and commonly used to describe LTS nanowires [151, 152]:

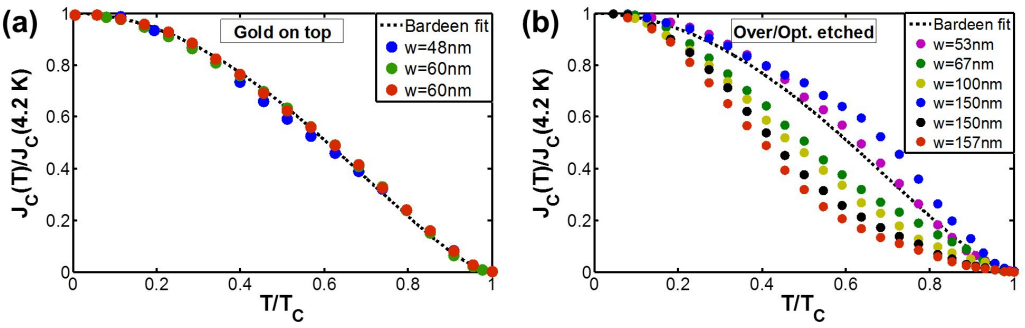

Figure 5.7: Normalized critical current density $J_C(T)/J_C(4.2\text{ K})$ measured in the whole range of temperature for nanowires capped with gold (panel (a)) and for those whose Au capping layer has been removed (panel (b)).

$$J_C(T) \propto \left[1 - \left(\frac{T}{T_C}\right)^2\right]^{\frac{3}{2}} . \tag{5.3}$$

On the contrary, deviations from the Bardeen expression are observed for wires whose Au capping layer has been etched (see Fig. 5.7b). Only few nanowires, probably less affected by damages induced by the nanopatterning, have a $J_C(T)$ following the Bardeen expression in the full temperature range.

5.2 IVC under microwaves

As a further test of the quality of our capped nanowires, we have studied the ac Josephson-like effect in these structures. The appearance of current steps has been

[2]The equivalent expression, derived for the clean limit ($\ell > \xi$) [150], should be more correct in our case. However, the agreement of our data with such expression is rather poor.

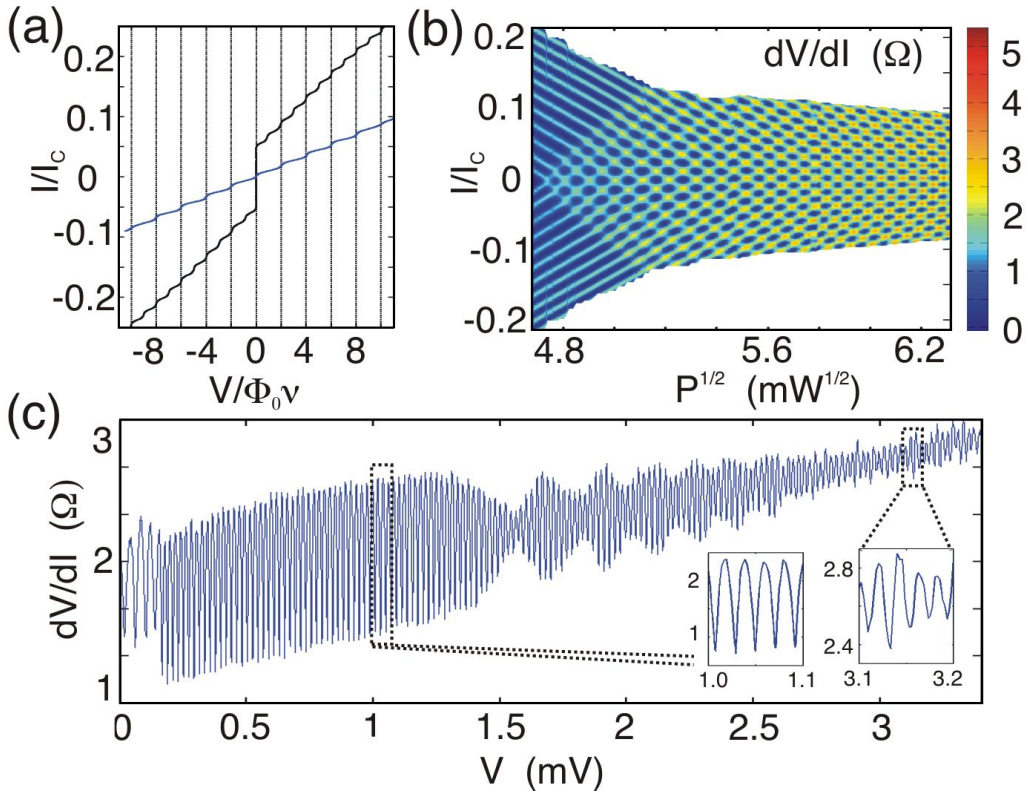

Figure 5.8: The IVC of a 50 nm wide nanowire is measured at 4.2 K, under microwave irradiation (ν = 10.13 GHz) and Shapiro-like current steps are observed. (a) IVC at two different powers at the output of the microwave source, P = 13 dBm (black curve) and P = 16 dBm (blue curve). (b) Differential resistance map as a function of the bias and of the applied microwave power. The blue regions represents the current steps. (c) Differential resistance as a function of voltage at a fixed microwave power of 14.5 dBm. The Shapiro-like steps are highlighted in the insets.

predicted in the IVCs of nanowires with dimensions smaller than λ_P, exposed to a microwave field [16]. These steps, appearing at specific voltages V_n given by the Josephson voltage-frequency relation, $V_n = n\Phi_0\nu$, with n integer and ν frequency of the applied microwave, have been explained in terms of synchronization of the coherent motion of Abrikosov vortices to the external microwave radiation by phase locking. Thence, they are similar to Shapiro steps, which can be observed in the IVCs of Josephson tunnel junctions when the frequency of an external microwave field phase locks with the Josephson oscillations at finite voltages [153].

The IVCs under microwave radiation of one of our narrowest nanowire, with cross section of 50 × 50 nm^2, is reported in Fig. 5.8a for two different applied microwave powers. Shapiro-like steps, occurring at integer multiples of $\Phi_0\nu$, are clearly visible. A differential resistance map of this nanowire as a function of the bias current and of the applied microwave power is shown in Fig. 5.8b. The periodic modulations of the current steps with the external microwave power is strictly connected to the existence of an effective periodic current phase relation in our nanowires [154]. The excellent quality of these structures is confirmed by the observation of up to 160 Shapiro-like steps (see Fig. 5.8c), since any inhomogeneity would prevent the coherent motion of

Abrikosov vortices. Moreover, these steps have been observed up to voltages of ≈ 3 mV, which correspond to a Josephson oscillation frequency of 1.5 THz: such evidence opens new perspectives for the employment of these wires as THz detectors and THz sources.

5.3 Resistance vs temperature measurements

We have measured the resistance of the YBCO nanowires with various lengths and widths as a function of the temperature, in a temperature range around T_C (see Fig. 5.9). The current and voltage probes of our 4-point measurement setup are situated at the far ends of the two wide and long electrodes, with widths $w > 10^4$ nm and $l > 10^5$ nm, connected to the nanowires. Therefore the first transitions at higher temperatures are related to the electrodes and the second broader transitions are instead related to the nanowires. Differently from what previously reported in literature [18], the onset

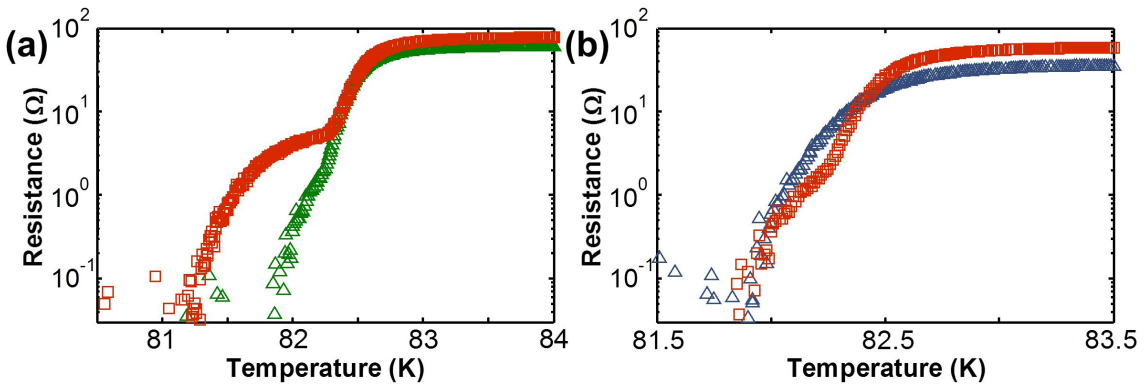

Figure 5.9: $R(T)$ measurements of Au capped YBCO nanowires with different lengths and widths grown on MgO (110). (a) $R(T)$ measurements of a 50 nm (squares) and 150 nm (triangles) wide wires. The length of both these wires is 200 nm. (b) $R(T)$ measurements of a 200 nm (squares) and 1000 nm (triangles) long wires, whose width is 150 nm in both the cases.

temperature of the wire transition is typically only 1 K (or less) below the one of the wide electrodes, even for the narrowest wires.

It is important to note that the measured onset temperature of the wide electrodes, and consequently that of the wire, is 1-2 K lower than the expected one, corresponding to the value of the bare YBCO films. However this is only due to the additional resistive shunt of the Au film and not to a change of the superconducting transition temperature of the film. To clarify this point, we have to consider that the resistance $R(T)$ we measure is a parallel combination between the resistance of the YBCO nanowire $R_w(T)$ and the resistance of the gold film on top of the nanowire structures R_{sh}, i.e. $R^{-1}(T) = R_w^{-1}(T) + R_{sh}^{-1}$. The resistance R_{sh} becomes dominant at temperature close to T_C, where it is much smaller than the resistance of the YBCO wire, $R_w(T_C) \approx R_N$. In particular, as we can clearly see in Fig. 5.10a, where we have studied with numerical calculations the influence of different values of R_{sh} on the total resistance $R(T)$ of a YBCO wire with fixed geometry, the onset temperature T^{onset}, at which the resistive transition becomes

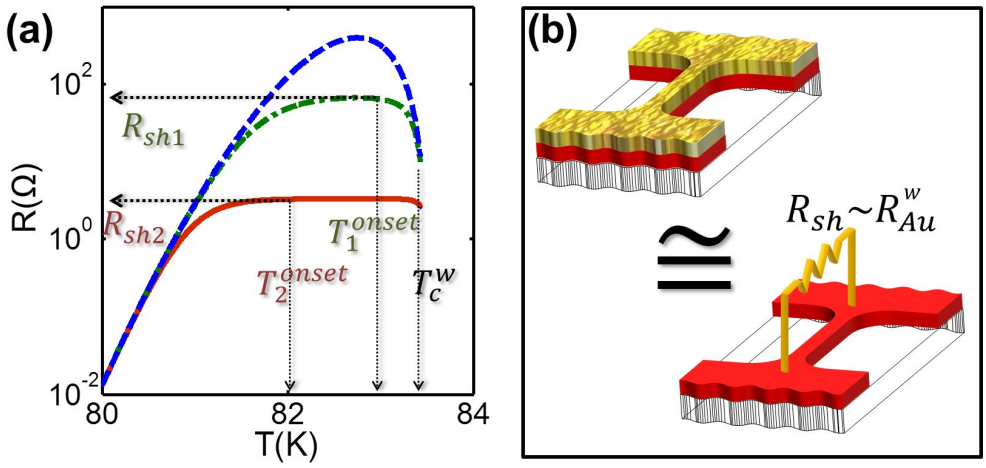

Figure 5.10: (a) Numerically calculated total resistance $R(T)$ for three different values of R_{sh}: $R_{sh,\infty} = \infty$ (dashed line), $R_{sh,1} = 80\ \Omega$ (dash dotted line) and $R_{sh,2} = 4\ \Omega$ (solid line). The difference between the observable onset temperature and the critical temperature T_C^w increases as the shunt resistance is decreased. (b) Equivalent circuit, describing the role of the Au layer: the value of R_{sh} in our capped nanowires can be approximated by the resistance of a gold strip of length $l_{Au} = l_{wire}$ and width $w_{Au} = w_{wire}$, R_{Au}^w, on the top of a YBCO wire.

observable, decreases with decreasing the value of the shunt resistance. Thence, a discrepancy will be present between the T_C of the bare film and the T^{onset} we measure for our capped nanostructures.

In our case, the R_{sh} can be roughly approximated by the resistance R_{Au} of the gold strip of length $l_{Au} = l_{wire}$ and width $w_{Au} = w_{wire}$, on top of the YBCO wire (see Fig. 5.10b).[3]

The temperature broadening in the $R(T)$ of the wires (see Fig. 5.9) can be analyzed according to the models discussed in sec. (2.3.4), considering thermally activated phase slip events or vortices crossing the wires as the dominating source of resistance during the superconducting transition. Both these models predict that the resistive transition gets broader in temperature for decreasing wire width, in complete agreement with what we observe in our nanowires (see Fig. 5.9). For the same reason we have ruled out the Berezinskii-Kosterlitz-Thouless (BKT) theory [155], related to vortex-antivortex pair dissociation in 2-dimensional systems with lateral extensions smaller than λ_P, which does not predict any size dependence in the $R(T)$ broadening.

Our wires are three-dimensional systems and in principle only vortex slips should be considered. However, phase slip theories, although developed for one-dimensional systems, have been demonstrated to give reasonable results also in case of two-dimensional systems [100]. Thence, we have applied both the phase slip and the vortex slip theories to our experimental $R(T)$ data, then comparing the extracted parameters.

[3] A more precise estimation has been derived from simulations of the current distributions in our structures using typical values for the resistivity of Au and YBCO, and the contact resistivity between Au and YBCO. The result is that the shunt resistance R_{sh} can be approximated by the series combination of the Au resistance on the top of the wire, R_{Au}^w, and the resistance associated to the current redistribution from the gold capping layer into the superconducting/low ohmic YBCO electrodes, R_{el}, which is independent on the YBCO wire resistivity.

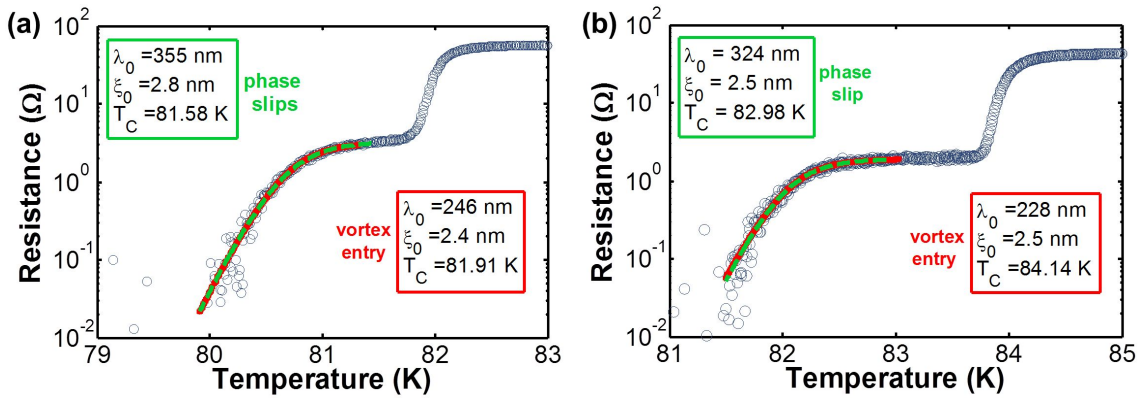

Figure 5.11: We have fitted both with the Little fit (dashed line) and with the vortex slip model (solid line) (a) a 85 nm wide wire grown on MgO (110); (b) a 67 nm wide wire grown on MgO (001).

In regards to the phase slip theories, we have considered the Little model to describe our $R(T)$ curves close to the transition, avoiding the intrinsic limitations of the LAMH model [104]. According to the Little model, the resistance of our YBCO wire is given by equation (2.35), $R_w(T) = R_{Little}(T)$. The energy barrier for phase slip nucleation $\Delta F(T)$writes analytically as:

$$\Delta F(T) = \left(\frac{8\sqrt{2}}{3}\right)\left(\frac{B_C^2(T)}{2\mu_0}\right) wt\xi(T)\,, \tag{5.4}$$

where w and t are respectively the width and the thickness of the wire. Moreover, close to T_C, the coherence length $\xi(T)$ and the critical field $B_C(T)$ can be expressed as $\xi(T) = \xi_0[2(1-T/T_C)]^{-1/2}$ and $B_C(T) = B_C^0(1-T/T_C)$, where $B_C^0 = h(2e\sqrt{2}\pi\lambda_0\xi_0)^{-1}$, λ_0 and ξ_0 are the thermodynamical critical field, the London penetration depth and the coherence length at $T = 0$, respectively (for the analytical determination of these latter quantities, we refer to Appendix C).

Since our wires are covered by a gold capping layer acting as a shunt, the final resistance can be expressed as:

$$R(T) = \left[R_{Little}^{-1}(T) + R_{sh}^{-1}\right]^{-1}. \tag{5.5}$$

In order to describe the broadening of the resistive transition in terms of vortex slips, we have considered the energy barrier for vortex entry expressed by eq. (2.36) [96]. As a consequence, the resistance of a YBCO wire is given by eq. (2.38), $R_w(T) = R_v(T)$. The gold shunt has to be accounted to derive the expression of the total resistance:

$$R(T) = \left[R_v^{-1}(T) + R_{sh}^{-1}\right]^{-1}. \tag{5.6}$$

We have fitted the $R(T)$ of the wires, both grown on MgO (110) and MgO (001), with eqs. (5.5) and (5.6), inserting the dimensions determined with AFM/SEM and extracting λ_0, ξ_0 and T_C as fitting parameters (see Fig. 5.11).

From a comparison between the parameters extracted with the two models, we can observe that the main difference is given by the much higher value of the London

penetration depth in case the Little fit is used. A summary of the parameters extracted by the fits on different wires grown both on MgO (110) and MgO (001) is shown in Table 5.1.

Substrate	λ_0^{Little} (nm)	ξ_0^{Little} (nm)	J_d^{Little} (A/cm^2)	λ_0^v (nm)	ξ_0^v (nm)	J_d^v (A/cm^2)
MgO(110)	340-370	2-3	$\approx$ 3.2e7	235-265	2-3	$\approx$ 6.5e7
MgO(001)	315-340	2-3	$\approx$ 3.8e7	210-240	2-3	$\approx$ 8e7

Table 5.1: Summary of the parameters extracted from the fits of the $R(T)$, considering phase slip and vortex slip models. The values of J_d have been derived using eq. (2.28).

For both the models, we have calculated the expected depairing current density of the nanowires through eq. (2.28), using the values of ξ_0 and λ_0 extracted by the fits, which are typical for YBCO thin films [144]. In particular if considering vortex slips as main source of resistance, the expected values of J_d so calculated, J_d^v, are rather consistent with those extracted from the IV curves at 4.2 K (see Fig. 5.3). Moreover, comparing nanowires grown on MgO (110) and MgO (001), the difference between the extracted J_d is consistent both with the difference between the measured J_C at 4.2 K (e.g. see in Fig. 5.3 the shift between red points and triangles) and with the lower T_C measured on films grown on MgO (110), as a consequence of the large mismatch between the film/substrate in-plane lattice parameters. These results give a confirmation of the validity of the vortex slip fitting procedure to extract physical quantities, as ξ_0 and λ_0, representing the nanowire. Thence, the possibility to explain the broadening in the resistive transition only in terms of the dissipation due to vortices crossing the wire, proves once more the high quality of our nanostructures, preserving pristine superconducting properties because of the presence of the gold capping layer.

To assess the effect of the capping layer on the superconducting properties, we have measured and analyzed the $R(T)$ of a nanowire before and after the removal ("overetching") of the Au layer (see Fig. 5.12). The results are as follows:

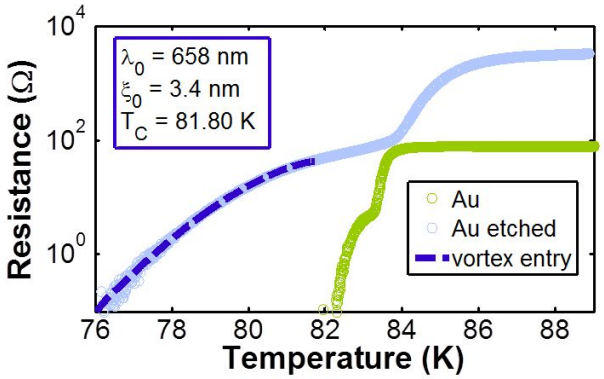

Figure 5.12: $R(T)$ of a 200 nm long YBCO wire grown on MgO (001) before (green circles) and after (blue circles) the eching of the Au capping layer. The blue dashed line is the fit to the vortex slip theory (eq. 2.38).

- As already mentioned previously, without the gold layer acting as a shunt, the onset temperatures of the wide electrodes and of the wire shift to higher values (in particular, the T^{onset} of the electrodes corresponds to the T_C of the bare film.

- The broadening of the superconducting transition of the wire is much bigger after the removal of gold. While the $R(T)$ before the Au etching can be fitted with the vortex slip model, extracting parameters in the ranges listed in Table 5.1, when fitting with the same model the $R(T)$ of the uncapped wire completely unfeasible parameters are extracted (see fitting parameters in Fig. 5.12). Therefore we have to conclude that the very broad superconducting transition is not caused by real physical processes (e.g. motion of vortices across the wire), rather by local damages of the YBCO wire occurred during the last etching step.

6

YBCO nanoSQUIDs implementing nanowires

With the progress in nanotechnologies the development of quantum limited sensors, allowing the measurement of the physical properties of nano-objects with unprecedented resolution, has become crucial. In particular, Josephson junction based nanodevices, such as Superconducting Quantum Interference Devices (nanoSQUIDs), have recently gained a lot of attention for their extreme magnetic flux sensitivity [23, 24]. Within this field, a real challenge is to what extend the flux sensitivity can be improved to be able to detect a single spin, a holy grail for physical measurements [25]: a SQUID loop on the nanometer scale is indeed a crucial requirement for such detection [26].

However, the downscaling of tunnel junction based SQUIDs is an extremely challenging task. In particular, scaling down the dimensions of a conventional tunnel junction to nanometer size implies several drawbacks such as the deterioration of the tunnel barrier, with increased critical current/resistance noise [156], and small critical current values, limiting the working operation range of the SQUIDs far below the transition temperature of the superconducting material used. For these reasons during the recent years a lot of effort has been put into the development of nanoSQUIDs implementing superconducting nanowires in a Dayem bridge configuration [157, 158]. At the moment, the realization of such nanoSQUIDs is well established for Low critical Temperature Superconductors (LTS) [159]. However, nanoSQUIDs made of High critical Temperature Superconductors (HTS) might extend the operational working temperature (from mK to above 77 K) and the range of magnetic field that can be applied compared to Nb based nanoSQUIDs, making them even more attractive for applications ranging from fundamental studies of nano-magnetism in molecules and magnetic nanoclusters to low field magnetic resonance imaging.

Several attempts to achieve HTS nanoSQUIDs, implementing YBCO Dayem bridges, have been done during the last few decades [27, 28, 160, 127]. However a proper SQUID behavior, with a periodic modulation of the critical current in the full temperature range below T_C has never been observed. These results suggest a severe degradation of the YBCO nanostructures during fabrication, highlighted by critical current densities J_C never above 10^6 A/cm^2 at 4.2 K.

In this chapter, we will show the fabrication and transport characterization of our nanoSQUIDs, realized in the Dayem bridge configuration by using the nanowires previously presented [161]. For the first time, critical current modulations have been

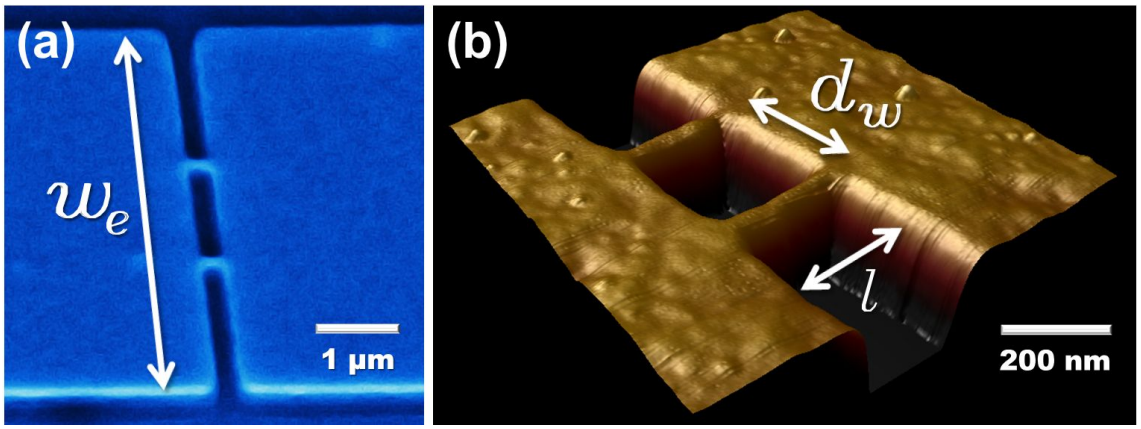

Figure 6.1: (a) SEM and (b) AFM images of two nanoSQUIDs in the Dayem bridges configuration. The loop areas, respectively of 200×970 nm^2 and 200×150 nm^2 are realized with two parallel YBCO nanowires, capped with Au and placed to a distance d_w, connecting two wider electrodes (whose width is w_e).

observed as a function of an externally applied magnetic flux in the full temperature range below the transition temperature T_C of the devices. Both the modulation depth and the period in magnetic field are in good quantitative agreement with numerical computations. The high values of the critical current density we have achieved, demonstrating superconducting properties close to the as grown film, make these devices model systems to study the intrinsic properties of HTS, such as the fluxoid quantization in superconducting loops [162, 29]. Moreover, the record white flux noise below 1 $\mu\Phi_0/\mathrm{Hz}^{1/2}$ we have measured above 10 kHz makes these devices also appealing for the investigation of small spin systems.

6.1 NanoSQUID design

The devices have been realized by patterning both untwinned YBCO films grown on MgO (110) substrates, and twinned YBCO films, provided by Theva GmbH [145], grown on MgO (001) substrates. The nanopatterning procedure is the one described in detail in Chapter 4. As a only difference, to better define square-shaped loop geometries even for very small areas, we have exposed the wider electrodes and the narrower wires in two different e-beam lithographic steps. Typical geometries we have realized for the nanoSQUIDs are shown in Fig. 6.1: two nanowires in parallel, whose length l is in the range 100 - 200 nm, connect two wide electrodes with widths w_e in the range 4-16 μm. Different loop areas have been achieved, by varying the distance d_w between the wires in the range 100 - 1000 nm. All the dimensions have been confirmed by scanning electron microscopy (SEM).

6.2 Transport characterization

Electrical transport properties of the devices have been performed in a ^{3}He cryostat. $R(T)$ measurements and IVCs in the whole temperature range from 300 mK up to the T_C of the devices, have been carried out using a 4-point measurement scheme. The nanoSQUIDs have the onset of the superconducting transition very close to the T_C of the bare films (differing not more than 1 K). Moreover, they have very high critical current densities J_C at 300 mK: on the devices patterned on (001) MgO the average J_C values per wire are in the range $7-9\times10^7$ A/cm^2, close to the GL depairing limit; on devices on (110) MgO they are of the same order of magnitude, although slightly lower. This small reduction of J_C could be related to a greater sensitivity of the YBCO films grown on (110) MgO to the double e-beam resist baking treatment, involved in the nanoSQUID patterning process.

In Fig. 6.2 we show the critical current of two nanoSQUIDs as a function of an externally applied magnetic field. Modulations of the critical current have been observed

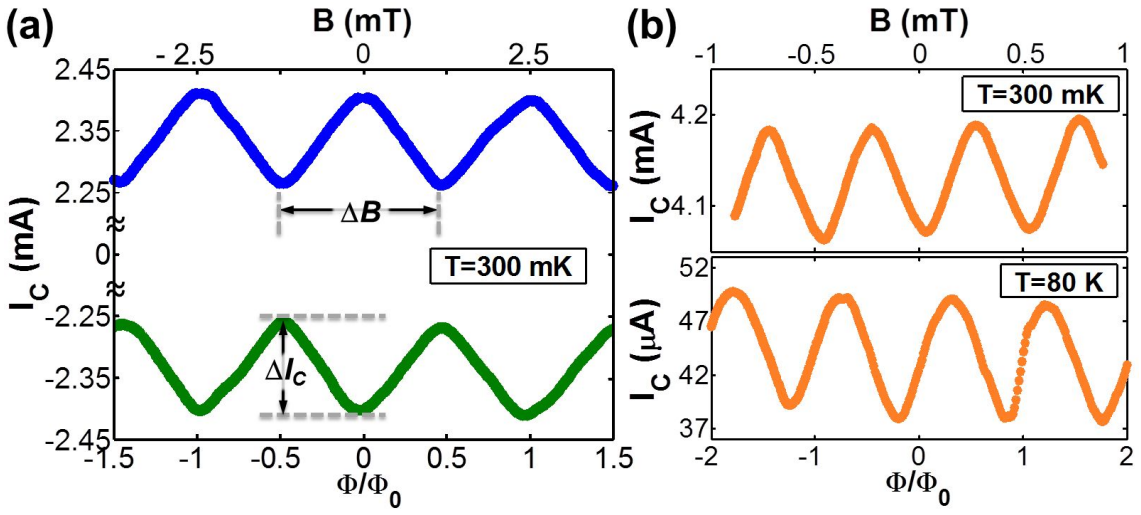

Figure 6.2: Critical current as a function of the applied magnetic field measured (a) at 300 mK, on a device patterned on MgO(110) with a loop area of 130×150 nm^2; (b) at T=300 mK (*upper panel*) and close to T_C (*lower panel*), on a device patterned on MgO(001) with a loop area of 130×1000 nm^2.

in the whole temperature range, up to the critical temperature of the devices. Here, the critical current has been measured by ramping the current and detecting when the voltage exceeded a voltage criterion, the latter being determined by the noise level and the shape of the IVC (usually a value of ~ 2 μV has been considered). From the critical current modulation we have extracted the modulation period ΔB and the relative critical current modulation depth $\Delta I_C/I_C^{max}$, with ΔI_C being the difference between the maximum I_C^{max} and the minimum I_C^{min} values of the critical current (see Fig. 6.2a). The small difference between I_C^{max} values belonging to different lobes within the same modulation (see Fig. 6.2b) is caused by the response of the single junction, which is not point contact-like as supposed in sec. (2.4.1): as a consequence, each nanoSQUID modulation is superimposed to the $I_C(B)$ modulation of the single nanowire. More-

over, the distortion of the critical current oscillations, which is most notable in the shift of the maxima and minima along the flux axis, is due to an asymmetry of the critical currents and/or inductances carried by the two nanowires [163].

6.3 Comparison between numerical and experimental results

To calculate numerically the expected ΔI_C, we have followed the approach by Tesche and Clarke [109]. For this purpose, the knowledge of the current-phase relation (CPR) of the bridges and the inductance of the electrodes is required. Concerning the CPR, our bridges are long ($l \gg \xi$) and wide ($w > 4.4\xi$) nanowires, with cross section $wt \ll \lambda^2$. In this limit, as already discussed in sec. (2.3.3), the CPR is given by the linear approximation of the Likharev and Yakobson expression [93], eq. (2.30). Each nanowire inside the nanoSQUID loop is therefore represented by an arm inductance, where the phase difference between the two ends grows linearly with the bias current. As a consequence, the critical current modulation depth will strongly depend on the value of the nanowire inductance: in particular, it decreases as the inductance increases. From numerical calculations, which have been shown in sec. (2.4.1), we have that

$$\frac{\Delta I_C}{I_C^{max}} \approx \frac{1}{\beta_L} , \tag{6.1}$$

where β_L is the screening inductance factor, given by

$$\beta_L = \frac{I_C^{max} L_{loop}}{\Phi_0} . \tag{6.2}$$

Here, L_{loop} is the total inductance of the SQUID loop, that includes both the contributions of the wires and of the electrodes. Thence, the experimentally measured ΔI_C is directly connected to the inductance of the nanoSQUID, through the β_L parameter.

In our case, we haven't directly measured the nanoSQUID inductance. Instead, we have calculated it by solving the Maxwell and London equations describing the Meissner state (eqs. 5.1) on our SQUID geometry [149]. As expected from their dimensions [108], the main contribution to L_{loop} comes from the kinetic inductance $L_k(T)$ of the nanowires (~ 15 pH at 300 mK), which is one order of magnitude higher than the geometrical value already at 4 K. For the temperature dependence of the loop inductance we have used the two-fluid model for the London penetration depth [39], on which L_k is strongly dependent:

$$\lambda_L(T) = \lambda_0 \frac{1}{\sqrt{1 - \left(\frac{T}{T_C}\right)^2}} , \tag{6.3}$$

The numerically calculated loop inductance $L_{loop}^{num}(T)$ allows to determine a numerical β_L (see lines in Fig.6.3) through eq.(6.3), as[1]

$$\beta_L^{num}(T) = \frac{I_C^{max}(T) L_{loop}^{num}(T)}{\Phi_0} . \tag{6.4}$$

[1] In this expression, we have extracted the $I_C^{max}(T)$ values from the measurements.

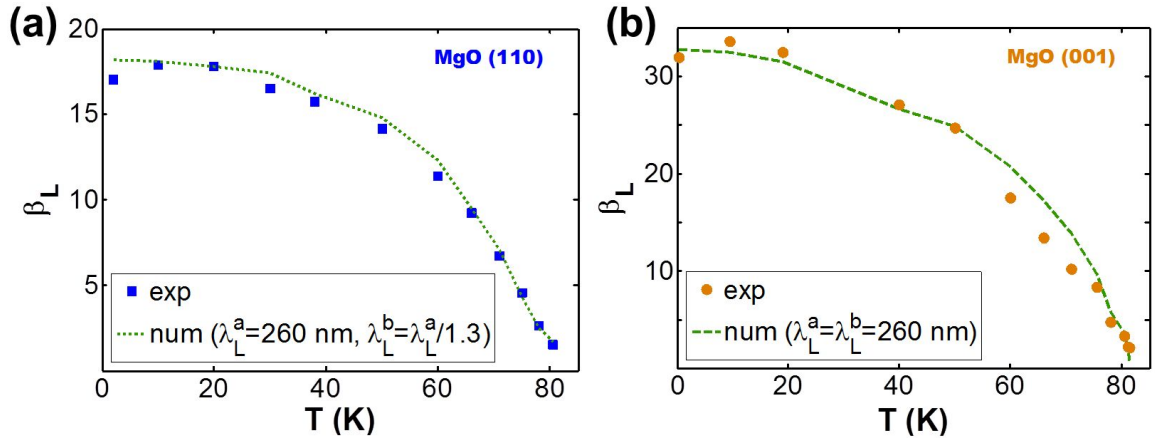

Figure 6.3: Comparison between the experimental (dots) and the theoretical (lines) values of the screening inductance factor β_L as a function of the temperature for nanoSQUIDs patterned on (a) a MgO (110) substrate, considering for the fit a λ_0^a value of 260 nm and the in-plane anisotropy of the London penetration depth; (b) a MgO (001) substrate, considering for the fit a λ_0^a value of 260 nm and assuming the in-plane isotropy of the London penetration depth.

We can now fit the numerical temperature dependence of β_L^{num} with an experimentally determined parameter, β_L^{exp} (see solid symbols in Fig. 6.3), defined through eq.(6.1) as

$$\beta_L^{exp}(T) = \frac{I_C^{max}(T)}{\Delta I_C(T)} \ , \tag{6.5}$$

by using λ_0 as the only fitting parameter.

As shown in Fig. 6.3a, for all the measured YBCO nanoSQUIDs fabricated on MgO (110) the agreement between data and numerical calculations is very good in the whole temperature range, using $\lambda_0^a = 260$ nm and considering the in-plane anisotropy of the London penetration depth, which is consequence of the YBCO films, being untwinned on MgO (110) (as highlighted in sec. 3.4). For the fit, an anisotropy factor of 1.3 has been considered ($\lambda_0^b = \lambda_0^a/1.3$) [70, 71]. Moreover, the λ_0^a value extracted by the fit is very close to that extracted from $R(T)$ measurements, assuming vortex slips as sources of the broadening of the resistive transition around T_C (see sec. 5.3 and table 5.1).

For the YBCO nanoSQUIDs fabricated on MgO (001), as shown in Fig. 6.3b, the agreement between data and numerical calculations is very good, using a $\lambda_0^a = 260$ nm, which is rather close to the value extracted by vortex slip fitting of the $R(T)$ measurements ($\lambda_0^v = 240$ nm), and considering the in-plane isotropy of the London penetration depth (the films on MgO (001) are twinned, so $\lambda_0^a = \lambda_0^b$).

We now focus on the periodicity ΔB of the critical current modulations. In Fig. 6.4 we show the experimentally determined effective area $A_{eff}^{exp} = \Phi_0/\Delta B$ of nanoSQUIDs having different distances d_w between the nanowires. These effective areas A_{eff}^{exp} are far larger than the geometrical areas $A_g = d_w \cdot l$, defined by the distance and the length of the two wires. This can be understood considering that the superconducting phase gradient induced in the wide electrodes by the screening currents contributes to the total phase difference between the two wires resulting in an effective area which

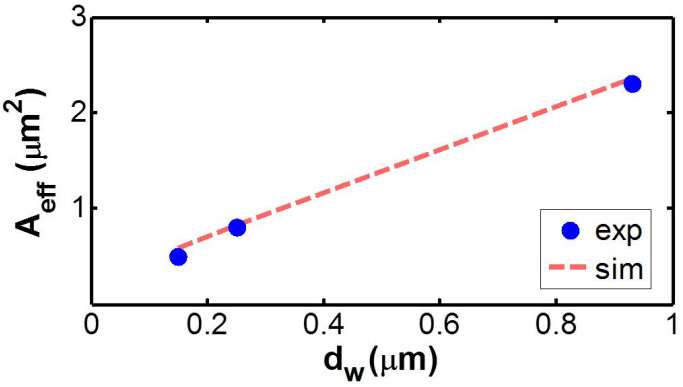

Figure 6.4: Comparison between the experimental (dots) and the calculated (lines) values of the effective area A_{eff} for several devices patterned on MgO (110), with same electrodes width (4 μm) and wire length (150 nm) but different edge to edge distance d_w between the wires. From the plot it could be deduced that $A_{eff} \neq 0$ even if $d_w = 0$: this is simply an artifact caused by the convention to define d_w between the two wire edges rather than between the two wire centers.

is larger than the geometric loop area [164, 157]. These experimentally determined values of A_{eff}^{exp} have been compared with those, calculated numerically, following Ref. [165], $A_{eff}^{num} = m/I_{cir}$. Here, $m = \frac{1}{2}\int \vec{r} \times \vec{j} d\vec{r}$ is the magnetic moment generated by a circulating current I_{cir} around the SQUID loop. The result shows a good agreement between theoretically and experimentally determined values of the effective area (see Fig. 6.4). In particular, our calculations show that the effective area is proportional to the product of the wire distance d_w and the electrode width w_e, $A_{eff} \propto w_e \cdot d_w$. A similar dependency has been analytically found for the effective area in Ref. [157], in the limit $d_w \ll w_e$ and $w_e \ll \lambda^2/t$, with a proportionality constant equal to $8G/\pi^2$ (where G is the Catalan number, defined as $G = \sum_{n=0}^{\infty}(-1)^n/(2n+1)^2 \approx 0.916$). Within these limits, we found a good agreement with such a value, with a discrepancy of about 5%.

6.4 Noise measurements

We have also measured the flux noise of a nanoSQUID (see Fig. 6.5) at a bias current slightly above the critical current and at a magnetic flux bias where the slope of the voltage modulations $V(\Phi)$ (see Fig. 6.6a) is maximized, $V_\Phi = \max(|\partial V/\partial \Phi|)$.

Using a cross correlation measurement scheme (see Fig. 6.6b) [166] we have achieved an amplifier input white noise level of $\simeq 0.7$ nV/$\sqrt{\text{Hz}}$. From the measured voltage noise density S_v we can calculate the flux noise density $S_\Phi = S_v/V_\Phi$. In Fig. 6.5, the flux noise of a nanoSQUID, recorded at a magnetic flux bias corresponding to the $\max(|\partial V/\partial \Phi|)$ displayed in Fig. 6.6a, is shown. Above 10 kHz the measured white flux noise is $S_\Phi^w = 1.2\ \mu\Phi_0/\sqrt{\text{Hz}}$, which is the sum of the intrinsic nanoSQUID flux noise and the noise added from the amplifier. From the measured value of the amplifier noise, including the Nyquist Johnson (NJ) noise of the measurement leads (grey dots in Fig. 6.5), $S_a \simeq 1\ \mu\Phi_0/\sqrt{\text{Hz}}$, we can determine the upper limit for the intrinsic white

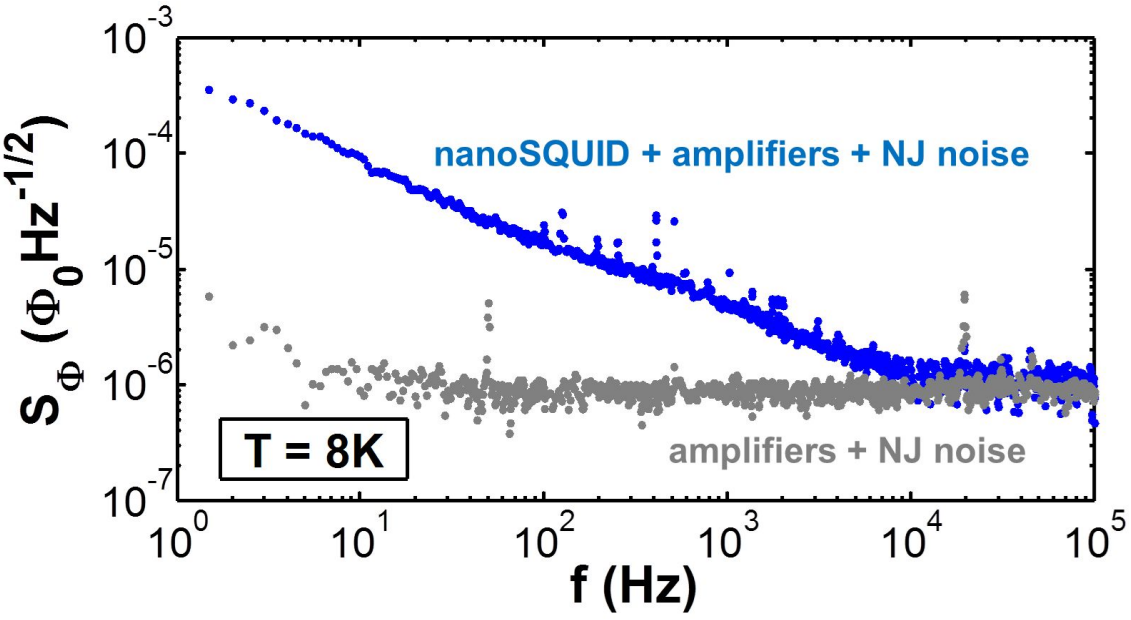

Figure 6.5: Flux noise spectral density S_Φ vs frequency f, measured at $T = 8$ K on a nanoSQUID grown on (110) MgO and with a geometrical loop area $A_g = 0.1$ μm^2.

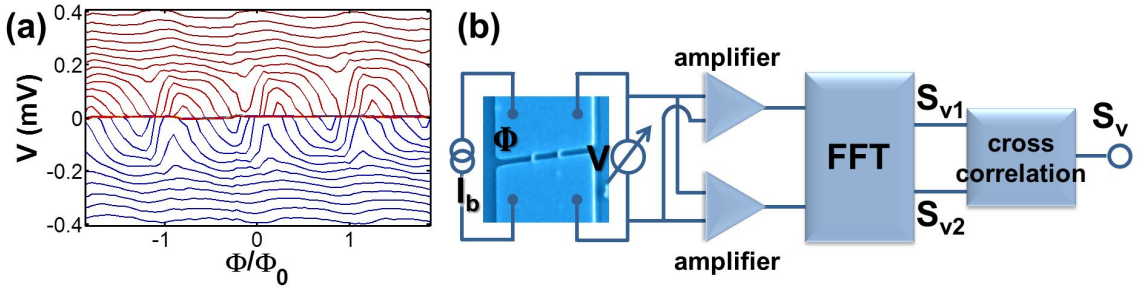

Figure 6.6: (a) Voltage modulations of the nanoSQUID mentioned in Fig. 6.5. $V(\Phi)$ are shown for $I = [-2.5, 2.5]$ mA (in 26 μA steps), among which a voltage modulation of 0.2 mV (peak-to-peak) is present, corresponding to a transfer function $V_\Phi = 1.5$ mV/Φ_0. (b) Basic scheme of the setup used for our noise measurements. The nanoSQUID is biased in current and in magnetic flux. The voltage signal from the device is fed to two independent input amplifiers operating in parallel, followed by a two-channels FFT dynamic system analyzer operated in cross correlation mode. The voltage noise from the nanoSQUID is coherent and correlated in both channels and averages to a finite value. The frequency components of the noises of the two input amplifiers are uncorrelated and they can be reduced by a proper averaging.

flux noise of the nanoSQUID: $S_\Phi^{nS} = \sqrt{S_v^2 - S_a^2} \simeq 0.7\ \mu\Phi_0/\sqrt{\text{Hz}}$. This is among the lowest values for YBCO nanoSQUIDs reported in literature [167], corresponding to a predicted spin sensitivity of only 50 μ_B per $\sqrt{\text{Hz}}$, where μ_B is the Bohr magneton [168].

At frequencies below 10 kHz the noise spectrum is dominated by $1/f$ noise. Since the measured $1/f$ voltage noise spectra do not depend on the flux bias, we attribute the $1/f$ spectrum to critical current noise. A further characterization is currently in progress, mainly aimed at establishing the ultimate flux noise sensitivity at low frequencies: by performing the measurements in bias reversal mode [169] with a custom made electronics, we should be able to remove the noise due to current fluctuations. Here it is worth mentioning that available electronics for SQUID noise characterization [170] does not allow to characterize devices with very high critical current (in the order of one hundred of μA even close to T_C).

7

YBCO nanorings

Nanorings are the basic structures for studying the fluxoid quantization and other coherent quantum phenomena. These structures have attracted a lot of interest during last years, after theoretical studies have predicted the appearance of an additional component in the magnetoresistance of HTS nanorings with flux periodicity h/e, attributed to the d-wave order parameter [30, 31, 32, 171, 172]. At the same time, theories utilizing striped order to explain the mechanism of HTS have predicted the appearance of a periodicity $h/4e$ (corresponding to half a quantum of flux), replacing/coexisting with the usual periodicity of $h/2e$, in rings made with HTS materials [33]. Therefore, the analysis of the magnetoresistance $R(B)$ oscillations, which can be observed in nanorings at temperatures close to T_C (Little-Parks effect), allows the identification of the responsible charge carrier in superconductors, shedding light on different issues on HTS pairing mechanisms. Magnetoresistance measurements made on HTS nanorings [162], and in particular on YBCO submicron rings [29], have shown up to now that in the optimally doped regime only the periodicity $h/2e$ is present.

However, in YBCO nanorings unexpected features have been observed: additional $h/2e$ peaks have been seen in the Fast Fourier Transform (FFT) of the $R(B)$ oscillations, indicating the existence of different characteristic radii, which have been associated to nonuniform vorticity within the ring linewidth [29]. This occurrence, together with the need to extend the search for unconventional $R(B)$ periodicities to different dopings within the superconducting dome, where the various theories for the HTS mechanism give the sharpest predictions, has given a strong boost for further experiments on YBCO nanorings.

We have realized nanorings made of nearly optimally doped YBCO, with cross sections down to 50×30 nm^2. $R(B)$ measurements close to T_C show large magnetoresistance oscillations with period $h/2e$, confirming the $2e$ value for the elemental superfluid charge in optimally doped YBCO. However, differently to what previously reported in literature [29], as a consequence of the high degree of homogeneity of our nanostructures, we have a clear evidence of a uniform vorticity of the order parameter inside the rings. Our nanorings may represent the ideal tools to probe the fluxoid quantization in the underdoped regime of YBCO, where a crossover from $h/2e$ to h/e or $h/4e$ flux periodicities is predicted: as a consequence of the very small arm width

in our devices, the peaks in the FFT spectra can be unequivocally determined.

7.1 Nanoring fabrication and design

The devices have been realized patterning 30 nm thick YBCO films, provided by Theva GmbH [145], grown on MgO (001) substrates and with a T_C of 85 K. The nanopatterning procedure is the one described in detail in chapter 4. Typical ring geometries we have realized are shown in Fig. 7.1a: the rings have an internal radius r_{int} in the

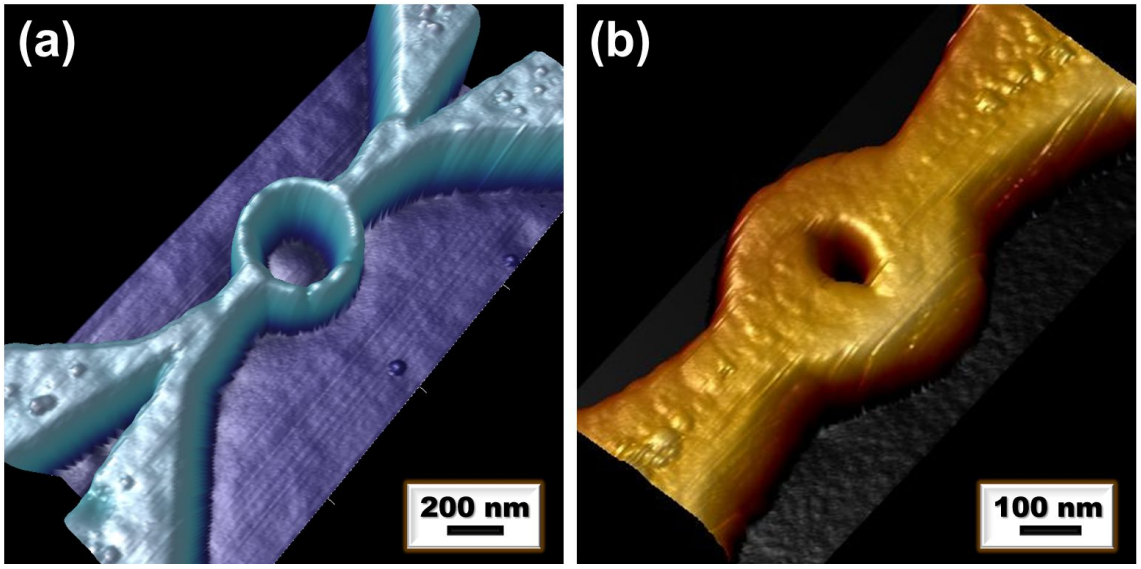

Figure 7.1: (a) AFM picture of a typical 30 nm thick nanoring, with internal radius of 150 nm and a linewidth of 50 nm. (b) AFM picture of a wider nanoring (w = 160 nm), used for comparison.

range 120-200 nm, and arm width w in the range 50-80 nm. The four wide electrodes, used as current and voltage probes during the measurements, are situated very close to the nanostructures. Numerical calculations of the current density have been made: the values of the effective area A_{eff}, we have estimated following Ref. [165] (see sec. 6.3), are in very good agreement with those of the geometrical area of the ring $A_g = \pi r_{avr}^2$, with $r_{avr} = r_{int} + (w/2)$ nm being the average radius.

For comparison, we have also fabricated few wider rings, with arm width in the range 150-200 nm (see Fig. 7.1b).

7.2 Magnetoresistance measurements

$R(T)$ and $R(B)$ measurements of different nanorings have been carried out in a in a Physical Property Measurement System (PPMS) of Quantum Design, using a 4-point measurement scheme. In the following, we will focus on the nanoring shown in Fig. 7.1a, which exhibits the typical characteristics of most of the devices we have measured.

The $R(T)$ has been obtained by biasing the ring with a 500 nA current. Since the electrodes are closely attached to the nanostructure, only the transition related to

the nanoring is observed in the $R(T)$ (see Fig. 7.2a). The broadening of the resistive transition can be modeled in terms of a vortex slip model (eq. 2.38), considering the actual dimensions measured by AFM: feasible values for λ_0 and ξ_0 have been extracted ($\lambda_0 \approx 340$ nm and $\xi_0 \approx 2.5$ nm), only slightly higher than those listed in Table (5.1), probably as a consequence of the thinner YBCO layer [144].This result highlights once more the high quality of our nanostructures, with superconducting properties close to the as grown film, even at cross sections of 50×30 nm^2 (the smallest ones investigated in this thesis).

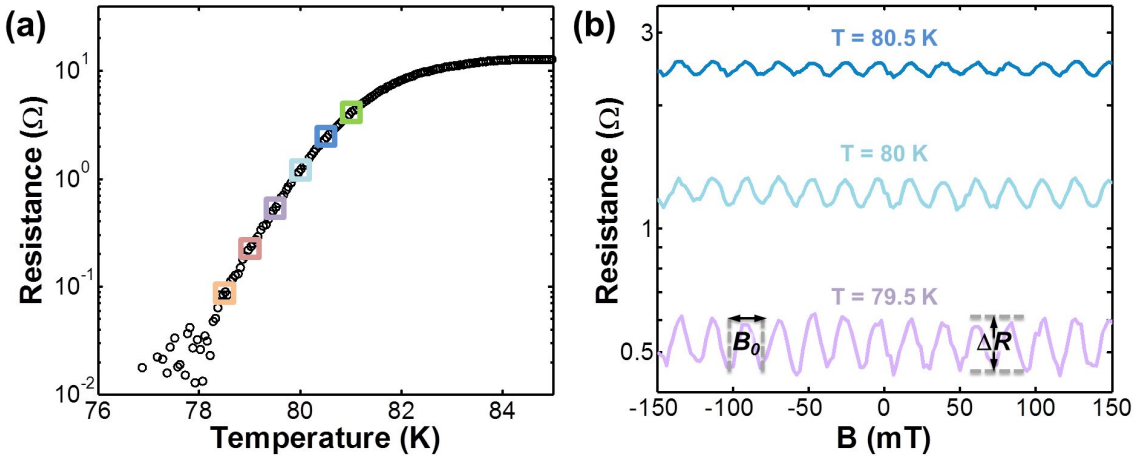

Figure 7.2: (a) $R(T)$ curve of the ring shown in Fig. 7.1a. (b) On the $R(T)$ transition, at fixed values of the temperature, we have applied an external magnetic field, observing large magnetoresistance oscillations (which are reported here for three different temperatures).

We have measured the magnetoresistance of the ring at different temperatures within the resistive transition (see colored opened squares in Fig. 7.2a). Large oscillations appear as a function of the flux enclosed by the ring (see Fig. 7.2b). Considering the geometrical area of the ring $A = \pi r_{avr}^2$, with $r_{avr} = 175$ nm, and the magnetic field periodicity $B_0 = 22$ mT, we have that the flux periodicity: $\Phi = B_0 \pi r_{avr}^2$ is equal to Φ_0, in agreement with a conventional $h/2e$ quantization.

Oscillations of the resistance as a function of the externally applied magnetic field are observed in the range $78 - 82$ K. The temperature dependence of the amplitude of these oscillations, ΔR, is shown in Fig. 7.3a (colored circles).

The most straightforward interpretation for these oscillations is the Little-Parks effect (sec. 2.3.2). According to this model, and following eq. (2.19), the expected temperature oscillations should have an amplitude $\Delta T_C = 0.14 T_C (\xi_0/r_{avr})^2 \approx 1.5$ mK, with $T_C \approx 82$ K, defined at the onset of the superconducting transition, and $\xi_0 \approx 2$ nm. From eq. (2.20), we can calculate the upper limit of the resistance amplitude predicted by the Little-Parks effect. As we can see from the grey dashed line in Fig. 7.3a, the discrepancy between the measured resistance amplitudes ΔR and those predicted by the Little-Parks effect is more than a factor 10.

These large magnetoresistance oscillations, which cannot be ascribed to classic Little-Parks oscillations, have been already observed in HTS nanoloops [162] and ex-

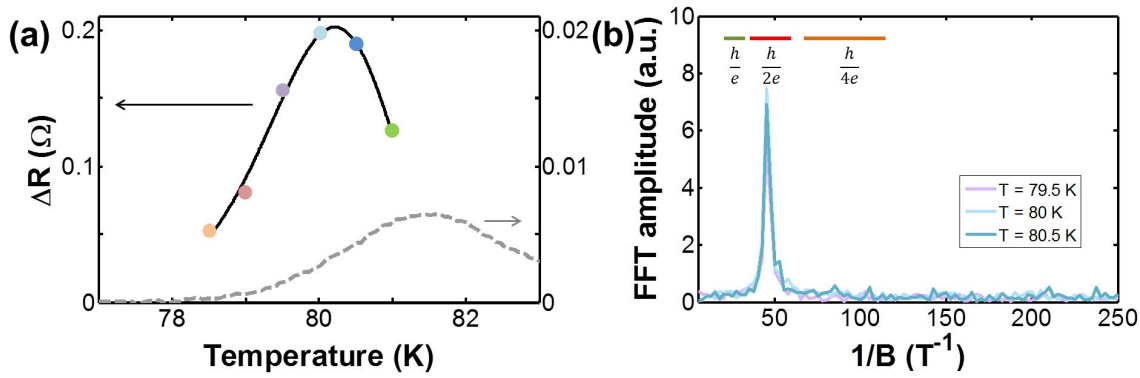

Figure 7.3: (a) Amplitude ΔR of the R(B) oscillations of Fig. 7.2, at different temperatures (points). The solid line represents the fit of the data by using eq. (7.1), accounting for the interaction between thermally excited moving vortices and oscillating screening currents circulating in the two arms of the ring. The dashed line represents instead an upper limit for the amplitude of the resistance oscillations as predicted by the Little-Park effect (its scale, on the right, is expanded by a factor 10). (b) FFT of the three R(B) curves shown in Fig. (7.2b). The h/e, $h/2e$ and $h/4e$ bars indicate the frequency range calculated from ring sizes (the ends of each bar correspond to the internal and external radius of the ring), and assuming h/e, $h/2e$ and $h/4e$ flux periodicity, respectively.

plained in terms of the vortex dynamics, triggering the resistive state in 3-dimensional nanowires (as we have also confirmed through the analysis of the $R(T)$ curve of the ring). In particular, according to this interpretation, the energy barrier for vortex entry, defined in eq. (2.36), becomes oscillatory, as a consequence of the interaction of the thermally excited moving vortices with the screening current circulating in the two arms of the ring, which - as we have previously observed in nanoSQUIDs - is a periodic function of the externally applied magnetic field. The equation describing the temperature dependent amplitude of the magnetoresistance oscillations is [162]:

$$\Delta R \approx R_0 \left(\frac{\epsilon_0^r}{2k_B T} \right)^2 \frac{K_1(\gamma)}{(K_0(\gamma))^3} \ , \tag{7.1}$$

where $\epsilon_0^r = \Phi_0^2 w/(4\pi\sqrt{\pi} r_{avr} \mu_0 \lambda_P(T))$ is the characteristic energy of a vortex in a nanoring, R_0 the resistance at the onset of the superconducting transition, K_0 and K_1 the zero-order and first-order modified Bessel functions of the first kind respectively and $\gamma = ((E_\nu + E_0/4)/(2k_B T)$, with $E_\nu = \Phi_0^2/(4\pi\mu_0\lambda_P(T))\ln(2w/(\pi\xi(T)))$ the energy barrier for vortex entry, in the limit of zero bias. We have fitted our measured $\Delta R(T)$ with eq. (7.1), by using λ_0 and ξ_0 as fitting parameters. As shown by the solid line in Fig. 7.3a, the agreement between the data and the model is excellent, and the values of $\lambda_0 \approx 360$ nm and $\xi_0 \approx 3$ nm, which we extract, are in agreement with those extracted from the fitting of the $R(T)$. In general, magnetoresistance oscillations originate both from the vortex dynamics and from the Little-Parks effect. In our case, the contribution of the vortex dynamics is dominant, as a consequence of the strong thermal fluctuations; at the same time, the contribution of the Little-Parks effect is very small, because of short coherence length in YBCO.

To further analyze the magnetoresistance oscillations, the Fast Fourier Transform (FFT) method has been used. In Fig. 7.3b the FFT spectra are shown, as a function of the temperature. The FFT peak at 46 T^{-1} corresponds to a loop with radius $r = 175$ nm, which coincides with the r_{avr} extracted by AFM. The FFT analysis also allows the following considerations:

- Only one sharp peak in the FFT is present, associated to a $h/2e$ periodicity. In previous experiments on YBCO nanorings, additional and unexpected peaks were instead observed [29]. They have been associated to the presence, within ring arms with $w \gg \xi$ ($w \approx 270 - 300$ nm), of different characteristic radii, with a spacing of $20 - 30$ nm, characterized by a different value of the order parameter vorticity (superfluid momentum). In our case, a uniform vorticity is present, mainly as a consequence of the narrow arm linewidths, associated to the high homogeneity of the superconducting properties in our nanorings.

- The FFT peak position, i.e. the value of the ring average radius, is constant as a function of the temperature, even at temperatures very close to T_C. This result proves once more the highly uniform superconductive properties of our nanostructures, where all the regions show the same T_C and there are no subdomains with depressed superconducting properties induced by damages during the nanopatterning.

- The peak in the FFT spectra can be unequivocally determined and associated to the $h/2e$ periodicity, since there is no overlapping between the frequency ranges associated to different possible periodicities (h/e, $h/2e$, $h/4e$). Because of the finite width of the ring arms, the periodicity of the resistance oscillations in B is associated to a certain frequency range, the extremes of which are given by r_{int} and $r_{ext} = r_{int} + w$. If different frequency ranges (corresponding to different fluxoid quantization) are compatible with the FFT peak, the determination of the fluxon value is uncertain. This ambiguity can be overcome if the arm width w fulfills the condition [1]

$$w \leq r_{int}(\sqrt{2} - 1) \; . \tag{7.2}$$

To highlight the importance of using nanorings with very narrow arms, we have also characterized few "wide" nanorings, not fulfilling the requirement (eq. 7.2) on the arm linewidth. In Fig. 7.4 the main results, related to the nanoring shown in Fig. 7.1b, are summarized. In this case the large magnetoresistance oscillations we have measured on the resistive transition are superimposed to a parabolic background (see Fig. 7.4a). Such background is due to the contribution to the magnetoresistance of each of the two arms forming the nanoring [173]. The FFT spectrum has been determined, considering only the magnetic field range [-100 mT, 100 mT], where the parabolic fitting curve subtraction is more accurate (see Fig. 7.4b). The peak at 22 T^{-1} correspond to a loop

[1] The extremes of each frequency range are $f^i_{min} = 1/B^i_{max} = \pi r^2_{int}/\Phi^i_0$ and $f^i_{max} = 1/B^i_{min} = \pi r^2_{out}/\Phi^i_0$, with $r_{out} = r_{int} + w$ and $\Phi^i_0 = h/e, h/2e, h/4e$, depending on the considered frequency range. The conditions to avoid overlapping between different frequency ranges are $f^e_{max} < f^{2e}_{min}$ and $f^{2e}_{max} < f^{4e}_{min}$. Substituting in these two equations the expressions for f_{max} and f_{min}, the condition (7.2) is found.

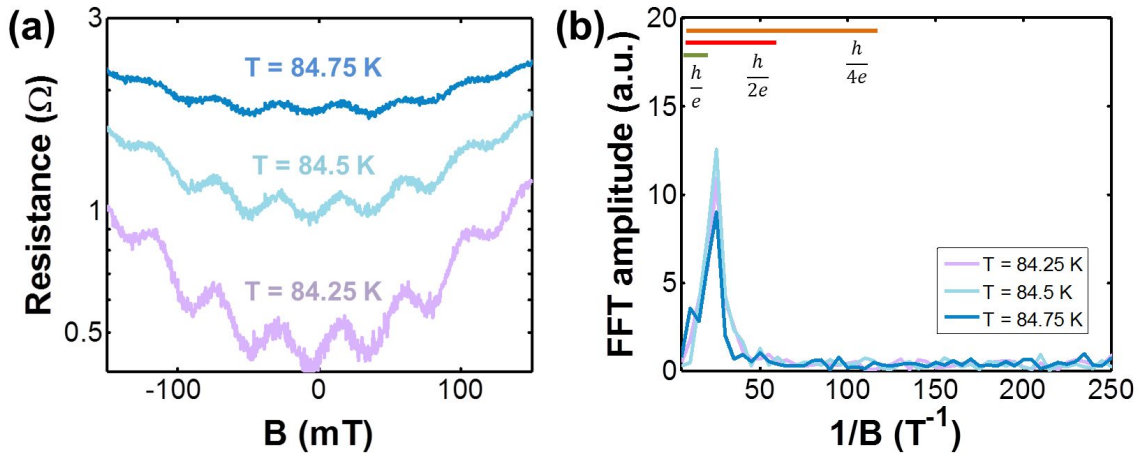

Figure 7.4: (a) R(B) oscillations of the "wide" ring of Fig. (7.1b), measured at three different temperatures. (b) FFT of the three curves of (a), after the subtraction of the parabolic background due to single wire magnetoresistance.

radius $r = 120$ nm, which is fairly close to the AFM extracted average loop diameter $r_{avr} = 115$ nm. For wider rings (as in Fig. 7.4b) the FFT amplitude of the main peak is wider than that of narrower rings (as in Fig. 7.3b), mainly as a consequence of the few examined oscillations (≈ 4). The smaller geometrical area causes larger periods of the oscillations, introducing at the same time complications in the analysis at high magnetic field, because of the appearance of the parabolic background. For instance, the shoulder in the FFT peak at low frequencies is an artifact, due to the subtraction of the background. Finally, as a further drawback induced by the wider cross section, the frequency ranges corresponding to the three possible periodicities overlap, so the determination of the peak at 22 T^{-1} is in principle not univocal[2].

[2]From the analysis done on the narrower ring (Fig. 7.3b), we can associate also this peak to a $h/2e$ flux periodicity.

8

Photoresponse on YBCO and YBCO/LSMO nanowires

High critical temperature superconductors (HTS), characterized by fast thermalization dynamics, are in principle very interesting for realizing devices useful for photodetection. In particular, YBCO thin films and micron size wires have been object of an intense research since the early 90's, based on the investigation of their transient voltage response to laser pulses in the picosecond regime [174, 175, 176]. A slow response, related to thermalization of phonons (bolometric effect), with times down to 1 ns, was observed, together with faster response times, down to the femtosecond regime, attributed to several mechanisms, such as Josephson effect [177], kinetic inductance variations in the superconducting state [178], motion of vortices [179], or electron heating [180]. However the single photon response, requiring a degree of homogeneity of the patterned material, together with very small cross sections, well above that of all the previously mentioned works, has never been observed. As a consequence, despite all the efforts, the focus on nanowire-based single photon detectors (see sec. 2.4) has involved only low temperature superconductors such as NbN, NbTiN, and more recently WSi to fabricate these devices [106, 181, 182].

Since our YBCO nanostructures show superconducting properties close to the as grown films, our aim was to fabricate devices suitable for the single photon response. Basically, what is required for such detection are wires, which have to be very thin, long and not covered by gold. We have been able to fulfill the last two requirements, fabricating nanowires in a series-parallel configurations, covering areas up to 30×10 μm^2 with nanowires down to 100 nm wide, and substituting Au with a protective layer of LSMO, which is transparent to optical photons [183]. However, the further requirement on the thickness has not been fulfilled yet. Transport measurements have shown that, despite the very complex pattern, the superconducting properties are not so much depressed if an LSMO capping is present. We have illuminated the devices with optical laser pulses, measuring a photoresponse, which has been analyzed as a function of the current bias, of the temperature and of the power. With a first approximation, we find that the main origin of such a response is bolometric, being strictly related to the raise of temperature induced by the laser in the YBCO nanowires. Much thinner YBCO wires appears to be a fundamental step for the development of HTS single

photon detectors.

8.1 Working principles of SNSPDs

The working principles of the LTS superconducting nanowire single photon detectors (SNSPDs) will be highlighted to clarify the requirements, which have to be fulfilled by the patterned nanostructures.

Although the microscopic mechanism of photon detection in SNSPDs is still under debate, a supercurrent-assisted, hot spot-formation is considered the main ingredient [106]. The superconducting stripe, biased close to its critical current, is hit by a photon (see Fig. 8.1a). The energy of the absorbed photon E_{ph} is usually much larger than the superconducting energy gap Δ (for optical photons $E_{ph} > 1$ eV, while typically $\Delta \approx 1 - 2$ meV for LTS materials): as a consequence, some Cooper pairs break into

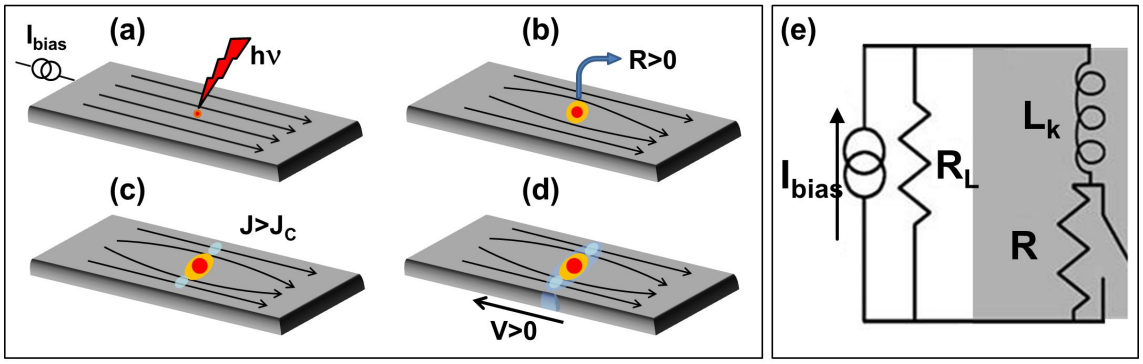

Figure 8.1: (a)-(d) Sketch of the hot spot mechanism. (e) Equivalent circuit of a SNSPD: the wire is represented as a series of a kinetic inductance L_k and a variable resistance R, in parallel with an external load R_L.

quasiparticles of high energy, leading to a region of depressed superconductivity around the absorption site, i.e. the *hot spot* (see Fig. 8.1b). Since the nanowire is biased close to I_C, the hotspot can expand (see Fig. 8.1c). When the whole cross-sectional area of the nanowire becomes normal, the bias current is deviated onto the external load R_L of the read-out circuit, generating the output voltage pulse V on nanosecond time scales (see Fig. 8.1d). By measuring the voltage pulses, the radiation can be detected and counted.

On first approximation, the detector can be modeled as an inductor L_k in series with a parallel connection of a current controlled switch and a resistor R. The whole device is in parallel with the external load $R_L \approx 50\ \Omega$. When the wire is superconducting, the whole applied bias current goes into the detector. As soon as the hot-spot generates a normal belt inside the wire, $R \gg R_L$ and the whole current is redirected into the readout line, where a signal $\propto I_b R_L$ will appear (see Fig. 8.1e).

8.2 Nanowire design

The fabrication of YBCO nanowires presents additional technological difficulties if the goal is to reach the single photon limit. First of all, the sensitivity of a SNSPD is strictly related to the capability to trigger a normal conducting cross section, whose propagation is determined by the electro-thermal properties of the wire [184]: thence, a homogeneous current distribution is a crucial requirement. A nanowire for single photon detection is biased indeed close to I_C: only if all the regions within the wire are characterized by the same value of critical current, the hotspot locally generated can expand to a whole cross section. However, three other conditions have to be fulfilled at the same time:

- *The cross section of the wire has to be extremely small.* The hot spot generated by the photon must cause a significant reduction of Cooper pairs compared to the unperturbed state. This has consequences both on the choice of the material, which has to be characterized by a low density of states at the Fermi level (to have a high relative change of Cooper pairs due to the radiation), and of the geometry. A small volume implies that a small photon energy is required to create the normal conducting zone causing the count event (voltage pulse). In this respect, LTS SNSPDs, as those made of NbN, have thicknesses of only few nanometers[1] [182, 185].

- *The wire has to be extremely long.* The normal resistance R_N of the wire needs to be much higher than R_L to guarantee the total redistribution of the whole bias current from the wire to the readout line, after the device becomes normal. In order to use the nanowires for photodetection experiments, there is the need for a large area coverage for many applications. As a consequence, in NbN several microns long nanowires have been employed as detector units [186].

- *Gold capping is not a good choice for single photon detectors applications.* Its high conductivity leads to a high reflection of the light. At the same time, the Au capping layer works as an electrical shunt for the photoresponse and could also represent thermal shunt for the perturbed area inside the detector. In the case of NbN SNSPDs, an enhancement of the critical current density has been observed by using ferromagnetic materials as NiCu (transparent to optical photons) as capping layers [187].

For LTS materials few nanometers thick and several microns long nanowires can be achieved without observing a severe degradation of the superconducting properties. For HTS materials, instead, the realization of nanowires with highly homogeneous superconducting properties fulfilling these requirements, becomes extremely challenging.

To cover large area devices with narrow wires, we have chosen the *parallel configuration*, first proposed in [185] for realizing a *cascade switch mechanism* in NbN SNSPD. It consists of a serial connection of blocks, each formed by nanowires in parallel. This

[1] In principle the cross section could be reduced shrinking either the width or the thickness of the wire. However, squeezing the width down to 5-10 nm, without undergoing a degradation of the wire homogeneity, is a technological issue even for LTS.

configuration has demonstrated to simultaneously allow large signal amplitudes and fast response. Moreover, the serial connection of blocks of parallel nanostripes also reduces the detrimental effect of single strip defects. The drawback is that the degree of homogeneity of the stripes is even more essential, because the photoresponse is most effective when all the stripes, having the same critical current, are biased around I_C. If few nanostripes have indeed superconducting properties strongly degraded, they can switch to the normal state while all the other stripes inside the block are well below their I_C, so preventing the occurrence of the cascade switch mechanism.

As regards the capping layer, some devices have been fabricated removing completely the Au layer from the top of YBCO by a further Ar^+ etching at the end of the nanopatterning procedure, even though we have demonstrated this is detrimental in achieving "pristine" superconducting properties. In addition, we have investigated a new protective material, the ferromagnetic LSMO, which has been reported to be compatible with YBCO both chemically and structurally [188]. Moreover, it has important functionalities in the context of photodetectors, as already discussed in sec. (3.5.2). By patterning YBCO/LSMO films, LSMO acts as a cap layer for YBCO during the last Au etching step, preventing the milling species from vertically impinging on the top surface of the nanowires, causing a degradation of the superconducting properties.

In conclusion, using the same nanopatterning procedure described in detail in chapter 4, we have fabricated 50 nm thick YBCO and YBCO/LSMO nanowires on LAO substrates, embedded in 7, 9, 11 and 13 blocks of 3 parallel wires (see Fig. 8.2). The

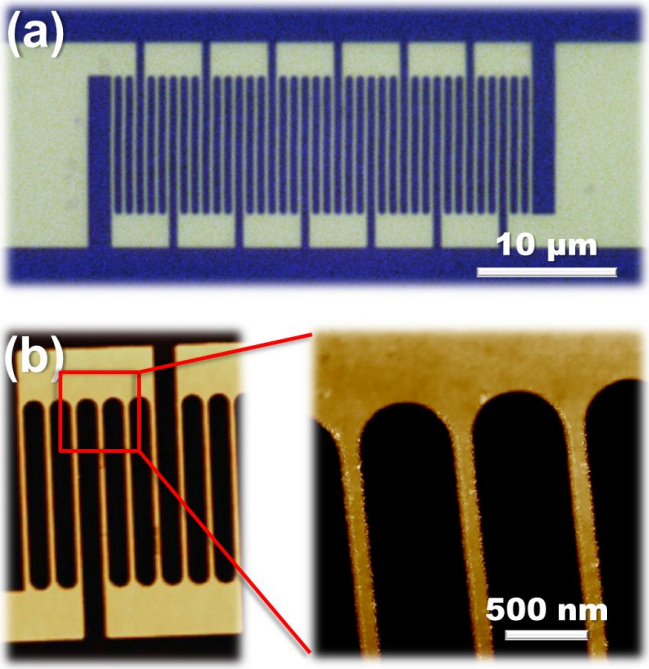

Figure 8.2: (a) Optical picture of a typical device realized for photo-response experiments, composed by serial connections of 300 nm wide parallel YBCO nanowires. (b) AFM picture of several 130 nm wide YBCO nanowires. The rounded corners between the wires and the wider electrodes are aimed to avoid the reduction of the critical current due to current crowding effect.

nanowires widths are in the range 90-500 nm, while the lengths - which increase proportionally to the widths - are up to 10 μm. The distance between wires is always fixed to 500 nm. We have been able to achieve devices covering areas up to 30×10 μm^2, with a filling factor of 50%. To minimize current crowding effects, which could be a further source of reduction of the critical current densities in the nanowires, the edges between the wires and the wider electrodes have been designed with a rounded shape (see Fig. 8.2b).

8.3 Transport characterization

To probe the quality and the degree of homogeneity of the YBCO and YBCO/LSMO nanowires, we have extracted their critical current densities J_C from current-voltage characteristics, measured down to $T \approx 5$ K both before and after the final etching of the Au capping layer (see Fig. 8.3a).

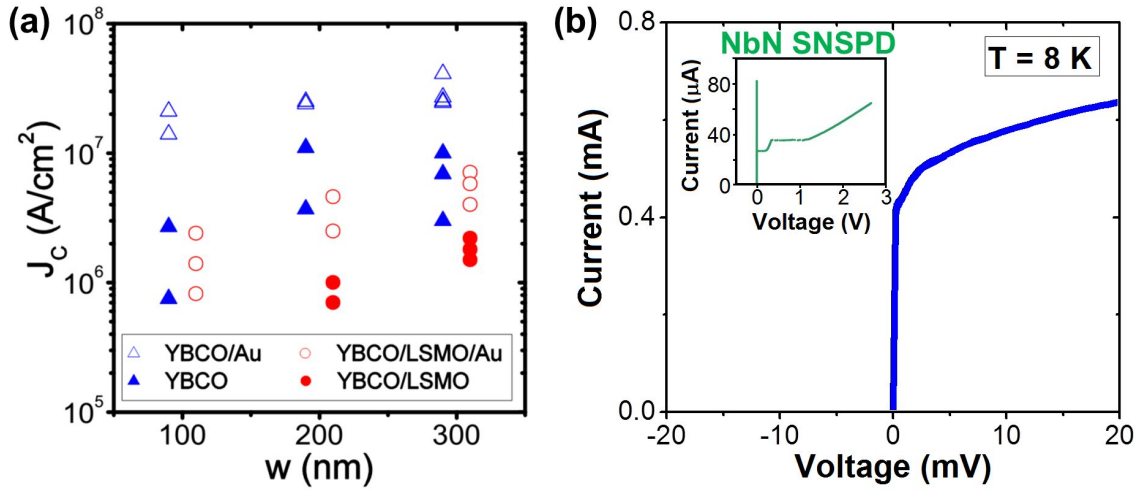

Figure 8.3: (a) The critical current densities of the YBCO/LSMO (*circles*) and YBCO (*triangles*) nanowires, extracted from from the IVC at $T \approx 5$ K of different devices, are shown for three different widths (100, 200 and 300 nm), both before (*blue*) and after (*red*) the Au removal. The data sets belonging to YBCO (YBCO/LSMO) have been shifted to the left (right). (b) Typical flux-flow like IV characteristics of a device made of 130 nm wide YBCO nanowires, after the removal of the Au capping. In the inset, typical IVC of a NbN SNSPD, where a clear switch, of the order of volts, triggering the whole device to the normal state, is present (adapted from [185]).

When the gold is still present, the IVCs, taken in a ^{3}He cryostat using a four point probe configuration, show that pure YBCO nanowires have J_C of $2 - 5 \cdot 10^7$ A/cm^2 at 4.2 K, independently of the wire width. The small discrepancy with the higher values reported in other YBCO nanostructures (see Chapters 5-6) can be understood considering that these wires are much longer and that they are grown on LAO substrates, where twin boundaries have been reported to affect the superconducting properties of YBCO [114]. The extracted critical current densities of YBCO/LSMO nanowires are one order of magnitude lower than YBCO/Au nanowires. This reduction could

be associated to the F/S proximity effect (probably reducing the effective thickness of the superconducting layer) or to the Sr contamination of the superconducting layer [189, 190], possibly enhanced by the reduced dimensions of the YBCO nanowires. However, for wires 200 and 300 nm wide, the measured critical current densities are almost width independent and the spread of values among devices with the same geometry is quite limited.

After the Au capping is completely etched, the fundamental role of the LSMO layer becomes clear. In the case of bare YBCO nanowires the critical current densities are severely reduced, almost by a factor of 10, for all widths, as already discussed in sec. (5.1.1), and a spread of J_C values bigger than 75% is present in devices with the same geometry. This spread implies the presence of local damages randomly distributed, affecting the degree of homogeneity of the nanostripes. By considering instead YBCO/LSMO nanowires, we can notice that the wire homogeneity is preserved. We have measured a J_C spread that is always lower than 50% while the J_C values are reduced maximum by a factor of 4 (after removal of the Au layer on LSMO).

In Fig. (8.3b), a typical flux-flow like IVC of a YBCO nanodevice after the Au etching is shown (the behavior is the same for YBCO/LSMO nanowires). The measured resistive branch represents an intermediate state where the device is only "locally" normal: the high value of the thermal conductivity in YBCO ($\sim$ 2 $\mathrm{Wm^{-1}K^{-1}}$)[140] prevents self-heating effects that could bring the whole device to the normal state just above the critical current I_C. This is what happens for instance in NbN single nanowires [191] and SNSPDs [185] (see inset in Fig. 8.3b), where the thermal conductivity is almost two orders of magnitude lower [192]. In this case the IVCs are highly hysteretic, with a difference up to the 70% between the critical and return currents, and a very large voltage switch (of the order of several volts) occurring just above the critical current, which brings all the nanowires into the normal state. The different current-voltage characteristics (related to different intrinsic physical mechanisms), imposes a severe limitation for the usage of YBCO nanowires as single photon detectors. Considering the equivalent circuit in Fig. (8.1e), in the case of NbN nanowires, the device switches instantly from $R = 0$ to $R = R_N \gg R_L$, so favoring the redistribution of all the bias current to the readout line, where the signal appears. In the case of YBCO nanowires, the hot spot is not able to drive a whole nanowire "belt" into the normal state, but only triggers the device to the resistive state ($0 < R \ll R_N$), where most probably fluxon dynamics plays a fundamental role [96]. In this case the cascade flow of I_b to the external load cannot happen.

8.4 Photoresponse measurements

Photoresponse experiments have been carried out mounting the devices in a liquid helium flow cryostat with optical access. Electrical connections are given by wire bonds to high bandwidth and low bandwidth cables going to room temperature. The low bandwidth connections are used to dc bias the devices, while the output signals are carried by the high bandwidth connection to two cascaded 1 GHz bandwidth amplifiers[2]

[2]Using these amplifiers, the detection of non-equilibrium signals on picosecond scale is not allowed.

with an overall voltage gain of 400 (for more details, see Appendix B).

We have recorded IVCs of devices with and without a dc 1550 nm laser illumination as shown in Fig. (8.4). The IVCs with and without radiation differ, mostly around the critical current, where under illumination the I_C decreases down to $85 - 95$ % of its unperturbed value.

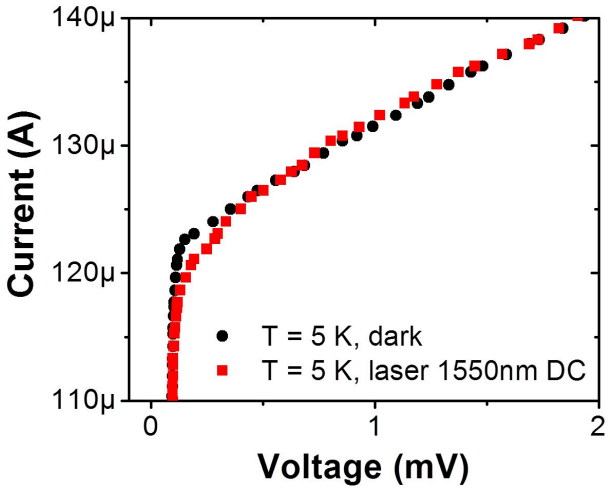

Figure 8.4: Current-voltage characteristics (IVCs) of a device made of 100 nm wide YBCO nanowires, measured at 5 K with (red squares) and without (black circles) a dc 1550 nm laser illumination. The difference is remarkable around the critical current.

A voltage response is measured when the devices are illuminated with optical laser pulses with 1550 nm wavelength, with a rise and fall time of 3 ns, a duration of 10-500 ns, an intensity of about 50 nW/μm^2 and at a repetition rate of 1 MHz (see Fig. 8.5a). As a first step, we have studied at $T = 5$ K the evolution of the voltage response as a function of the applied bias current. When the devices are biased far below the critical current, no photo signals can be measured. By biasing the nanowires slightly below and above I_C, a clear voltage response is observed, in correspondence with the laser pulses. In particular, we can distinguish between two different regions in which the photoresponse can be measured. The first one is accessible when biasing the devices from $\approx 0.85 \cdot I_C$, (the I_C value when the photoresponse signal appears) up to the critical current I_C (see Fig. 8.5b and inset). Here the signal pulse amplitude increases exponentially with the bias current for all the devices, reaching its maximum in correspondence of the critical current ($\approx 0.99 \cdot I_C$). The second region instead corresponds to bias currents higher than I_C. In this case, the signal pulse amplitude slowly decreases by increasing the bias (see Fig. 8.5b): at high bias ($> 2 - 3 \cdot I_C$), it vanishes completely or it reaches a very small saturation value ($\approx$ 2-5 μV). The amplitude of the voltage signal around I_C is $\approx$ tens-hundreds of μV: it increases as the nanowire width increases, because more current redistributes into the external load, and - for a fixed geometry - it is higher (20%-50%) if the devices are capped with LSMO.

The photoresponse has been also studied as a function of the temperature (see Fig. 8.6a). Voltage pulses, in correspondence with the laser pulses, are present from

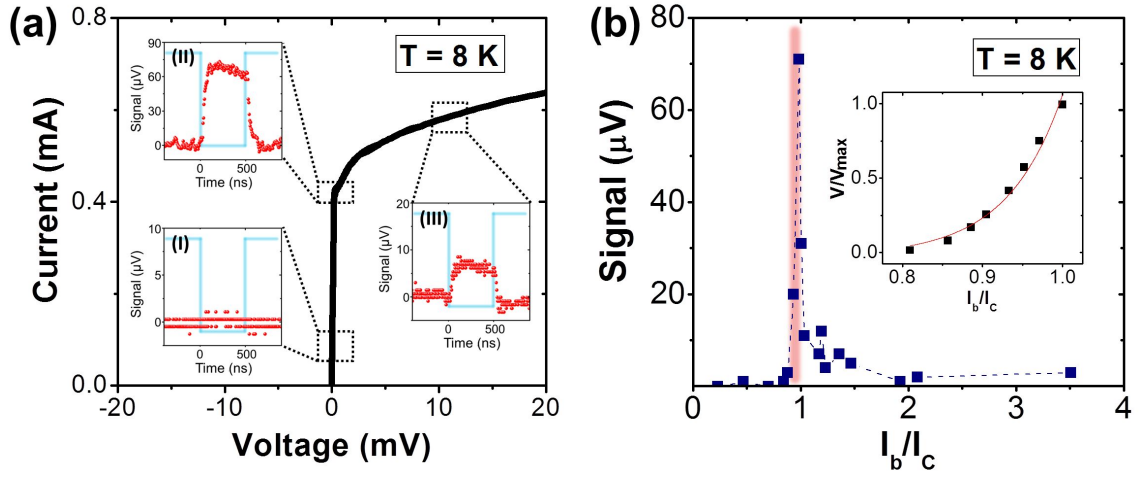

Figure 8.5: (a) IVC measured at $T = 8$ K for a device made of 130 nm wide YBCO nanowires. The three insets show the photoresponse signal (red circles) measured at three different bias currents, corresponding to different regimes in the IVC: (I) far below the critical current ($I_b/I_C = 0.23$), where no photoresponse is observed; (II) around the critical current ($I_b/I_C = 0.99$), where the maximum voltage signal is measured; (III) on the resistive branch ($I_b/I_C = 1.36$), where the photoresponse has a finite value, though reduced with respect to (II). The light blue signals in the three insets correspond to the inverse light pulses of the ac 1550 nm laser used to illuminate the devices. (b) Photoresponse signal as a function of the applied bias current (normalized to the critical current value), for the device whose IVC is shown in panel (a). In the region below I_C, which has been highlighted in pink, the dependence of the voltage signal on the bias current is exponential (inset).

5 K up to T_C, which, depending on the wire width, is in the range 80-85 K. The maximum photoresponse, visible at I_C, decreases as a function of the temperature, with a stronger dependence at lower temperatures (see Fig. 8.6b). Moreover, studying the signal dependence on the bias current at different temperatures, we may notice that the enhancement of the signal around I_C is very strong at lower temperatures, while at T slightly below T_C the photo-signal is almost independent of the bias current.

This behavior suggests that the main contribution, to the photoresponse signals we observe, has a bolometric nature, i.e. it is caused by a raise of temperature δT, induced by the interaction with photons. The IVC changes due to a temperature variation; as a consequence, the voltage changes as $V(I, T+\delta T) - V(I, T)$, possibly giving rise to the signal we measure. To our knowledge, a complete model, describing the effect of the heating on superconducting nanowires, is still missing. To get a qualitative description of the phenomenon, we can consider the IVCs of a resistively shunted junction (RSJ, see Fig. 8.7a): although this modelization cannot be rigorously used in our case, the overall behavior of the IVCs of the nanowires is similar to that of the RSJ model (see Fig. 8.4). The equation describing the dynamics of a Josephson junction in presence of thermal noise, according to the RSJ model [193, 194] , is the following:

$$\frac{1}{R}\frac{\hbar}{2e}\frac{d\phi}{dt} + I_C \sin\phi = I + \xi(t) \ , \tag{8.1}$$

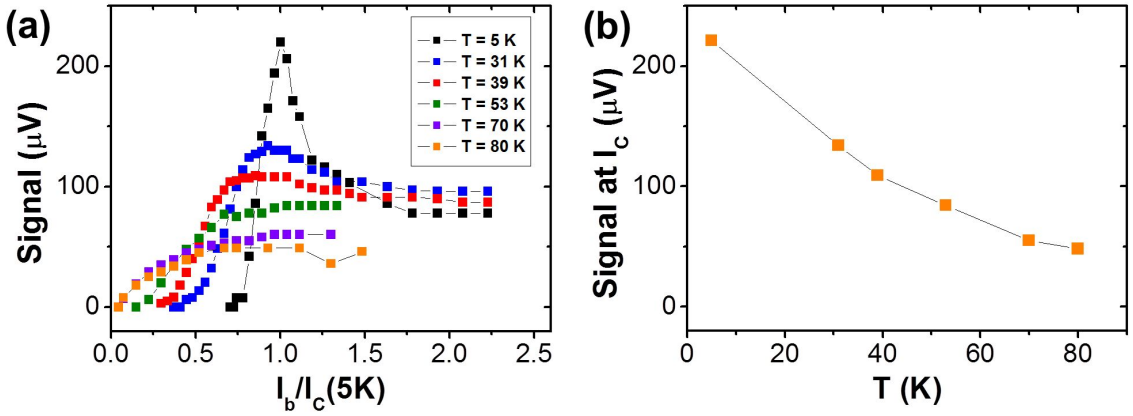

Figure 8.6: (a) Photoresponse signal as a function of the applied bias current measured at different temperature up to the T_C of the device, which is made by 500 nm wide YBCO nanowires. The maximum signal, measured at I_C, is plotted as a function of the temperature in panel (b). In both the panels, the lines are used only to guide the eye.

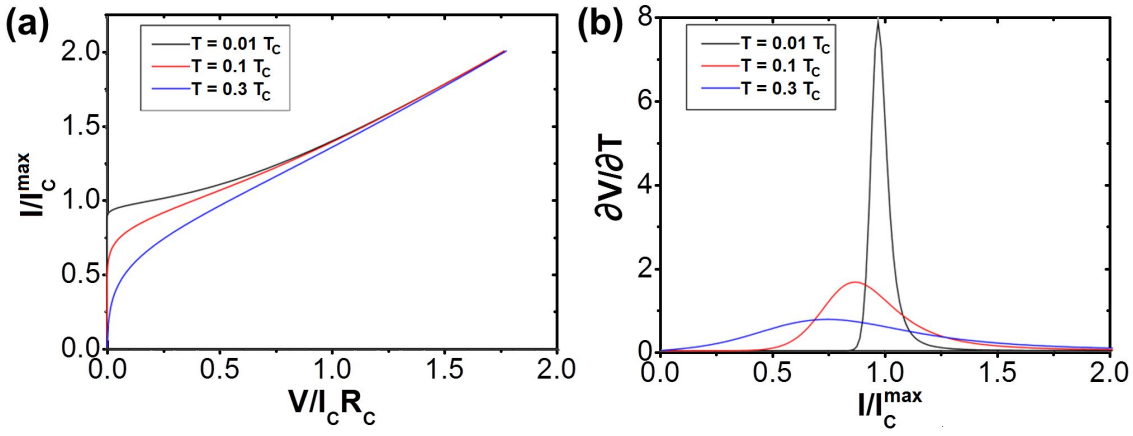

Figure 8.7: (a) RSJ IVCs at three different temperatures. The derivatives $\partial V/\partial T$ as a function of the current, normalized to the I_C of the lowest temperature, are shown in (b). It is worth noticing the similarity with Fig. (8.6a).

with ϕ phase difference across the junction and $\xi(t)$ the noise. For simplicity, we can assume that the noise is white and write its correlator as

$$\langle \xi(t)\xi(t') \rangle = \frac{2k_B T^\star}{R_{qp}(T_1)} \delta(t-t') \ , \tag{8.2}$$

where $T^\star$ is the noise temperature and R_{qp} is the quasiparticle resistance. The exact solution of eq. (8.1) can be found in Ref. [195]: the RSJ IVC in presence of thermal noise, which is plotted in Fig. 8.7, writes as:

$$V(I) = \frac{4\pi e k_B T^\star R_{qp}(T_1)}{\hbar \int_{-\pi}^{\pi} d\phi_1 \int_{-\infty}^{\phi_1} d\phi_2 \exp[-\frac{\hbar I}{2ek_B T^\star}(\phi_1-\phi_2) - \frac{\hbar I_C}{2ek_B T^\star}(\cos\phi_1 - \cos\phi_2)]} \ . \tag{8.3}$$

The derivative $\partial V/\partial T$ of the theoretical RSJ IVCs, as a function of the bias current at different temperatures is shown in Fig. 8.7b. It is very similar to the photoresponse in Fig. 8.6a, which we have experimentally measured. The main difference is above I_C: the I-V curve of the RSJ model is linear, corresponding to a resistance $R = R_N$, leading to a $\partial V/\partial T$ which is negligible already at $I_b = 1.5 \cdot I_C$. For our nanowires instead, as already previously discussed, above I_C the system is in a resistive state, where the resistance changes continuously as a function of the bias current, with values $0 < R \ll R_N$. This facts determines the main difference of the photoresponse of our nanowire with respect to the RSJ model in presence of thermal noise.

The hypothesis of a bolometric nature of the photoresponse is also confirmed by the variation of the shape of the IVC when we illuminate the nanowires with the laser (see Fig. 8.4), mostly changing around I_C at low temperatures. A further support to this hypothesis comes from the dependence of the photoresponse signals on the laser power. As it can be seen in Fig. 8.8, the amplitude of the photoresponse signal, measured at

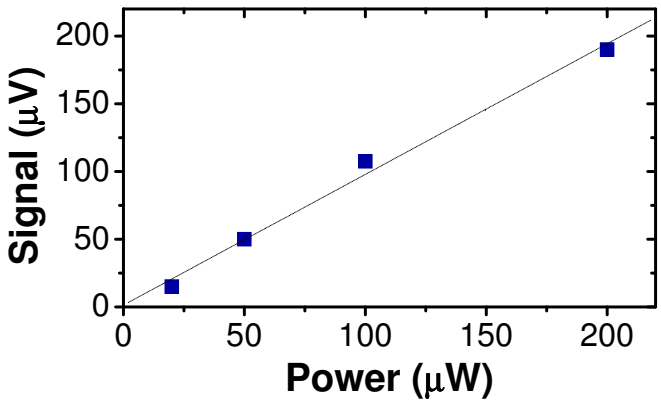

Figure 8.8: Photoresponse signals, measured at $T = 5$ K using a bias current $I_b = I_C$, as a function of the laser power on a device made of 500 nm wide YBCO nanowires (blue dots). Black line represents the linear fit to the data, used to determine the responsivity of the nanowire devices.

$I_b = I_C$, decreases linearly by reducing the power of the laser [196]. In particular, if the laser power is reduced by a factor 10, the photoresponse disappears. In correspondence with such value of power, the IVC of the devices does not change, when illuminated by the dc laser (differently than in Fig. 8.4). From this power dependence, we can calculate the responsivity, defined as the ratio between the detector output signal and the absorbed radiation power. From the values reported in Fig. 8.8, we can estimate a responsivity of 1 V/W at 5 K. This represents only an approximate value, since we haven't consider the actual radiation power absorbed by the YBCO nanowires. For a better estimate, we should also consider the system coupling efficiency and the actual dimensions of the devices with respect to the laser beam.

Although the heating appears as the dominant mechanism giving rise to the photoresponse, we cannot exclude a possible interaction between the light and the vortices crossing the wires (which have been recently accounted as a possible cause of photon counts in SNSPDs [197, 198]).

However, more experiments will be needed, mainly aimed at reducing the cross sections of the nanowires, i.e. at decreasing their thicknesses. This is an essential prerequisite to achieve normal belts inside the nanowires by means of a small photon energy. For this purpose, the usage of LSMO will be crucial, since we proved it has a beneficial role in preserving the homogeneity of the nanowires. It has been reported that the LSMO layer induces at the interface with YBCO a non-superconducting dead layer [199], reducing even further the effective cross sections. In particular, we plan to investigate the effects of the thickness reduction on the dynamics of the resistive state of our devices which, as previously mentioned in sec. (8.3), appears to be the main limitation for the use of HTS nanowires as SNSPDs.

9 Conclusions

In this thesis we have realized YBCO nanowires, with cross sections down to 40×50 nm^2, and employed them in nanoSQUIDs and optical sensors.

We have overcome the limiting issues in establishing reliable nanofabrication routines for YBCO, due to the chemical instability (related to oxygen out-diffusion), and the extreme sensitivity to defects and disorder due to very short coherence length of this material. Through an improved nanopatterning procedure, based on e-beam lithography in combination with an amorphous carbon mask and a very gentle Ar^+ ion etching, by keeping a capping layer of Au on the top of the nanostructures, we have achieved nanowires preserving "pristine" superconducting properties, very close to the as-grown films. The benchmark of their quality is given by the very high critical current densities they carry (up to 10^8 A/cm^2), which are very close to the theoretical depairing limit. Therefore, these structures represent model system to study HTS, since the properties they show are strictly related to the superconducting material, scaled to the nanoscale, and they are not ruled by damages and defects associated to the nanopatterning procedure.

Different experiments have been done, employing these nanowires in more complex devices. The results we got pave the way for new exciting experiments, which will be object of future works, exploring HTS superconductivity at the nanoscale both for fundamental studies and applications:

- We have fabricated and characterized YBCO nanoSQUIDs, employing very short nanowires in the so-called Dayem bridge configuration. These devices, working in the whole temperature range from 300 mK up to their critical temperature ($\approx$ 82 K), have revealed an ultra white low-noise below 1 $\mu\Phi_0/\sqrt{\text{Hz}}$ above 10 kHz, corresponding to a predicted spin sensitivity of only 50 μ_B per $\sqrt{\text{Hz}}$. These properties make our devices very attractive for many applications: in the next future, we will use them as magnetic flux sensors, investigating the magnetic moment of small ensembles of spins in a wide range of temperatures and magnetic fields. In particular, it could be very interesting to study magnetic nanoparticles in their transition from their paramagnetic to the ferromagnetic state, which has been limited until now by the critical temperature of Nb-based devices, lower than the typical T_{Curie} of the magnetic nanoparticles [200].

- We have realized YBCO nanorings, measuring the magnetoresistance close to T_C. Large oscillations have been measured, which can be associated to the vortex dynamics triggering our nanowires to the resistive state. The FFT spectra have shown, for the nanorings with narrower linewidth, a single sharp peak: this peak, associated to $h/2e$ periodicity, as predicted for optimally doped YBCO, represents a clear evidence of a uniform vorticity of the order parameter inside the rings, confirming the high degree of homogeneity of our structures. Therefore, it could be exciting to study, with these nanorings, the fluxoid quantization in the underdoped regime of YBCO, where a crossover from $h/2e$ to h/e and $h/4e$ is predicted. It is mainly for this purpose that we are working in the optimization of the growth conditions of underdoped YBCO films, as mentioned in sec. (3.5.1).

- The homogeneity of our nanowires, together with the fast relaxation times of the YBCO, gave the boost for the realization of devices, aimed at the detection of single photons. This goal required the use of very long wires (up to 10 μm), covering large areas ($\approx$ 300 μm^2). Crucial requirement is the homogeneity of the superconducting properties within different regions of each device. This requirement cannot be achieved by using a Au capping layer. we have therefore engineered YBCO/LSMO nanowires showing encouraging homogeneity properties. We have done preliminary photoresponse measurements on these devices, detecting signals whose main origin appears to be mostly bolometric. More experiments are already planned, addressed at decreasing substantially the thickness of the devices, which is a prerequisite to achieve an hot spot in the wires after a single photon is absorbed. The use of a ferromagnetic LSMO layer, employed as capping for preliminary photoresponse studies appears to be the natural route for future investigation.

- Our YBCO films grown on (110) oriented MgO substrates are untwinned. This occurrence, only observed in films grown on vicinal angle cut so far, can give new boost to new experiments (currently in progress) aiming at studying the in-plane anisotropy of the superconducting properties in these films. In particular, nanowires with different width have been patterned at different in-plane angles with respect to the substrate (see Fig.9.1a). Their J_C has been measured, and it shows an angular dependence for narrower ($\approx$ 85 nm) wires, which smears out for wider ($\approx$ 140 nm) nanowires (see Fig.9.1b). The difference of more than one order of magnitude between the maximum and the minimum value of J_C, measured at 90° and 30° respectively, cannot be only explained in terms of the different values of the London penetration depth along the two in plane directions a and b. However, the homogeneity of our nanostructures guarantees that this angular dependence has to be directly connected to some intrinsic properties of YBCO. To understand these measurements, and investigate their possible connection with the film morphology, a deep structural investigation is currently in progress, by means of atomic resolution Transmission Electron Microscopy studies and nanodiffraction experiments.

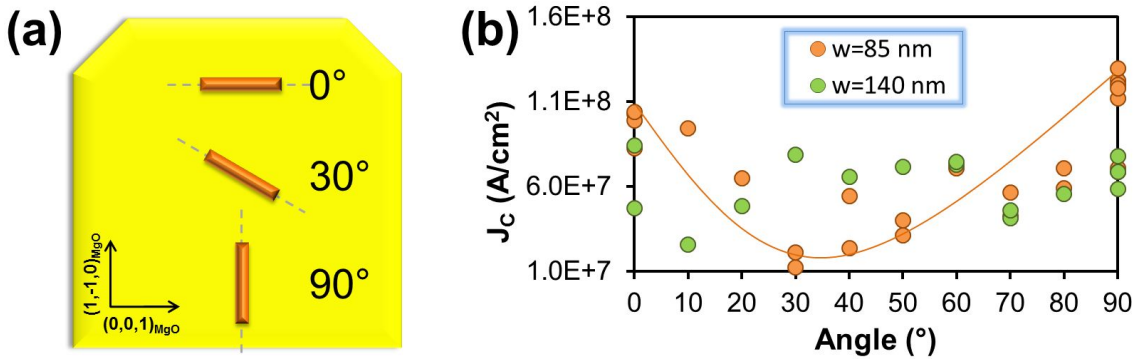

Figure 9.1: (a) Sketch of the nanowires, patterned at different in-plane angles with respect to the substrate. (b) Measured dependence of the critical current density J_C on the angle, both for the 85 nm and the 140 nm wide nanowires. The orange line is a guide for the eye.

Appendices

A

Recipes for sample fabrication

The recipes of the nanopatterning procedures presented here are tailored for the Nanofabrication Laboratory at the Department of Microtechnology and Nanoscience, Chalmers. As a consequence, the used parameters are specific of the equipment which are there.

A.1 YBCO nanowires on MgO (110)

1. A 50 nm thick film is deposited by Pulsed Laser deposition (DCA UHV system, tool #1142) on a MgO substrate (110) oriented, according to the parameters that are listed in Table 3.1.

2. A 50 nm thick film of Au is deposited by e-beam evaporation (Lesker#1, tool #451), at a rate of 1-2 Å/sec.

3. An 80 nm thick film of C is deposited by e-beam evaporation (AVAC HVC600, tool #420), at low rate (1 Å/sec). In order to improve the robustness of this layer, which has to act as a hard mask for YBCO during the following nanopatterning steps, the base pressure of the chamber is kept to its lowest possible value (1×10^{-7} mbar), also by using Ti pre-evaporation. The C evaporation is splitted in several steps, so to keep the process pressure constantly below 5×10^{-6} mbar.

4. The C surface is ashed 5 sec by using a low-power O_2 plasma (BatchTop, tools #418 - #419), to improve adhesion with the upcoming resist.

5. A double layer resist is spun on the chip. Both the bottom resist layer, MMA co-polymer, EL4 (4% solid in Ethyl lactate), and the top resist layer, ZEP520A 1:2, are spin-coated at 6000 RPM for 50 nm, than baked for 8 mins at 100° on a hotplate. Alternatively, a single layer resist can be used. In this case, a layer of ZEP 520A 1:1 is spin-coated at 4000 RPM for 120 nm, than baked for 5 mins at 105° on a hotplate.

6. The desired pattern in CAD file is exposed with e-beam litography at 100 kV. For small structures, a beam current of 2 nA, with a dose of 150 μC/cm^2 and

corrections to proximity effects, is used. For big structures (e.g. electrodes, bonding pads), a beam current of 35 nA, with a dose of 250 μC/cm^2 is used.

7. In case of double layer resist: the top layer resist is developed in Hexylacetate for 25-30 sec, rinsed in isopropyl alcohol (IPA) and blown dry with N_2, while the bottom resist is developed in HBIK:IPA 1:3 for 35-40 sec, rinsed in IPA and blown dry with N_2. In case of single layer resist: the ZEP 520A 1:1 is developed in Hexylacetate for 25-30 sec, rinsed in IPA and blown dry with N_2.

8. A fast descum process is carried in an O_2 plasma, e.g. "ash 5s", in the Batchtop (tools #418 - #419).

9. A thin layer (12 - 15 nm) of Cr is evaporated (in Lesker#1, tool #451), at a rate of 1 Å/sec.

10. Lift-off of Cr is done in Removal 1165 at 60°.

11. Unprotected carbon is removed by O_2 plasma etching in the Batchtop (tool #418), for 25 mins at 50 W, and pressure of 100 mTorr.

12. The YBCO and Au not covered by the C mask are very softly and slowly etched in the Ar^+ ion milling system (CAIBE Oxford Ionfab, tool #417). We have chosen to work close to the etching voltage threshold for YBCO: below this value, which is of the order of 300 V, the film is only made amorphous instead of being etched. Moreover we have used the lowest beam current which allows the ignition of the plasma in our milling system. A summary of all the used parameters is reported in the following table:

Parameter	Value
V_{beam}	300 V
I_{beam}	5 mA
Current density	0.06 A/cm^2
Tilt	5°
Base Pressure	1×10^{-7} mbar
Process Pressure	1.5 - 2.3 $\times 10^{-4}$ mbar
Ar^+ flow	3.9 sccm
Stage Rotation	ON
Neutralizer	OFF

With these parameters, the etching rates of the used materials are the following: 5 nm/min for Au, 7 Å/min for YBCO, 1.5 nm/min for MgO (110). As a consequence, $\approx$ 110 mins are needed to remove 50 nm of Au, 50 nm of YBCO and to overetch 50 nm into the MgO (110) substrate.

13. The remaining carbon is removed by means of a O_2 plasma etching in the Batchtop (tool #418), for 18-22 mins at 50 W, and pressure of 100 mTorr.

A.2 YBCO nanowires on LAO (001)

The procedure is the same as described in sec. (A.1), with the exception of the steps 1, 7 and 12, which are the following:

1. A 50 nm thick film is deposited by Pulsed Laser deposition (DCA UHV system, tool #1142) on a LAO substrate (001) oriented, according to the parameters that are listed in Table 3.1.

7. Both the ZEP 520A 1:2 used as a top layer in the double layer resist and the ZEP 520A 1:1 used as a single layer resist are developed in Hexylacetate for 10-12 sec, rinsed in IPA and blown dry with N_2.

12. With the parameters listed in the table above the etching rate of LAO is $\approx$ 10 nm/min. As a consequence, the etching time required to etch 50 nm of Au, 50 nm of YBCO and 50 nm of LAO (001) substrate is 90 mins.

A.3 YBCO/LSMO nanowires on LAO (001)

The procedure is the same as described in sec. (A.1), with the exception of the steps 1, 7 and 12. Moreover, an additional etching step is required in the end of the process.

1. A 50 nm thick film is deposited by Pulsed Laser deposition (DCA UHV system, tool #1142) on a LAO substrate (001) oriented, with the parameters that are listed in Table 3.1. On the top, a 15 nm thick film of LSMO is deposited by Pulsed Laser deposition (Calas System, tool #11411), with the parameters mentioned in sec. (3.5.2).

7. Both the ZEP 520A 1:2 used as a top layer in the double layer resist and the ZEP 520A 1:1 used as a single layer resist are developed in Hexylacetate for 10-12 sec, rinsed in IPA and blown dry with N_2.

12. With the parameters listed in the table of sec. (A.1), the etching rate of LSMO is $\approx$ 7 Å/min. As a consequence, the etching time required to etch 50 nm of Au, 15 nm of LSMO, 50 nm of YBCO and 50 nm of LAO (001) substrate is 115 mins.

14. The Au layer on the top of the nanostructures is removed by an additional ion milling step (CAIBE Oxford Ionfab, tool #417). The parameters are again those listed in the table of sec. (A.1), and the time to etch 50 nm of Au is $\approx$ 9 min.

B

The measurement setups

B.1 280 mK system - Heliox

The measurements in Chapters 5 and 6 were all done in an Oxford Heliox VL ^{3}He system, equipped with 44 dc-lines and used to reach temperatures down to 280 mK.

The 5×5 mm^2 chip is glued to a sample holder. Large Au/YBCO pads (250×75 μm^2) are located at the end of the electrodes, connected to the nanodevices. These pads are connected to the contacts of the sample holder by wedge bondings, using a gold wire of 25 μm diameter.

To cool down the nanodevices, the chip is mounted in thermal contact with the ^{3}He pot, located inside a vacuum can of the dip-stick. Then, the dip-stick is inserted in a liquid ^{4}He dewar surrounded by a superconducting magnetic shield. In this way, the chip reaches a temperature of 4.2 K. After this, a temperature of 1 K can be reached by pumping on the liquid ^{4}He contained in the so called 1 K pot. At this point, the charcoal ^{3}He sorb can be heated up with an electrical heater to release ^{3}He, and liquid ^{3}He condenses into the so called ^{3}He pot. Finally, pumping on this liquid with the charcoal absorption pump the cryostat can reach 280 mK.

All the nanodevices are low ohmic, with finite critical currents. As a consequence, measurements were performed in current bias mode. A high ohmic series resistance, R_b, is used to bias the device, while a resistor with lower resistance, R_s, is used to indirectly measure the current. The cryostat and the battery driven voltage preamplifiers are placed in an electromagnetic interference shielded room. All the digital electronics used for the measurements (voltage and current sources, analog to digital converters and the computer) is instead out of the shielded room, so to minimize the digital noise (see Fig. B.1). At the input-output of the matrix box, where the dc-lines are connected to the amplifiers and source, the signal is filtered by simple LC filters. The system is also equipped with a NbTi coil for the application of a magnetic field of around 100 mT. Moreover, a microwave antenna is mounted, close to the chip, to study microwave response of our nanodevices.

In details, the electronics used for the measurements was:

- 2 Stanford Research SR560 voltage preamplifiers.

- 2 HP 34401A multimeters.

- 1 Yokogawa 7651 dc current source, used to bias the NbTi coil.
- 1 Agilent 33220A arbitrary function generator, used for biasing.
- 1 Stanford Research Dynamic Signal analyzer SR785, used for the noise measurements.
- 1 National Instruments PCI-6052E data acquisition card (DAQ).

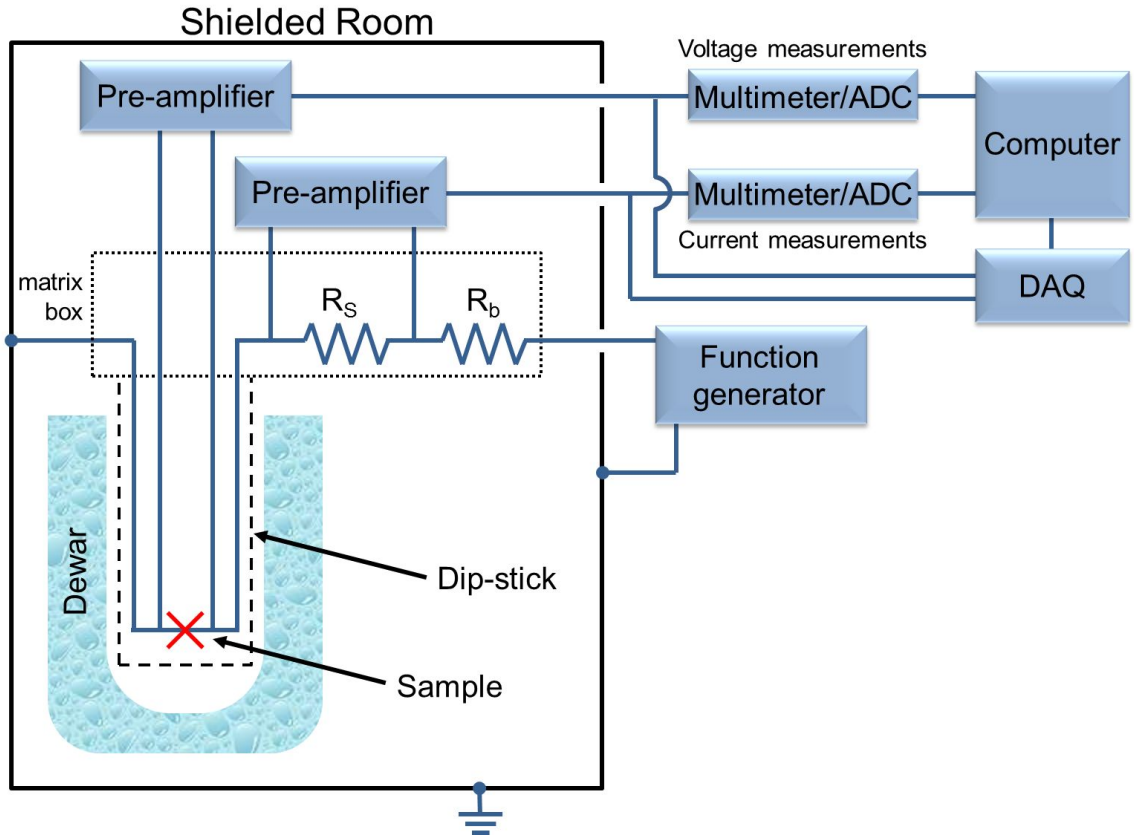

Figure B.1: A schematic diagram of the 300 mK Heliox measurement setup.

B.2 4.2 K system with optical access

The measurements in Chapters 8 were all done in a liquid helium flow cryostat with optical access, reaching temperatures down to 4.2 mK, which allows to perform photoresponse measurements.

The 5×5 mm^2 chip is glued to a sample holder. Large YBCO pads (250×75 μm^2) are located at the end of the electrodes, connected to the nanodevices. These pads are connected to the contacts of the sample holder by aluminum wedge bondings.

The sample holder is cooled down to 4.2 K through its mechanical attachment to a cold finger, which is cooled by using liquid ^{4}He. To cool down the cold finger,

a medium vacuum pressure ($p \leq 10^{-6}$ torr), reachable by diffusive pump, is required. Then, the liquid helium is transferred to the cryostat through a transfer tube, insulated at $p \leq 10^{-5}$ torr with respect environment, which is connected to the external liquid ^{4}He dewar. The flow is controlled by a spin valve.

Electric connections to the nanodevices were made through wire bonds to high bandwidth and low bandwidth cables going to room temperature. The low bandwidth connections were used to dc bias the nanodevices, while the output (photo)voltage signals were carried by the high bandwidth connection to two cascaded 1 GHz bandwidth amplifiers with an overall voltage gain of 400. The amplified signal was observed and recorded by using an oscilloscope (see Fig. B.2).

During the photoresponse measurements a diode laser with $\lambda = 1550$ nm characterized by low power (≈ 200 μW) and repetition rate of 10 MHz was used. The optical bench is also equipped with various 3 dB and 6 dB full-band-pass optical filters, used to attenuate the power of the laser before hitting the sample.

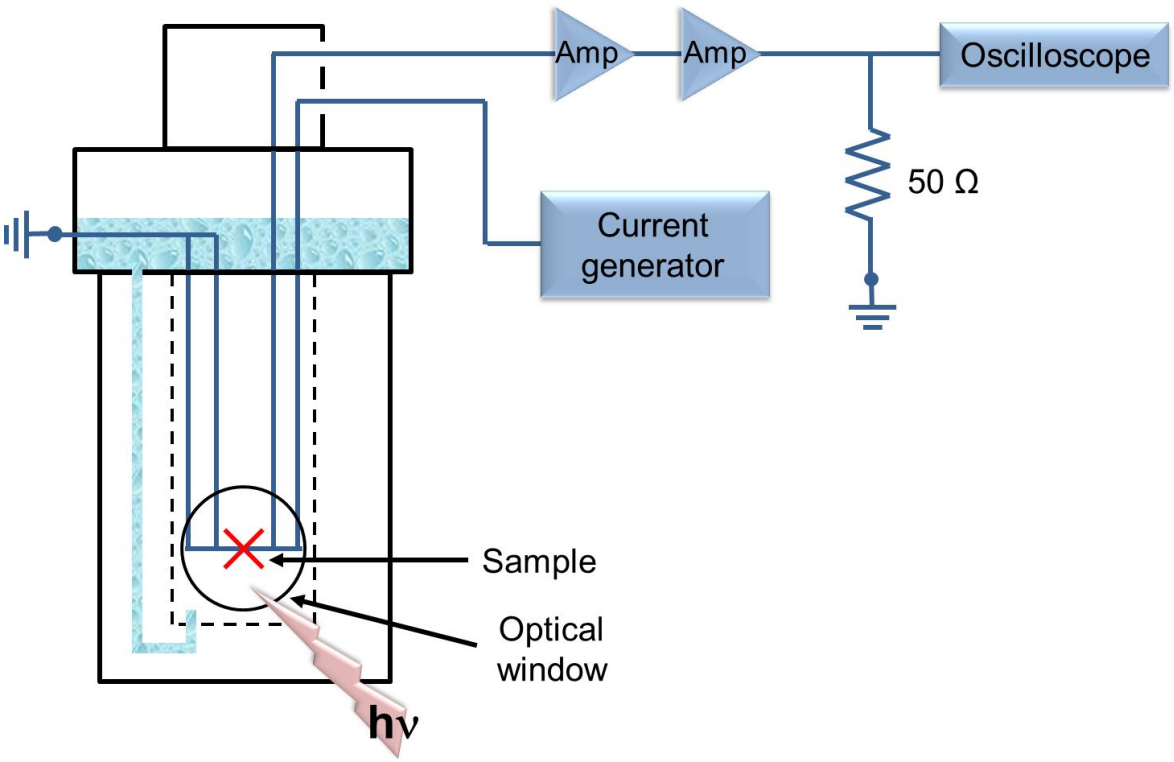

Figure B.2: A schematic diagram of the experimental apparatus used for the photoresponse experiments.

C

Determination of λ_0 and ξ_0 at temperatures close to T_C

In the Ginzburg-Landau (GL) approximation, the usual temperature dependences of the London penetration depth, coherence length and thermodynamical critical field write as:

$$\lambda_L(T) = \lambda_0^* \frac{1}{\sqrt{1 - \frac{T}{T_C}}} \tag{C.1}$$

$$\xi(T) = \xi_0^* \frac{1}{\sqrt{1 - \frac{T}{T_C}}} \tag{C.2}$$

$$B_C(T) = \frac{\Phi_0}{2\sqrt{2}\pi\, \xi_0^* \lambda_0^*} \left(1 - \frac{T}{T_C}\right) . \tag{C.3}$$

However the GL theory is strictly valid only at $T \approx T_C$. Therefore, the parameters ξ_0^* and λ_0^* do not correspond to the real zero temperature values, ξ_0 and λ_0.

To better estimate these latter two parameters, the starting point is that in the dirty limit the full temperature dependence of the depairing current density is well approximated by the GL expression (eq. 2.28) [201]: $J_C^{GL} \propto \left(\lambda_L^2(T)\, \xi(T)\right)^{-1}$.

Thence, considering the Bardeen expression for temperature dependence of J_C in the full temperature range below T_C, which we have experimentally observed in our nanowires

$$J_C(T) \propto \left[1 - \left(\frac{T}{T_C}\right)^2\right]^{\frac{3}{2}} , \tag{C.4}$$

and using the two fluid model for the expression of the temperature dependence of λ_L in the full temperature range below T_C,

$$\lambda_L(T) = \lambda_0 \frac{1}{\sqrt{1 - \left(\frac{T}{T_C}\right)^2}} , \tag{C.5}$$

we obtain for ξ:

$$\xi(T) \propto \frac{1}{\lambda_L^2 J_C} = \frac{1-\left(\frac{T}{T_C}\right)^2}{\left[1-\left(\frac{T}{T_C}\right)^2\right]^{\frac{3}{2}}} = \frac{1}{\sqrt{1-\left(\frac{T}{T_C}\right)^2}} \,. \tag{C.6}$$

The temperature dependence of ξ in the full temperature range can be written as:

$$\xi(T) = \xi_0 \frac{1}{\sqrt{1-\left(\frac{T}{T_C}\right)^2}} \,. \tag{C.7}$$

Similarly, we can write for B_C:

$$B_C(T) = \frac{\Phi_0}{2\sqrt{2}\pi\,\xi(T)\lambda_L(T)} = \frac{\Phi_0}{2\sqrt{2}\,\xi_0\lambda_0}\left[1-\left(\frac{T}{T_C}\right)^2\right] \,. \tag{C.8}$$

In the GL limit, at T close to T_C, we can approximate

$$\left(\frac{T}{T_C}\right)^2 \approx 1 + 2\left(\frac{T}{T_C}-1\right) = -1 + 2\,\frac{T}{T_C} \,. \tag{C.9}$$

From this it follows:

$$\lambda_L(T) \approx \frac{\lambda_0}{\sqrt{2}} \frac{1}{\sqrt{1-\frac{T}{T_C}}} \tag{C.10}$$

$$\xi(T) \approx \frac{\xi_0}{\sqrt{2}} \frac{1}{\sqrt{1-\frac{T}{T_C}}} \tag{C.11}$$

$$B_C(T) \approx \frac{\Phi_0}{\sqrt{2}\pi\,\xi_0\lambda_0}\left(1-\frac{T}{T_C}\right) \,. \tag{C.12}$$

Bibliography

[1] M. Zgirski, K.-P. Riikonen, V. Touboltsev, and K. Arutyunov, "Size Dependent Breakdown of Superconductivity in Ultranarrow Nanowires," *Nano Lett.* **5**, 1029 (2005).

[2] R. Vijay, J. D. Sau, M. L. Cohen, and I. Siddiqi, "Optimizing Anharmonicity in Nanoscale Weak Link Josephson Junction Oscillators," *Phys. Rev. Lett.* **103**, 087003 (2009).

[3] K. Arutyunov, T. T. Hongisto, J. S. Lehtinen, L. I. Leino, and A. L. Vasiliev, "Quantum phase slip phenomenon in ultra-narrow superconducting nanorings," *Sci. Rep.* **2**, 293 (2012).

[4] O. V. Astafiev, L. B. Ioffe, S. Kafanov, Y. A. Pashkin, K. Arutyunov, D. Shahar, O. Cohen, and J. S. Tsai, "Coherent quantum phase slip," *Nature* **484**, 355 (2012).

[5] T. Aref, A. Levchenko, V. Vakaryuk, and A. Bezryadin, "Quantitative analysis of quantum phase slips in superconducting MoGe nanowires revealed by switching-current statistics," *Phys. Rev. B* **86**, 024507 (2012).

[6] J. E. Mooij and Y. V. Nazarov, "Superconducting nanowires as quantum phase-slip junctions," *Nature Physics* **2**, 169 (2006).

[7] S. A. Kivelson, I. P. Bindloss, E. Fradkin, V. Oganesyan, J. M. Tranquada, A. Kapitulnik, and C. Howald, "How to detect fluctuating stripes in the high-temperature superconductors," *Rev. Mod. Phys.* **75**, 1201 (2003).

[8] A. A. Shanenko, M. D. Croitoru, M. Zgirski, F. M. Peeters, and K. Arutyunov, "Size-dependent enhancement of superconductivity in Al and Sn nanowires: shape-resonance effect," *Phys. Rev. B* **74**, 052502 (2006).

[9] F. M. Peeters, M. D. Croitoru, and A. A. Shanenko, "Nanowires and nanofilms: Superconductivity in quantum-size regime," *Physica C* **468**, 326 (2008).

[10] S. Bose, A. M. Garcia-Garcia, M. M. Ugeda, J. D. Urbina, C. H. Michaelis, I. Brihuega, and K. Kern, "Observation of shell effects in superconducting nanoparticles of Sn," *Nature Materials* **9**, 550 (2010).

[11] A. M. Garcia-Garcia, J. D. Urbina, E. A. Yuzbashyan, K. Richter, and B. L. Altshuler, "Bardeen-Cooper-Schrieffer Theory of Finite-Size Superconducting Metallic Grains," *Phys. Rev. Lett.* **100**, 187001 (2008).

[12] T. Senthil and M. P. A. Fisher, "Fractionalization in the Cuprates: Detecting the Topological Order," *Phys. Rev. Lett.* **86**, 292 (2001).

[13] D. A. Bonn, J. C. Wynn, B. W. Gardner, Y. J. Lin, R. Liang, W. N. Hardy, J. R. Kirtley, and K. A. Moler, "A limit on spin-charge separation in high-Tc superconductors from the absence of a vortex-memory effect," *Nature* **414**, 887 (2001).

[14] G. Deutscher, "Coherence and single-particle excitations in the high-temperature superconductors," *Nature* **397**, 410 (1999).

[15] Y. Uemura, "Bose-Einstein to BCS crossover picture for high-Tc cuprates," *Physica C* **282**, 194 (1997).

[16] K. K. Likharev, "Vortex motion and Josephson effect in superconducting thin bridges," *Sov. Phys. JETP* **34**, 906 (1972).

[17] L. G. Aslamazov and S. V. Lempitskii, "Resistive state in broad superconducting films," *Sov. Phys. JETP* **57**, 1291 (1983).

[18] G. Papari, F. Carillo, D. Stornaiuolo, L. Longobardi, F. Beltram, and F. Tafuri, "High critical-current density and scaling of phase-slip processes in YBCO nanowires," *Supercond. Sci. Technol.* **25**, 035011 (2012).

[19] J. A. Bonetti, D. S. Caplan, D. J. Van Harlingen, and M. B. Weissman, "Electronic Transport in Underdoped YBCO Nanowires: Evidence for Fluctuating Domain Structures," *Phys. Rev. Lett.* **93**, 087002 (2008).

[20] P. Larsson, B. Nilsson, and Z. G. Ivanov, "Fabrication and Transport Measurements of YBCO nanostructures," *J. Vac. Sci. Technol. B* **18**, 25 (2000).

[21] J. Schneider, H. Kohlstedt, and R. Wordenweber, "Nanobridges of optimized YBCO thin films for superconducting flux-flow type devices," *Appl. Phys. Lett.* **63**, 2426 (1993).

[22] H. Assink, A. J. M. Harg, C. M. Schep, N. Y. Chen, D. Marel, P. Hadley, E. W. J. M. Drift, and J. E. Mooij, "Critical Currents in submicron YBCO lines," *IEEE Trans. Appl. Supercond.* **3**, 2983 (1993).

[23] S. K. H. Lam and D. L. Tilbrook, "Development of a niobium nanosuperconducting quantum interference device for the detection of small spin populations," *Appl. Phys. Lett.* **82**, 1078 (2003).

[24] L. Hao, J. C. Macfarlane, J. C. Gallop, D. Cox, J. Beyer, D. Drung, and T. Schurig, "Measurement and noise performance of nano-superconducting-quantum-interference devices fabricated by focused ion beam," *Appl. Phys. Lett.* **92**, 192507 (2008).

[25] J. Gallop, "SQUIDs: some limits to measurement," *Supercond. Sci. Technol.* **16**, 1575 (2003).

[26] C. P. Foley and H. Hilgenkamp, "Why NanoSQUIDs are important: an introduction to the focus issue," *Supercond. Sci. Technol.* **22**, 064001 (2009).

[27] J. Schneider, M. Muck, and R. Wordenweber, "dc SQUIDs based upon $YBa_2Cu_3O_7$ nanobridges," *Appl. Phys. Lett.* **65**, 2475 (1994).

[28] M. V. Pedyash, D. H. A. Blank, and H. Rogalla, "Superconducting quantum interference devices based on YBaCuO nanobridges," *Appl. Phys. Lett.* **68**, 1156 (1996).

[29] F. Carillo, G. Papari, D. Stornaiuolo, D. Born, D. Montemurro, P. Pingue, F. Beltram, and F. Tafuri, "Little-Parks effect in single nanoscale YBCO rings," *Phys. Rev. B* **81**, 054505 (2010).

[30] V. Juričić, I. F. Herbut, and Z. Tešanović, "Restoration of the Magnetic hc/e Periodicity in Unconventional Superconductors," *Phys. Rev. Lett.* **100**, 187006 (2008).

[31] F. Loder, A. P. Kampf, T. Kopp, J. Mannhart, C. W. Schneider, and Y. S. Barash, "Magnetic flux periodicity of h/e in superconducting loops," *Nature Physics* **4**, 112 (2008).

[32] V. Vakaryuk, "Universal Mechanism for Breaking the hc/2e Periodicity of Flux-Induced Oscillations in Small Superconducting Rings," *Phys. Rev. Lett.* **101**, 167002 (2008).

[33] E. Berg, E. Fradkin, and S. A. Kivelson, "Charge-4e superconductivity from pair-density-wave order in certain high-temperature superconductors," *Nature Physics* **5**, 830 (2009).

[34] C. M. Natarajan, M. G. Tanner, and R. H. Hadfield, "Superconducting nanowire single-photon detectors: physics and applications," *Supercond. Sci. Technol.* **25**, 063001 (2012).

[35] H. Kamerlingh Onnes, "The resistance of pure mercury at helium temperatures," *Commun. Phys. Lab. Univ. Leiden* **12**, 120 (1911).

[36] W. Meissner and R. Ochsenfeld, "Ein neuer Effekt bei Eintritt der Supraleitfähigkeit," *Naturwissenschaften* **21**, 787 (1933).

[37] F. London and H. London, "The Electromagnetic Equations of the Supraconductor," *Proceedings of the Royal Society A: Mathematical, Physical and Engineering Sciences* **149**, 71 (1935).

[38] V. L. Ginzburg and L. D. Landau, *Zh. Eksp. Teor. Fiz.* **20**, 1064 (1950).

[39] M. Tinkham, *Introduction to Superconductivity* (Dover Publications, 2004).

[40] K. F. Herzfeld, E. Maxwell, and R. B. Scott, "Isotope Effect and Lattice Properties in Superconductivity," *Phys. Rev.* **79**, 911 (1950).

[41] J. Bardeen, L. N. Cooper, and J. R. Schrieffer, *Phys. Rev.* **108**, 1175 (1957).

[42] J. Orenstein and A. J. Millis, "Advances in the physics of high temperature superconductivity," *Science* **288**, 468 (2000).

[43] J. Bednorz and K. Müller, "Possible high-Tc superconductivity in the Ba-La-Cu-O system," *Zeitschrift für Physik B Condensed Matter* **64**, 189 (1986).

[44] M. K. Wu, J. R. Ashburn, C. J. Torng, P. H. Hor, R. L. Meng, L. Gao, Z. J. Huang, Y. Q. Wang, and C. W. Chu, "Superconductivity at 93 K in a new mixed-phase Y-Ba-Cu-O compound system at ambient pressure," *Phys. Rev. Lett.* **58**, 908 (1987).

[45] A. Schilling, M. Cantoni, J. D. Guo, and H. R. Ott, "Superconductivity above 130 K in the Hg-Ba-Ca-Cu-O system," *Nature* **363**, 56 (1993).

[46] Y. Tokura and T. Arima, "New Classification Method for Layered Copper Oxide Compounds and Its Application to Design of New High T_c Superconductors," *Jpn. J. Appl. Phys.* **29**, 2388 (1990).

[47] Y. Sassa, "ARPES investigations on in situ PLD grown $YBa_2Cu_3O_{7-\delta}$," *PhD thesis* (2011).

[48] T. A. Zaleski and T. K. Kopeć, "Possible origin of 60-K plateau in the $YBa_2Cu_3O_{6+y}$ phase diagram," *Phys. Rev. B* **74**, 014504 (2006).

[49] W. E. Pickett, "Electronic structure of the high-temperature oxide superconductors," *Rev. Mod. Phys.* **61**, 433 (1989).

[50] J. Brooks and J. Schrieffer, *Handbook of High -Temperature Superconductivity: Theory and Experiment* (Springer, 2007).

[51] M. D. Vázquez-Navarro, A. Kursumovic, and J. E. Evetts, "Study and modelling of oxygen diffusion in YBCO under isothermal conditions," *Supercond. Sci. Technol.* **12**, 1117 (1999).

[52] R. Cava, A. Hewat, E. Hewat, B. Batlogg, M. Marezio, K. Rabe, J. Krajewski, W. Peck Jr, and L. Rupp Jr, "Structural anomalies, oxygen ordering and superconductivity in oxygen deficient $Ba_2YCu_3O_x$," *Physica C* **165**, 419 (1990).

[53] N. Doiron-Leyraud, C. Proust, D. LeBoeuf, J. Levallois, J.-B. Bonnemaison, R. Liang, D. Bonn, W. Hardy, and L. Taillefer, "Quantum oscillations and the Fermi surface in an underdoped high-Tc superconductor," *Nature* **447**, 565 (2007).

[54] J. M. Tranquada, D. E. Cox, W. Kunnmann, H. Moudden, G. Shirane, M. Suenaga, P. Zolliker, D. Vaknin, S. K. Sinha, M. S. Alvarez, A. J. Jacobson, and D. C. Johnston, "Neutron-Diffraction Determination of Antiferromagnetic Structure of Cu Ions in $YBa_2Cu_3O_{6+x}$ with $x = 0.0$ and 0.15," *Phys. Rev. Lett.* **60**, 156 (1988).

[55] S. Nakamae, K. Behnia, N. Mangkorntong, M. Nohara, H. Takagi, S. J. C. Yates, and N. E. Hussey, "Electronic ground state of heavily overdoped nonsuperconducting $La_{2-x}Sr_xCuO_4$," *Phys. Rev. B* **68**, 100502 (2003).

[56] J. Chang, M. Månsson, S. Pailhès, T. Claesson, O. J. Lipscombe, S. M. Hayden, L. Patthey, O. Tjernberg, and J. Mesot, "Anisotropic breakdown of Fermi liquid quasiparticle excitations in overdoped $La_{2-x}Sr_xCuO_4$," *Nature Communications* **4**, 2559 (2013).

[57] C. M. Varma, P. B. Littlewood, S. Schmitt-Rink, E. Abrahams, and A. E. Ruckenstein, "Phenomenology of the normal state of Cu-O high-temperature superconductors," *Phys. Rev. Lett.* **63**, 1996 (1989).

[58] T. Timusk and B. Statt, "The pseudogap in high-temperature superconductors: an experimental survey," *Reports on Progress in Physics* **62**, 61 (1999).

[59] J. C. Campuzano, H. Ding, M. R. Norman, H. M. Fretwell, M. Randeria, A. Kaminski, J. Mesot, T. Takeuchi, T. Sato, T. Yokoya, T. Takahashi, T. Mochiku, K. Kadowaki, P. Guptasarma, D. G. Hinks, Z. Konstantinovic, Z. Z. Li, and H. Raffy, "Electronic Spectra and Their Relation to the $\pi-\pi$ Collective Mode in High- T_C Superconductors," *Phys. Rev. Lett.* **83**, 3709 (1999).

[60] S. Chakravarty, H.-Y. Kee, and V "An explanation for a universality of transition temperatures in families of copper oxide superconductors," *Nature* **428**, 53 (2004).

[61] R. Khasanov, T. Kondo, S. Strässle, D. O. G. Heron, A. Kaminski, H. Keller, S. L. Lee, and T. Takeuchi, "Evidence for a Competition between the Superconducting State and the Pseudogap State of $(BiPb)_2(SrLa)_2CuO_{6+\delta}$ from Muon Spin Rotation Experiments," *Phys. Rev. Lett.* **101**, 227002 (2008).

[62] V. J. Emery and S. A. Kivelson, "Importance of phase fluctuations in superconductors with small superfluid density," *Nature* **374**, 434 (1994).

[63] Y. Kohsaka, T. Hanaguri, M. Azuma, M. Takano, J. C. Davis, and H. Takagi, "Visualization of the emergence of the pseudogap state and the evolution to superconductivity in a lightly hole-doped Mott insulator," *Nature Phys.* **8**, 534 (2012).

[64] K. Segawa and Y. Ando, "Transport Anomalies and the Role of Pseudogap in the 60-K Phase of $YBa_2Cu_3O_{7-\delta}$," *Phys. Rev. Lett.* **86**, 4907 (2001).

[65] R. Beyers, B. Ahn, G. Gorman, V. Lee, S. Parkin, M. Ramirez, K. Roche, J. Vazquez, T. Gür, and R. Huggins, "Oxygen ordering, phase separation and the 60-K and 90-K plateaus in $YBa_2Cu_3O_x$," *Nature* **340**, 619 (1989).

[66] C. Chaillout, M. A. Alario-Franco, J. J. Capponi, J. Chenavas, J. L. Hodeau, and M. Marezio, "Oxygen-vacancy ordering in the $Ba_2YCu_3O_{7-x}$ $(0 \leq x \leq 1)$ superconducting system," *Phys. Rev. B* **36**, 7118 (1987).

[67] J. M. Tranquada, B. J. Sternlieb, J. D. Axe, Y. Nakamura, and S. Uchida, "Evidence for stripe correlations of spins and holes in copper oxide superconductors," *Nature* **375**, 561 (1995).

[68] J. Chang, E. Blackburn, A. Holmes, N. Christensen, J. Larsen, J. Mesot, R. Liang, D. Bonn, W. Hardy, A. Watenphul, M. v. Zimmermann, E. M. Forgan, and S. M. Hayden, "Direct observation of competition between superconductivity and charge density wave order in $YBa_2Cu_3O_{6.67}$," *Nature Physics* **8**, 871 (2012).

[69] J. Tallon, G. Williams, N. Flower, and C. Bernhard, "Phase separation, pseudogap and impurity scattering in the {HTS} cuprates," *Physica C* **282**, 236 (1997).

[70] D. N. Basov, R. Liang, D. A. Bonn, W. N. Hardy, B. Dabrowski, M. Quijada, D. B. Tanner, J. P. Rice, D. M. Ginsberg, and T. Timusk, "In-Plane Anisotropy of the Penetration Depth in $YBa_2Cu_3O_{7-x}$ and $YBa_2Cu_4O_8$ Superconductors," *Phys. Rev. Lett.* **74**, 598 (1995).

[71] S. T. Johnson, E. M. Forgan, S. H. Lloyd, C. M. Aegerter, S. L. Lee, R. Cubitt, P. G. Kealey, C. Ager, S. Tajima, A. Rykov, and D. M. Paul, "Flux-Line Lattice Structures in Untwinned $YBa_2Cu_3O_{7-\delta}$," *Phys. Rev. Lett.* **82**, 2792 (1999).

[72] C. Villard, G. Koren, D. Cohen, E. Polturak, B. Thrane, and D. Chateignier, "*ab*-Plane Anisotropy of Transport Properties in Unidirectionally Twinned $YBa_2Cu_3O_{7-\delta}$ Films," *Phys. Rev. Lett.* **77**, 3913 (1996).

[73] H. J. H. Smilde, A. A. Golubov, Ariando, G. Rijnders, J. M. Dekkers, S. Harkema, D. H. A. Blank, H. Rogalla, and H. Hilgenkamp, "Admixtures to *d*-Wave Gap Symmetry in Untwinned $YBa_2Cu_3O_7$ Superconducting Films Measured by Angle-Resolved Electron Tunneling," *Phys. Rev. Lett.* **95**, 257001 (2005).

[74] D. H. Lu, D. L. Feng, N. P. Armitage, K. M. Shen, A. Damascelli, C. Kim, F. Ronning, Z.-X. Shen, D. A. Bonn, R. Liang, W. N. Hardy, A. I. Rykov, and S. Tajima, "Superconducting Gap and Strong In-Plane Anisotropy in Untwinned $YBa_2Cu_3O_{7-\delta}$," *Phys. Rev. Lett.* **86**, 4370 (2001).

[75] J. Waldram, *Superconductivity of Metals and Cuprates* (Taylor & Francis, 1996).

[76] T. Sekitani, N. Miura, S. Ikeda, Y. Matsuda, and Y. Shiohara, "Upper critical field for optimally-doped $YBa_2Cu_3O_{7-\delta}$," *Phys. B: Condens. Matter* **346**, 319 (2004).

[77] D. J. Van Harlingen, "Phase-sensitive tests of the symmetry of the pairing state in the high-temperature superconductors - Evidence for $d_{x^2-y^2}$ symmetry," *Rev. Mod. Phys.* **67**, 515 (1995).

[78] D. Gustafsson, D. Golubev, M. Fogelström, T. Claeson, S. Kubatkin, T. Bauch, and F. Lombardi, "Fully gapped superconductivity in a nanometre-size $YBa_2Cu3O_{7-\delta}$ island enhanced by a magnetic field," *Nature Nanotechnol.* **8**, 25 (2013).

[79] A. V. Chubukov and D. K. Morr, "Electronic structure of underdoped cuprates," *Physics Reports* **288**, 355 (1997).

[80] J. Zaanen, S. Chakravarty, T. Senthil, P. Anderson, P. Lee, J. Schmalian, M. Imada, D. Pines, M. Randeria, C. M. Varma, M. Vojta, and M. Rice, "Towards a complete theory of High-T_C," *Nature Phys.* **2**, 138 (2006).

[81] J. M. Tranquada, G. D. Gu, M. Hücker, Q. Jie, H.-J. Kang, R. Klingeler, Q. Li, N. Tristan, J. S. Wen, G. Y. Xu, Z. J. Xu, J. Zhou, and M. v. Zimmermann, "Evidence for unusual superconducting correlations coexisting with stripe order in $La_{1.875}Ba_{0.125}CuO_4$," *Phys. Rev. B* **78**, 174529 (2008).

[82] C. V. Parker, P. Aynajian, E. H. d. Silva Neto, A. Pushp, S. Ono, J. Wen, Z. Xu, G. Gu, and A. Yazdani, "Fluctuating stripes at the onset of the pseudogap in the high-T_c superconductor $Bi_2Sr_2CaCu_2O_{8+x}$," *Nature* **468**, 677 (2010).

[83] R.-H. He, M. Hashimoto, H. Karapetyan, J. D. Koralek, J. P. Hinton, J. P. Testaud, V. Nathan, Y. Yoshida, H. Yao, K. Tanaka, W. Meevasana, R. G. Moore, D. H. Lu, S.-K. Mo, M. Ishikado, H. Eisaki, Z. Hussain, T. P. Devereaux, S. A. Kivelson, J. Orenstein, A. Kapitulnik, and Z.-X. Shen, "From a Single-Band Metal to a High-Temperature Superconductor via Two Thermal Phase Transitions," *Science* **331**, 1579 (2011).

[84] E. H. da Silva Neto, P. Aynajian, C. V. Parker, and A. Yazdani, "Detecting incipient stripe order in the high-temperature superconductor $Bi_2Sr_2CaCu_2O_{8+x}$," *Physica C* **481**, 153 (2012).

[85] K. A. Moler, "High-temperature superconductivity: How the cuprates hid their stripes," *Nature* **468**, 643 (2010).

[86] R. Doll and M. Näbauer, "Experimental Proof of Magnetic Flux Quantization in a Superconducting Ring," *Phys. Rev. Lett.* **7**, 51 (1961).

[87] B. S. Deaver and W. M. Fairbank, "Experimental Evidence for Quantized Flux in Superconducting Cylinders," *Phys. Rev. Lett.* **7**, 43 (1961).

[88] A. A. Abrikosov, "On the magnetic properties of the superconductors of the second group," *Sov. Phys. JETP* **5**, 1174 (1957).

[89] M. Tinkham, "Effect of Fluxoid Quantization on Transitions of Superconducting Films," *Phys. Rev.* **129**, 2413 (1963).

[90] W. A. Little and R. D. Parks, "Observation of Quantum Periodicity in the Transition Temperature of a Superconducting Cylinder," *Phys. Rev. Lett.* **9**, 9 (1962).

[91] B. Josephson, "Possible new effects in superconductive tunnelling," *Physics Letters* **1**, 251 (1962).

[92] P. W. Anderson and J. M. Rowell, "Probable Observation of the Josephson Superconducting Tunneling Effect," *Phys. Rev. Lett.* **10**, 230 (1963).

[93] K. K. Likharev and L. A. Yakobson, "Steady state properties of superconducting bridges," *Sov. Phys. Tech. Phys.* **20**, 950 (1976).

[94] K. K. Likharev, "Superconducting weak links," *Rev. Mod. Phys.* **51**, 101 (1979).

[95] D. Y. Vodolazov, I. Maksimov, and E. Brandt, "Modulation instability of the order parameter in thin-film superconductors with edge barrier," *Europhys. Lett.* **48**, 313 (1999).

[96] L. N. Bulaevskii, M. J. Graf, C. D. Batista, and V. G. Kogan, "Vortex-induced dissipation in narrow current-biased thin-film superconducting strips," *Phys. Rev. B* **83**, 144526 (2011).

[97] W. A. Little, "Decay of Persistent Currents in Small Superconductors," *Phys. Rev.* **156**, 396 (1967).

[98] J. S. Langer and V. Ambegaokar, "Intrinsic Resistive Transition in Narrow Superconducting Channels," *Phys. Rev.* **164**, 498 (1967).

[99] D. E. McCumber and B. I. Halperin, "Time Scale of Intrinsic Resistive Fluctuations in Thin Superconducting Wires," *Phys. Rev. B* **1**, 1054 (1970).

[100] M. Bell, A. Sergeev, V. Mitin, J. Bird, A. Verevkin, and G. Gol'tsman, "One-dimensional resistive states in quasi-two-dimensional superconductors: Experiment and theory," *Phys. Rev. B* **76**, 094521 (2007).

[101] N. Giordano, "Evidence for Macroscopic Quantum Tunneling in One-Dimensional Superconductors," *Phys. Rev. Lett.* **61**, 2137 (1988).

[102] A. Bezryadin, "Quantum suppression of superconductivity in nanowires," *J. Phys.: Condens. Matter* **20**, 043202 (2008).

[103] K. Arutyunov, D. Golubev, and A. Zaikin, "Superconductivity in one dimension," *Physics Reports* **464**, 1 (2008).

[104] D. S. Golubev and A. D. Zaikin, "Thermally activated phase slips in superconducting nanowires," *Phys. Rev. B* **78**, 144502 (2008).

[105] (To be published).

[106] G. N. Gol'tsman, O. Okunev, G. Chulkova, A. Lipatov, A. Semenov, K. Smirnov, B. Voronov, A. Dzardanov, C. Williams, and R. Sobolewski, "Picosecond superconducting single-photon optical detector," *Appl. Phys. Lett.* **79**, 705 (2001).

[107] H. Weinstock, *SQUID sensors: fundamentals, fabrication, and applications* (Springer, 1996).

[108] K. Hasselbach, D. Mailly, and J. R. Kirtley, "Micro-superconducting quantum interference device characteristics," *J. Appl. Phys.* **91** (2002).

[109] C. D. Tesche and J. Clarke, "dc SQUID: Noise and optimization," *J. Low Temp. Phys.* **29**, 301 (1977).

[110] T. Steinborn, G. Miehe, J. Wiesner, E. Brecht, H. Fuess, G. Wirth, B. Schulte, M. Speckmann, H. Adrian, M. Maul, K. Petersen, W. Blau, and M. McConnel, "Twinning of $YBa_2Cu_3O_7$ thin films on different substrates and modification by irradiation," *Physica C* **220**, 219 (1994).

[111] D. Schweitzer, T. Bollmeier, B. Stritzker, and B. Rauschenbach, "Twinning of $YBa_2Cu_3O_7$ thin films on different substrates," *Thin Solid Films* **280**, 147 (1996).

[112] W. K. Kwok, U. Welp, V. M. Vinokur, S. Fleshler, J. Downey, and G. W. Crabtree, "Direct observation of intrinsic pinning by layered structure in single-crystal $YBa_2Cu_3O_{7-\delta}$," *Phys. Rev. Lett.* **67**, 390 (1991).

[113] J. M. Dekkers, G. Rijnders, S. Harkema, H. J. H. Smilde, H. Hilgenkamp, H. Rogalla, and D. H. A. Blank, "Monocrystalline $YBa_2Cu_3O_{7-x}$ thin films on vicinal $SrTiO_3$ (001) substrates," *Appl. Phys. Lett.* **83**, 5199 (2003).

[114] S. Hoon Lee, J.-H. Choi, and S.-G. Lee, "Transition properties of a $YBa_2Cu_3O_7$ nanobridge patterned across a twin boundary of a $LaAlO_3$ substrate," *J. Appl. Phys.* **111**, 063914 (2012).

[115] A. P. Zhuravel, S. M. Anlage, S. K. Remillard, A. V. Lukashenko, and A. V. Ustinov, "Effect of $LaAlO_3$ twin-domain topology on local dc and microwave properties of cuprate films," *J. Appl. Phys.* **108**, 033920 (2010).

[116] J. Mazierska, D. Ledenyov, M. V. Jacob, and J. Krupka, "Precise microwave characterization of MgO substrates for HTS circuits with superconducting post dielectric resonator," *Supercond. Sci. Technol.* **18**, 18 (2005).

[117] A. Di Chiara, F. Lombardi, F. M. Granozio, U. S. di Uccio, M. Valentino, F. Tafuri, A. Del Vecchio, M. De Riccardis, and L. Tapfer, "Structure and morphology of MgO/YBCO bilayers for biepitaxial junctions," *Physica C* **273**, 30 (1996).

[118] G. Farnan, M. McCurry, and D. Walmsley, "Fabrication and characterisation of underdoped $YBa_2Cu_3O_{7-\delta}$ thin films," *Physica C* **341**, 2335 (2000).

[119] C. Namgung, J. Irvine, J. Binks, and A. West, "Orthorhombic-tetragonal transition in YBa_2Cu_3Ox," *Supercond. Sci. Technol.* **1**, 169 (1988).

[120] J. Ye and K. Nakamura, "Quantitative structure analyses of $YBa_2Cu_3O_{7-\delta}$ thin films: Determination of oxygen content from x-ray-diffraction patterns," *Phys. Rev. B* **48**, 7554 (1993).

[121] P. Benzi, E. Bottizzo, and N. Rizzi, "Oxygen determination from cell dimensions in YBCO superconductors," *J. Cryst. Growth* **269**, 625 (2004).

[122] A. I. Buzdin, "Proximity effects in superconductor-ferromagnet heterostructures," *Rev. Mod. Phys.* **77**, 935 (2005).

[123] L. Parlato, R. Arpaia, C. De Lisio, F. Miletto Granozio, G. P. Pepe, P. Perna, V. Pagliarulo, C. Bonavolontà, M. Radovic, Y. Wang, R. Sobolewski, and U. Scotti di Uccio, "Time-resolved optical response of all-oxide $YBa_2Cu_3O_7/La_{0.7}Sr_{0.3}MnO_3$ proximitized bilayers," *Phys. Rev. B* **87**, 134514 (2013).

[124] S. Soltan, J. Albrecht, and H.-U. Habermeier, "Ferromagnetic/superconducting bilayer structure: A model system for spin diffusion length estimation," *Phys. Rev. B* **70**, 144517 (2004).

[125] C. Chen, Y. Li, and C. Cai, "Field-suppressed interfacial spin scattering in $YBa_2Cu_3O_{7-\delta}/La_{0.67}Sr_{0.33}MnO_3$ heterostructures," *Solid State Commun.* **152**, 1203 (2012).

[126] S. Ki and J. Dho, "Interface Reaction and Thickness-dependent Spin-diffusion Effect in $YBa_2Cu_3O_{7-\delta}/La_{0.7}Sr_{0.3}MnO_3$ Bilayers," *J. Korean Phys. Soc.* **57**, 1879 (2010).

[127] C. H. Wu, Y. T. Chou, W. C. Kuo, J. H. Chen, L. M. Wang, J. C. Chen, K. L. Chen, U. C. Sou, H. C. Yang, and J. T. Jeng, "Fabrication and characterization of high-T_C $YBa_2Cu_3O_{7-x}$ nanoSQUIDs made by focused ion beam milling," *Nanotechnology* **19**, 315304 (2008).

[128] N. Curtz, E. Koller, H. Zbinden, M. Decroux, L. Antognazza, Ø. Fischer, and N. Gisin, "Patterning of ultrathin YBCO nanowires using a new focused-ion-beam process," *Supercond. Sci. Technol.* **23**, 045015 (2010).

[129] G. Zhang, X. Lu, T. Zhang, J. Qu, W. Wang, X. Li, and S. Yu, "Microstructure and superconductivity of highly ordered $YBa_2Cu_3O_{7-\delta}$ nanowire arrays," *Nanotechnology* **17**, 4252 (2006).

[130] A. I. Mansour, K. H. Chow, and J. Jung, "Persistent critical current of $YBa_2Cu_3O_{7-\delta}$ nanowires," *J. Appl. Phys.* **110**, 063909 (2011).

[131] P. Morales, M. DiCiano, and J. Y. T. Wei, "Selective epitaxial growth of submicron complex oxide structures by amorphous $SrTiO_3$," *Appl. Phys. Lett.* **86**, 192509 (2005).

[132] A. A. O. Elkaseh, W. J. Perold, and V. V. Srinivasu, "Josephson nanoconstrictions made by AFM plowing of $YBa_2Cu_3O_{7-x}$ films," *J. Appl. Phys.* **108**, 053914 (2010).

[133] K. Xu and J. R. Heath, "Long, Highly-Ordered High-Temperature Superconductor Nanowire Arrays," *Nano Lett.* **8**, 3845 (2008).

[134] K. Kajino, T. Kimura, Y. Horii, M. Watanabe, M. Inoue, and A. Fujimaki, "Preparation of Narrowed $YBa_2Cu_3O_{7-x}$ Nanobridges Down to 30 nm With Reduced Degradation," *IEEE Trans. Appl. Supercond.* **19**, 178 (2009).

[135] G. Papari, F. Carillo, D. Born, L. Bartoloni, E. Gambale, D. Stornaiuolo, P. Pingue, F. Beltram, and F. Tafuri, "YBCO Nanobridges: Simplified Fabrication Process by Using a Ti Hard Mask," *IEEE Trans. Appl. Supercond.* **19**, 183 (2009).

[136] R. Arpaia, S. Nawaz, F. Lombardi, and T. Bauch, "Improved Nanopatterning for YBCO Nanowires Approaching the Depairing Current," *IEEE Trans. Appl. Supercond.* **23**, 1101505 (2013).

[137] S. Nawaz, R. Arpaia, F. Lombardi, and T. Bauch, "Microwave Response of Superconducting $YBa_2Cu_3O_{7-\delta}$ Nanowire Bridges Sustaining the Critical Depairing Current: Evidence of Josephson-like Behavior," *Phys. Rev. Lett.* **110**, 167004 (2013).

[138] S. Nawaz, R. Arpaia, T. Bauch, and F. Lombardi, "Approaching the theoretical depairing current in $YBa_2Cu_3O_{7-x}$ nanowires," *Physica C* **495**, 33 (2013).

[139] S. Tahara, S. M. Anlage, J. Halbritter, C.-B. Eom, D. K. Fork, T. H. Geballe, and M. R. Beasley, "Critical currents, pinning, and edge barriers in narrow $YBa_2Cu_3O_{7-\delta}$ thin films," *Phys. Rev. B* **41**, 11203 (1990).

[140] M. Flik and C. Tien, "Size effect on the thermal conductivity of high-Tc thin-film superconductors," *J. Heat Transfer* **112**, 872 (1990).

[141] P. Mikheenko, X. Deng, S. Gildert, M. S. Colclough, R. A. Smith, C. M. Muirhead, P. D. Prewett, and J. Teng, "Phase slips in submicrometer $YBa_2Cu_3O_{7-\delta}$ bridges," *Phys. Rev. B* **72**, 174506 (2005).

[142] M. Pedyash, G. Gerritsma, D. Blank, and H. Rogalla, "Coherent vortex motion in superconducting nanobridges based on YBaCuO thin films," *IEEE Trans. Appl. Supercond.* **5**, 1387 (1995).

[143] J. Bardeen, "Critical Fields and Currents in Superconductors," *Rev. Mod. Phys.* **34**, 667 (1962).

[144] A. G. Zaitsev, R. Schneider, G. Linker, F. Ratzel, R. Smithey, P. Schweiss, J. Geerk, R. Schwab, and R. Heidinger, "Microwave measurements of the absolute London penetration depth in double-sided $YBa_2Cu_3O_{7-x}$ thin films on sapphire," *Rev. Sci. Instrum.* **73**, 335 (2002).

[145] *http://www.ceraco.de/* .

[146] J. R. Clem and K. K. Berggren, "Geometry-dependent critical currents in superconducting nanocircuits," *Phys. Rev. B* **84**, 174510 (2011).

[147] D. Henrich, P. Reichensperger, M. Hofherr, J. M. Meckbach, K. Il'in, M. Siegel, A. Semenov, A. Zotova, and D. Y. Vodolazov, "Geometry-induced reduction of the critical current in superconducting nanowires," *Phys. Rev. B* **86**, 144504 (2012).

[148] H. L. Hortensius, E. F. C. Driessen, T. M. Klapwijk, K. K. Berggren, and J. R. Clem, "Critical-current reduction in thin superconducting wires due to current crowding," *Appl. Phys. Lett.* **100**, 182602 (2012).

[149] M. M. J. Khapaev, "Extraction of inductances of plane thin film superconducting circuits," *Supercond. Sci. Technol.* **10**, 389 (1997).

[150] M. Y. Kupriyanov and V. F. Lukichev, *Fiz. Nizk. Temp.* **6**, 445 (1980).

[151] M. W. Brenner, S. Gopalakrishnan, J. Ku, T. J. McArdle, J. N. Eckstein, N. Shah, P. M. Goldbart, and A. Bezryadin, "Cratered Lorentzian response of driven microwave superconducting nanowire-bridged resonators: Oscillatory and magnetic-field induced stochastic states," *Phys. Rev. B* **83**, 184503 (2011).

[152] M. W. Brenner, D. Roy, N. Shah, and A. Bezryadin, "Dynamics of superconducting nanowires shunted with an external resistor," *Phys. Rev. B* **85**, 224507 (2012).

[153] S. Shapiro, "Josephson Currents in Superconducting Tunneling: The Effect of Microwaves and Other Observations," *Phys. Rev. Lett.* **11**, 80 (1963).

[154] M.-H. Bae, R. C. Dinsmore III, T. Aref, M. Brenner, and A. Bezryadin, "Current-Phase Relationship, Thermal and Quantum Phase Slips in Superconducting Nanowires Made on a Scaffold Created Using Adhesive Tape," *Nano Lett.* **9**, 1889 (2009).

[155] M. R. Beasley, J. E. Mooij, and T. P. Orlando, "Possibility of Vortex-Antivortex Pair Dissociation in Two-Dimensional Superconductors," *Phys. Rev. Lett.* **42**, 1165 (1979).

[156] D. Gustafsson, F. Lombardi, and T. Bauch, "Noise properties of nanoscale $YBa_2Cu_3O_{7-\delta}$ Josephson junctions," *Phys. Rev. B* **84**, 184526 (2011).

[157] D. S. Hopkins, D. Pekker, P. M. Goldbart, and A. Bezryadin, "Quantum Interference Device Made by DNA Templating of Superconducting Nanowires," *Science* **308**, 1762 (2005).

[158] C. Granata, E. Esposito, A. Vettoliere, L. Petti, and M. Russo, "An integrated superconductive magnetic nanosensor for high-sensitivity nanoscale applications," *Nanotechnology* **19**, 275501 (2008).

[159] R. Vijay, E. M. Levenson-Falk, D. H. Slichter, and I. Siddiqi, "Approaching ideal weak link behavior with three dimensional aluminum nanobridges," *Appl. Phys. Lett.* **96**, 223112 (2010).

[160] M. V. Pedyash, D. H. Blank, J. De Muijnck, and H. Rogalla, "Properties of YBaCuO nanobridges and dc-SQUIDs," *IEEE Trans. Appl. Supercond.* **7**, 2764 (1997).

[161] R. Arpaia, M. Arzeo, S. Nawaz, S. Charpentier, F. Lombardi, and T. Bauch, "Ultra low noise $YBa_2Cu_3O_{7-\delta}$ nano superconducting quantum interference devices implementing nanowires," *Appl. Phys. Lett.* **104**, 072603 (2014).

[162] I. Sochnikov, A. Shaulov, Y. Yeshurun, G. Logvenov, and I. Bozovic, "Large oscillations of the magnetoresistance in nanopatterned high-temperature superconducting films," *Nature Nanotechnology* **5**, 516 (2010).

[163] G. J. Podd, G. D. Hutchinson, D. A. Williams, and D. G. Hasko, "Micro-SQUIDs with controllable asymmetry via hot-phonon controlled junctions," *Phys. Rev. B* **75**, 134501 (2007).

[164] P. A. Rosenthal, M. R. Beasley, K. Char, M. S. Colclough, and G. Zaharchuk, "Flux focusing effects in planar thin film grain boundary Josephson junctions," *Appl. Phys. Lett.* **59**, 3482 (1991).

[165] J. R. Clem and E. H. Brandt, "Response of thin-film SQUIDs to applied fields and vortex fields: Linear SQUIDs," *Phys. Rev. B* **72**, 174511 (2005).

[166] M. Sampietro, L. Fasoli, and G. Ferrari, "Spectrum analyzer with noise reduction by cross-correlation technique on two channels," *Rev. Sci. Instrum.* **70**, 2520 (1999).

[167] T. Schwarz, J. Nagel, R. Wölbing, M. Kemmler, R. Kleiner, and D. Koelle, "Low-Noise Nano Superconducting Quantum Interference Device Operating in Tesla Magnetic Fields," *ACS Nano* **7**, 844 (2013).

[168] J. Nagel, K. B. Konovalenko, M. Kemmler, M. Turad, R. Werner, E. Kleisz, S. Menzel, R. Klingeler, B. Büchner, R. Kleiner, and D. Koelle, "Resistively shunted $YBa_2Cu_3O_7$ grain boundary junctions and low-noise SQUIDs patterned by a focused ion beam down to 80 nm linewidth," *Supercond. Sci. Technol.* **24**, 015015 (2011).

[169] D. Drung, "High-T_c and low-T_c dc SQUID electronics," *Supercond. Sci. Technol.* **16**, 1320 (2003).

[170] D. Drung, "Low frequency noise in low Tc multiloop magnetometers with additional positive feedback," *Appl. Phys. Lett.* **67**, 1474 (1995).

[171] T.-C. Wei and P. M. Goldbart, "Emergence of h/e-period oscillations in the critical temperature of small superconducting rings threaded by magnetic flux," *Phys. Rev. B* **77**, 224512 (2008).

[172] J.-X. Zhu and H. T. Quan, "Magnetic flux periodicity in a hollow d-wave superconducting cylinder," *Phys. Rev. B* **81**, 054521 (2010).

[173] R. P. Groff and R. D. Parks, "Fluxoid Quantization and Field-Induced Depairing in a Hollow Superconducting Microcylinder," *Phys. Rev.* **176**, 567 (1968).

[174] N. Bluzer, "Temporal relaxation of nonequilibrium in Y-Ba-Cu-O measured from transient photoimpedance response," *Phys. Rev. B* **44**, 10222 (1991).

[175] A. D. Semenov, G. N. Gol'tsman, I. G. Gogidze, A. V. Sergeev, E. M. Gershenzon, P. T. Lang, and K. F. Renk, "Subnanosecond photoresponse of a YBaCuO thin film to infrared and visible radiation by quasiparticle induced suppression of superconductivity," *Appl. Phys. Lett.* **60**, 903 (1992).

[176] M. Lindgren, M. Zorin, V. Trifonov, M. Danerud, D. Winkler, B. Karasik, G. Gol'tsman, and E. Gershenzon, "Optical mixing in a patterned $YBa_2Cu_3O_{7-\delta}$ thin film," *Appl. Phys. Lett.* **65**, 3398 (1994).

[177] M. Leung, P. R. Broussard, J. H. Claassen, M. Osofsky, S. A. Wolf, and U. Strom, "Optical detection in thin granular films of YBCO at temperatures between 4.2 and 100 K," *Appl. Phys. Lett.* **51**, 2046 (1987).

[178] N. Bluzer, "Biexponential decay and delay artifact in the photoresponse of superconductors," *IEEE Trans. Appl. Supercond.* **3**, 2869 (1993).

[179] A. Frenkerl, "High temperature superconducting thin films as broadband optical detectors," *Physica C* **180**, 251 (1991).

[180] J. M. Chwalek, C. Uher, J. F. Whitaker, G. A. Mourou, J. Agostinelli, and M. Lelental, "Femtosecond optical absorption studies of nonequilibrium electronic processes in high Tc superconductors," *Appl. Phys. Lett.* **57**, 1696 (1990).

[181] S. N. Dorenbos, E. M. Reiger, U. Perinetti, V. Zwiller, T. Zijlstra, and T. M. Klapwijk, "Low noise superconducting single photon detectors on silicon," *Appl. Phys. Lett.* **93**, 131101 (2008).

[182] F. Marsili, V. B. Verma, J. A. Stern, S. Harrington, A. E. Lita, T. Gerrits, I. Vayshenker, B. Baek, M. D. Shaw, R. P. Mirin, and S. W. Nam, "Detecting single infrared photons with 93% system efficiency," *Nature Photonics* **7**, 210 (2013).

[183] R. Arpaia, M. Ejrnaes, L. Parlato, R. Cristiano, M. Arzeo, T. Bauch, S. Nawaz, F. Tafuri, G. P. Pepe, and F. Lombardi, "Highly homogeneous YBCO/LSMO nanowires for photoresponse experiments," *Supercond. Sci. Technol.* **27**, 044027 (2014).

[184] A. V. Gurevich and R. G. Mints, "Self-heating in normal metals and superconductors," *Rev. Mod. Phys.* **59**, 941 (1987).

[185] M. Ejrnaes, A. Casaburi, O. Quaranta, S. Marchetti, A. Gaggero, F. Mattioli, R. Leoni, S. Pagano, and R. Cristiano, "Characterization of parallel superconducting nanowire single photon detectors," *Supercond. Sci. Technol.* **22**, 055006 (2009).

[186] F. Mattioli, M. Ejrnaes, A. Gaggero, A. Casaburi, R. Cristiano, S. Pagano, and R. Leoni, "Large area single photon detectors based on parallel configuration NbN nanowires," *J. Vac. Sci. Technol., B* **30**, 031204 (2012).

[187] N. Marrocco, G. P. Pepe, A. Capretti, L. Parlato, V. Pagliarulo, G. Peluso, A. Barone, R. Cristiano, M. Ejrnaes, A. Casaburi, N. Kashiwazaki, T. Taino, H. Myoren, and R. Sobolewski, "Strong critical current density enhancement in NiCu/NbN superconducting nanostripes for optical detection," *Appl. Phys. Lett.* **97**, 092504 (2010).

[188] P. Przyslupski, I. Komissarov, W. Paszkowicz, P. Dluzewski, R. Minikayev, and M. Sawicki, "Magnetic properties of $La_{0.67}Sr_{0.33}MnO_3$-$YBa_2Cu_3O_7$ superlattices," *Phys. Rev. B* **69**, 134428 (2004).

[189] J. T. Petrisor, M. S. Gabor, C. Tiusan, V. Galluzzi, G. Celentano, S. Popa, A. Boulle, and T. Petrisor, "Magnetic pinning effects of epitaxial $La_xSr_{1-x}MnO_3$ nanostructured thin films on $YBa_2Cu_3O_{7-\delta}$ layers," *J. Appl. Phys.* **112**, 053919 (2012).

[190] T. Aytug, M. Paranthaman, B. W. Kang, S. Sathyamurthy, A. Goyal, and D. K. Christen, "$La_{0.7}Sr_{0.3}MnO_3$: A single, conductive-oxide buffer layer for the development of $YBa_2Cu_3O_{7-\delta}$ coated conductors," *Appl. Phys. Lett.* **79**, 2205 (2001).

[191] A. K. Elmurodov, F. M. Peeters, D. Y. Vodolazov, S. Michotte, S. Adam, F. d. M. de Horne, L. Piraux, D. Lucot, and D. Mailly, "Phase-slip phenomena in NbN superconducting nanowires with leads," *Phys. Rev. B* **78**, 214519 (2008).

[192] A. Stockhausen, K. Il'in, M. Siegel, U. Södervall, P. Jedrasik, A. Semenov, and H.-W. Hübers, "Adjustment of self-heating in long superconducting thin film NbN microbridges," *Supercond. Sci. Technol.* **25**, 035012 (2012).

[193] W. C. Stewart, "Current-Voltage Characteristics of Josephson Junctions," *Appl. Phys. Lett.* **12**, 277 (1968).

[194] D. E. McCumber, "Effect of ac Impedance on dc Voltage-Current Characteristics of Superconductor Weak-Link Junctions," *J. Appl. Phys.* **39**, 3113 (1968).

[195] V. Ambegaokar and B. I. Halperin, "Voltage Due to Thermal Noise in the dc Josephson Effect," *Phys. Rev. Lett.* **22**, 1364 (1969).

[196] P. Thoma, J. Raasch, A. Scheuring, M. Hofherr, K. Il'in, S. Wunsch, A. Semenov, H.-W. Hubers, V. Judin, A.-S. Muller, N. Smale, J. Hanisch, B. Holzapfel, and M. Siegel, "Highly Responsive Y-Ba-Cu-O Thin Film THz Detectors With Picosecond Time Resolution," *IEEE Trans. Appl. Supercond.* **23**, 2400206 (2013).

[197] A. D. Semenov, P. Haas, H.-W. Hübers, K. Ilin, M. Siegel, A. Kirste, T. Schurig, and A. Engel, "Vortex-based single-photon response in nanostructured superconducting detectors," *Physica C* **468**, 627 (2008).

[198] L. N. Bulaevskii, M. J. Graf, and V. G. Kogan, "Vortex-assisted photon counts and their magnetic field dependence in single-photon superconducting detectors," *Phys. Rev. B* **85**, 014505 (2012).

[199] S. Soltan, J. Albrecht, and H.-U. Habermeier, "Ferromagnetic/superconducting bilayer structure: A model system for spin diffusion length estimation," *Phys. Rev. B* **70**, 144517 (2004).

[200] C. Granata, A. Vettoliere, R. Russo, M. Fretto, N. De Leo, and V. Lacquaniti, "Three-dimensional spin nanosensor based on reliable tunnel Josephson nano-junctions for nanomagnetism investigations," *Appl. Phys. Lett.* **103**, 102602 (2013).

[201] J. R. Clem and V. G. Kogan, "Kinetic impedance and depairing in thin and narrow superconducting films," *Phys. Rev. B* **86**, 174521 (2012).